Algorithmic Assessment of Cardiac Viability using Magnetic Resonance Imaging

Gang GAO

A thesis submitted in partial fulfillment of the requirement for the degree of Doctor of Philosophy

Department of Computing Science
&
Glasgow Cardiac Magnetic Resonance Unit
University of Glasgow

Acknowledgements

Although a few words do not do justice to their contribution, I would like to thank the following people for making this work possible. Dr. Paul Cockshott, for his tireless moral and academic support. Dr. John Foster, for endless references and pointers to research material. Dr. Bjoern Groenning, Dr. Thomas Martin, Dr. Patrick Mark, Dr. Kelvin Blyth and Dr Stuart Wakins, for bringing me into the magic world of Cardiology. Tracey Steedman, for her support in providing high quality magnetic resonance images. Professor Alex Elliott (technical director of GCMRU) and Professor Henry Dargie (clinical director of GCMRU) for their generous financial and academic support. Without their help, I can never go this far. Jinrong Huang, my beloved wife, I know she will always be there for me. Gao Si and Zhao Ying, my brother and sister in law, for their encouragements.

Special thanks to my parents, for their unconditional love, for everything.

Declaration

I hereby declare that the dissertation, submitted in partial fulfillments of the requirements for the degree of Doctorate of Philosophy and entitled "Algorithm Assessment of Cardiac Viability using Magnetic Resonance Imaging", represents my own work and has not been previously submitted to this or any other institution for any degree, diploma or other qualification.

Gang Gao

Abstract

MRI is a non-invasive imaging method which produces high resolution images of human tissues from inside the human body. Due to its outstanding ability, it is quickly becoming a major tool for medical and clinical studies, including high profile areas such as neurology, oncology, cardiology and etc.

MRI technology developed relatively slowly compared to other methods such as x-ray. A decade ago, it took more than 5 minutes to construct an MR image. However more recently, with several significant inventions such as echo planar imaging and steady state free procession techniques, the acquisition time of MRI has significantly reduced. At present, it is possible to capture dozens of MR images in a second. Those techniques are generally called ultra-fast MRI.

The fast MR acquisition techniques enable us to extend our studies to the moving tissues such as the myocardium. Using the ultra-fast MRI, multiple images can be acquired during a cardiac cycle allowing the construction of cardiac cinematographic MR images.

Cardiac motion can therefore be revealed. Abnormal cardiac motion is often related to cardiac diseases such as ischaemic myocardium and myocardial infarction. With advanced MRI techniques, cardiac diseases can be more specifically defined. For example, the late contrast enhanced MRI highlights acute myocardial infarction. The first-pass perfusion MRI suggests the existence of ischaemic myocardium. At the present time the majority of the analysis of MR images can be performed either qualitatively or quantitatively. The qualitative assessment is an eye-ball assessment of the images on a MRI workstation, which is subjective and inaccurate. The quantitative assessment of MR image relies on the computer technologies of both hardware and software. In recent years, the demands for the quantitative assessment of MR images have increased sharply. Many so-called computer aided diagnosis systems were developed to process data either more accurately or more efficiently. In this study, we developed an algorithmic method to analyse the late contrast enhanced MR images, revealing the so-called hibernating myocardium. The algorithm is based on an efficient and robust image registration algorithm. Using the image registration algorithm, we are able to integrate the static late contrast enhanced MR image with its corresponding cardiac cinematography MR images, and so constructing cardiac CINE late enhanced MR images. Our algorithm was tested on 20 subjects. In each of the subject, the mean left ventricle diastolic volume and systolic volume was measured by planimetry from both the original CINE images and the constructed late enhanced CINE images. The results are: left ventricle diastolic volume

(original / constructed) = 206 / 215 ml, p = 0.35. Left ventricle systolic volume (original / constructed) = 129 / 123 ml, p = 0.33. With our algorithm, the cardiac motion and the myocardial infarction can therefore be studied simultaneously to locate the hibernating myocardium which moves abnormally. The accurate location of the hibernating myocardium is important because it could turn into the irreversible myocardial infarction. On the other hand, with proper medical treatment or cardiac surgery, the hibernating myocardium could be revitalised. The experimental results show there are no significant differences between the artificial cine late contrast enhanced MR images and the original cinematography MR images in left ventricle diastolic volume, left ventricle systolic volume. The method therefore appears promising as an improved cardiac viability assessment tool.

In addition, we extended the method to a semi-automatic cardiac contour definition algorithm, which has produced a satisfactory result in contour definition for cardiac cinematography MR images from 34 subjects including 20 healthy volunteers and 14 patients. Although it is a semi-automatic method, the diagnosis time could be significantly reduced compared to the manual method. The algorithm was preliminarily tested on 10 first-pass perfusion MR sequences and 10 aortic MR sequences. The experimental results were satisfactory. Although, minor manual correction is required on

some occasions, we believe our method could be clinically useful for the study of cardiac cinematography MR images, first-pass perfusion MR images and aortic MR images.

Content

List of Figures

Chapter 1

Chapter 2

Chapter 3

Chapter 4

Chapter 5

Chapter 6

Chapter 7

Chapter 1
Introduction

1.1 Objectives of the work

The objective of this work is to develop a software package for the computer-aided analysis of cardiac viability using high resolution cardiac magnetic resonance (MR) images.

Different MRI modalities are involved in this work including cardiac cinematography MRI, late contrast enhanced MRI, the first-pass perfusion MRI and phase contrast MRI. The first three MRI techniques reveal cardiac structure and viability. The analysis of the phase contrast MRI suggests the velocity of blood flow, indexing the aortic stiffness.

MRI is one of the latest medical imaging technologies. It is similar to the computer tomography (CT) scan [Dhawan, 2003] in that it produces cross-sectional image of the body, although it is based on totally different principles. Unlike CT scans, MRI does not use X-rays[1], which could be harmful for the human body. It uses a strong magnetic field and radio-frequency pulses to produce clear and detailed images of the inside of the body.

[1] **CT scans are special x-rays tests discovered by British engineer G. Hounsfield and A. Cormack. It has become a mainstay for diagnosing medical diseases.**

As a non-invasive method, MRI technology has been significantly improved in the past twenty years. Clinical MRI studies have been extended from the relatively static tissues such as brain [Valk 1987][Jezzard et al., 2001], bone [Valk 1987] etc to the moving tissue such as myocardium. At present, with the so-called ultrafast imaging techniques [Cohen & Weisskoff, 1991], most of the commercial MRI scanners are able to produce multiple high resolution images during a cardiac cycle, producing cardiac cinematographic (CINE) MRI images.

Cardiac CINE MRI is one of the most widely used MRI technique. It provides structural information about the myocardium, such as volume, cardiac wall thickness as well as cardiac wall motion information [Mitchell 1999]. The reduced cardiac wall motion indicates the existence of cardiac disease, such as myocardial infarction. With the help of an MRI contrast enhancement agent, Gd-DPTA, myocardial infarction can be observed directly using MRI due to contrast differences. A cardiac viability score can be derived by the study of cardiac wall motion in combination with the presence of myocardial infarction.

However at present, the viability assessment is at a preliminary stage of development. The manual analysis is still widely used and therefore subjective errors are inevitable. A further problem is that the cardiac CINE MRI images and its corresponding late enhancement image are acquired separately [Chen et al., 2003]. The mis-registration between the two types of images caused by unavoidable patient motion may produce diagnostic error. Our research work is to develop an automatic solution which allows

correction of the motion between CINE images and contrast enhanced images [Gao et al., 2004][Gao & Cockshott et al., 2004]. The hypothesis is that the cardiac motion data could be extracted from CINE MRI images using a free-form non-rigid image registration algorithm. The motion data will be used to digitally align the late contrast enhanced image to its corresponding CINE sequence, producing an artificial CINE sequence with late contrast enhancement. The analysis of such a sequence reveals 1) the cardiac motion and 2) the location of myocardial infarction simultaneously. The reduced human intervention and the alignment between the CINE and the late contrast enhanced images are expected to provide more persuasive results for the cardiac viability study.

Misalignment has become a general problem in medical image analysis because of inevitable subject motion such as respiratory motion. However in many cases, the alignment of the entire image is unnecessary. The processing can be simplified to the alignment of the defined contours. As a sub-study of this work, we extended our automatic image alignment algorithm to a contour deformation model. The contour deformation model could work as a semi-automatic contour definition algorithm, which could find a large number of applications in cardiac MRI study such as first-pass perfusion, pulse wave velocity and the distensibility of aorta.

1.2 This thesis

The thesis has been divided into eight chapters. After the initial introduction, Chapter Two, "**Introduction of MRI**", discusses the physical principle of MRI technology. "What are MRI signals", "How to locate MRI signals spatially" and "How to construct MRI images from MRI signals" are the three questions to be examined. Basic MRI pulse sequences such as gradient echo and spin echo will be introduced in this chapter.

Chapter Three, "**Introduction of Cardiac MRI**", continues the discussion of MRI technology but focuses on Cardiac MRI technology. The chapter begins with a preliminary introduction of the anatomic structure of myocardium and then moves to the theoretical and technical details of cardiac MRI technologies, including cardiac cine MRI, late contrast enhanced MRI, first past perfusion MRI, etc. Some preliminary image analysis methods corresponding to different MRI techniques will also be introduced.

Image registration is the main image processing technique used in this work. A full understanding of the image registration process is essential. Chapter Four, "**Image registration**" discusses the background of image registration.

In this study, we set out to develop an image registration based algorithm to align CINE MR images and late contrast enhanced MR image.

All the data produced in this study were measured and evaluated by software package Cardiowarp which was developed in Glasgow Cardiac Magnetic Resonance Unit (GCMRU). In Chapter Five, "**The validation of the measurement**", we evaluated the

accuracy of Cardiowarp by comparing its measurement results with a conical phantom and a well known and clinically validated software package, Argus (Siemens Medical Systems).

In Chapter Six, "**A motion study of late contrast enhanced MRI**", we will present our method of constructing CINE late contrast enhanced MR images. The late contrast enhanced MR image reveals precise details about myocardial infarction, including its size and location. However, the acquisition of late contrast enhanced MR image is time consuming, and can only produce one image for each scan. From the CINE late contrast enhanced MR images, clinicians hope to improve the localization of ischaemic myocardium which may not be observable directly from the original late contrast enhanced MR image.

In Chapter Seven, "**The extensive studies**", we extend this work to a semi-automatic contour definition algorithm. Definition of cardiac contours is involved in most of cardiac MRI studies. At present, cardiac contours are defined manually to ensure accurate results. But manual contour definition is tedious, time consuming and subjective. Many efforts in the past years have been made to develop an efficient and fast automatic contouring algorithm. However, at present, none is used in clinical studies. Although our method is a semi-automatic algorithm, we believe it still can be a great improvement. The algorithm has been tested on cardiac CINE MR images, first-pass perfusion images and two types aortic MRI images (aortic CINE MRI and PCMRI). Experimental results and discussion will be presented in this chapter.

Chapter Eight is the conclusion of this work and future development work and potential ideas will be discussed.

Chapter 2

Introduction to MRI

Magnetic resonance imaging (MRI) is a noninvasive medical imaging technique based on the physical phenomenon of nuclear magnetic resonance (NMR) (Mitchell, 1999). It is based on the detection of water and fat protons (H_1). Because H_1 is in high concentration in human tissues, even weak NMR signals can be picked up to create images. Less than two decades old, MRI offers diagnostic power far beyond that of radiographic density based methods.

Any attempt to memorise the protocols of MRI is difficult, because they are complex, numerous and change rapidly. However, a solid understanding of the underlying principles is essential. In section (2.1), the history of MRI will be briefly described. In section 2.2, the basic physical principles of MRI will be introduced. We will examine:

1. What MRI signals are.
2. How to locate MRI signals.
3. How to construct MRI images from MRI signals.

Some practical MRI acquisition methods will be introduced in sections 2.3 and 2.4.

2.1 History of Magnetic Resonance Imaging

The phenomenon of nuclear magnetic resonance (NMR) was discovered independently by two American scientists, F. Bloch and E. Purcell in 1946 (Bloch et al., 1946; Purcell et al., 1946). This discovery allowed NMR to be used as an analytical tool for studying the structure of solids and liquids at a molecular level (Cho et al., 1993; Beutel et al., 2000). This was the main use of NMR between 1950 and 1970 until the interest of medical applications arose. F. Bloch and E. Purcell were awarded the Nobel Prize in 1952.

In the late 60s and early 70s, Raymond Damadian demonstrated that the relaxation time of excited protons in tumour samples, measured in vitro, was significantly higher than normal tissue (Damadian, 1971). Paul Lauterbur, University of Illinois at Urbana-Champaign and Peter Mansfield, University of Nottingham in England took advantage of this discovery and acquired the first MR image of a test tube in 1973 by using magnetic gradients for spatial encoding and reconstructing the image (Lauterbur, 1973; Mansfield et al., 1973). Paul Lauterbur and Peter Mansfield shared the 2003 Nobel Prize in Physiology or Medicine. They are named as the fathers of MRI. After these crucial discoveries, spin system understanding, gradient technology, signal detection and data handling developed considerably. This led to many new imaging sequences and methods being developed during the 1980s (Bernstein et al., 2004). Artifacts from earlier years were now better understood and compensation techniques could be developed or the artifacts could be exploited to produce new imaging methods.

Cardiac imaging improved considerably in the mid to late 1980s when compensations for artifacts such as cardiac motion and flow were developed. As a result of these compensatory techniques the first cine images of the cardiac cycle were taken in 1987 while the art of myocardial labeling for the study of cardiac motion was developed in 1989 by L. Axel and L. Dougherty (Axel & Dougherty, 1989).

Figure 2.1 illustrates the milestones of the developments of MRI techniques.

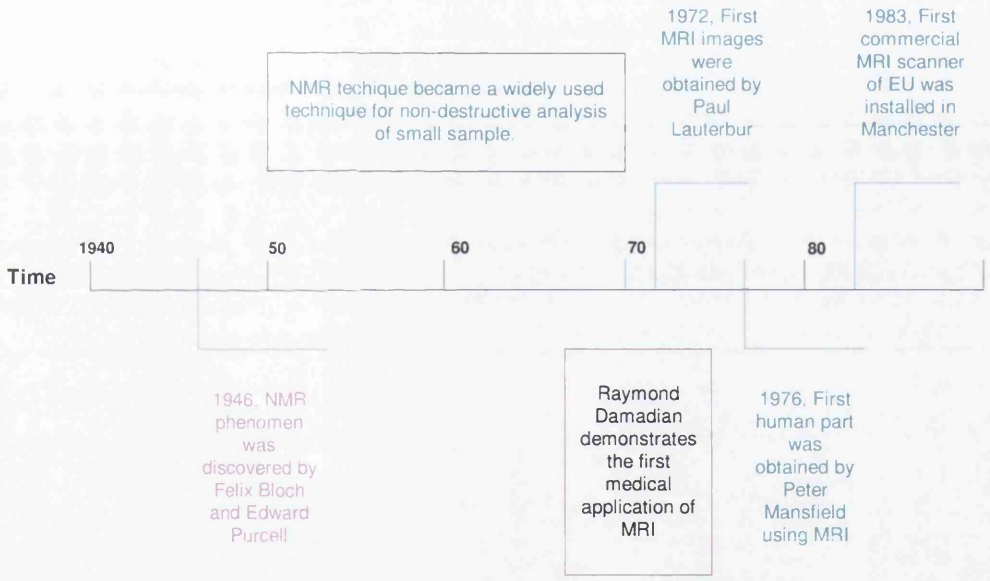

Figure 2.1 The history of MRI

2.2 MRI Theory

Protons, subatomic particles, exist in every object. They are constantly spinning. Each of the spinning protons has a magnetic axis. Naturally, the orientation of these axes is random. In the presence of an external magnetic field, the axis of these spinning protons will be rearranged either parallel or antiparallel to the direction of the magnetic field. The number of protons aligned with the external magnetic field is slightly higher than the protons aligned against the external magnetic field. For simplicity, we consider the overall alignment of protons instead of the behaviour of each proton.

The inequality of alignment of protons in the presence of a magnetic field makes a net magnetisation. The net magnetisation aligns with the direction of the external magnetic field. It is referred to as the ***net longitudinal magnetisation*** or the ***longitudinal magnetisation***. The inequality of protons inside a magnetic field is referred to as ***equilibrium***.

The longitudinal magnetisation is the source of MR signals. However, it is rather difficult to measure the longitudinal magnetisation because it is swamped by the external magnetic field. A direct solution is to work out a method which could change the direction of the longitudinal magnetisation, which allows it to be differentiated from the external magnetic field. Scientists found this can be done by using a radio pulse. A radio pulse with a certain frequency can break the equilibrium, rotating the longitudinal magnetisation toward the transverse plane, thereby forming ***transverse magnetisation***.

The transverse magnetisation is orthogonal to the external magnetic field. The change of the transverse magnetisation can therefore be detected by an inductive coil which produces a changing electrical signal as electric current, produced from the well-known Faraday electricity and magnetisation theory.

Although the physical principles of MRI are rather straightforward, there are many practical difficulties which scientists have been trying to solve in recent decades. Many difficulties involve:

1. How to read MR signals.
2. How to read MR signals from a specified imaging plane.
3. How to capture MR signals efficiently and therefore reduce the scan time.

These questions will be answered in the following sections.

2.2.1 MR signals

There is little possibility of detecting net longitudinal magnetisation because it is dwarfed by the external magnetisation field. It has been discovered that the longitudinal magnetisation can be rotated to the transverse plane, building transverse magnetisation by exposing protons to a radio frequency pulse which has the same frequency of the proton

precession. The Larmor equation explains the relationship between the frequency of precession and the external magnetic field strength (SimplyPhysics, 2002).

$$\varpi = B_0 \cdot \gamma \qquad 2.1$$

where ϖ is the frequency of precession, γ is the gyromagnetic ratio and B_0 is the strength of the external magnetic field. The standard unit of the magnetic field strength is ***tesla***, or **T**. The gyromagnetic ratio is a constant. For hydrogen, γ = 42.58MHz/T. The magnetisation strength change along the transverse plane can easily be picked up by a coil, based on the electromagnetic theory of Michael Faraday.

The disturbance of net longitudinal magnetisation is referred to as ***excitation***. The radio pulse applied to disturb the equilibrium is called an ***excitation pulse***. At a proper strength and duration, a radio pulse may rotate the net magnetisation from the longitudinal plane to the transverse plane completely. This pulse is called a 90° pulse. Likewise, an excitation pulse with a proper strength is referred to as a 180° pulse if it rotates the net magnetisation by an angle of 180°. The degree of rotation caused by the radio pulse is called the ***flip angle***.

Following the excitation pulse, the net magnetisation goes back along the longitudinal axis from minimum to maximum. Meanwhile, the transverse magnetisation fades away quickly. The recovery of the longitudinal magnetisation is referred to as ***T1 relaxation***. The decay of the transverse magnetisation is referred to ***T2 relaxation***. Generally, the excitation and relaxation have to repeat in order to generate enough MR signals, constructing high resolution and high quality MR images. The time between repetitions

of the excitation pulse is defined as the ***repetition time (TR)***. The time between the initial creation of transverse magnetisation and its measurement is referred to as the ***echo time (TE)***.

T1 weighted MRI images

With the same magnetisation field strength, the rate at which the longitudinal magnetisation recovers from saturation, the ***T1 relaxation rate***, is determined by the tissue itself. The ***T1 relaxation time*** is defined as the time required for the longitudinal magnetisation to recover to 63% of its original equilibrium level after complete saturation by a 90° pulse. After twice the duration of the T1 relaxation time, about 91% longitudinal magnetisation has recovered. After three T1 relaxation times, the recovery reaches about 97%. During relaxation, the longitudinal magnetisation forms a logarithmic curve against time figure 2.2.

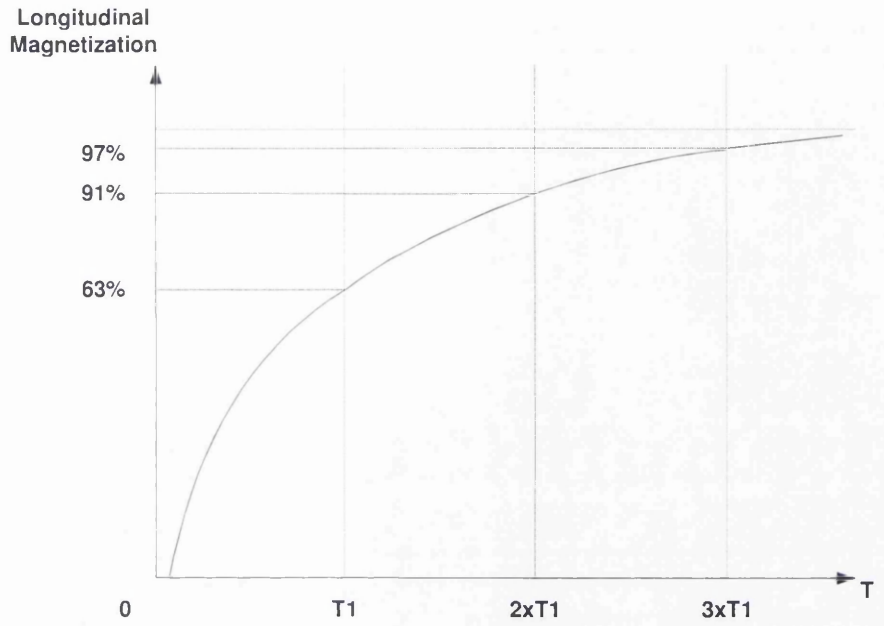

Figure 2.2. The longitudinal magnetisation recovers following a logarithmic curve.

At a given magnetic field strength T1 relaxation time is a constant property of tissue. Table 2.1[1] lists the T1 relaxation time of human tissues. At a magnetic field strength, for example 1.5 Tesla, the T1 relaxation time of fat is about 250 milliseconds which is significantly shorter than the T1 relaxation time of muscle (about 863 milliseconds). Therefore, at the time point t (t < relaxation time **T**), the strength of the longitudinal magnetisation of the fat, M_{fat}, is stronger than the longitudinal magnetisation of muscle, M_{muscle}. If the MR signals are picked up at t, the signal intensity generated from the fat would be stronger compared to the MR signals generated from the muscle resulting in a contrast between fat and muscle in the constructed MR image (figure 2.3[2]).

[1] **Data source: [Mitchell, 1999]**
[2] **Image source: http://www.gemedicalsystemseurope.com**

	T1 at 1.5T (msec)
Fat	250
Liver	490
White matter	783
Muscle	863
Spleen	778
Gray matter	917
CSF	3000

Table 2.1 Representative T1 relaxation time at 1.5T

The images depict the differences of T1 relaxation time and are referred to as ***T1 weighted images***. The contrast of T1 weighted images depends on the repetition time of the excitation pulse (**TR**) and the so-called **flip angle**. The flip angle is the angle to which the net magnetisation is rotated or tipped relative to the main magnetic field direction via the application of an excitation pulse (http://www.mr-tip.com). With a flip angle of 90°, the longitudinal magnetisation saturates completely to the transverse plane. Using a short TR, the excitation pulse repeats before the full recovery of the longitudinal magnetisation, and the generated reverse magnetisation could be weaker than it was. This may harm the T1 contrast of the resulting images but reduce the data acquisition time.

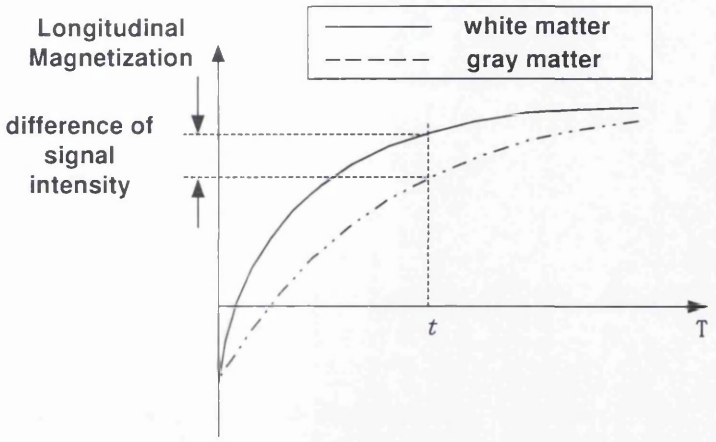

(a)

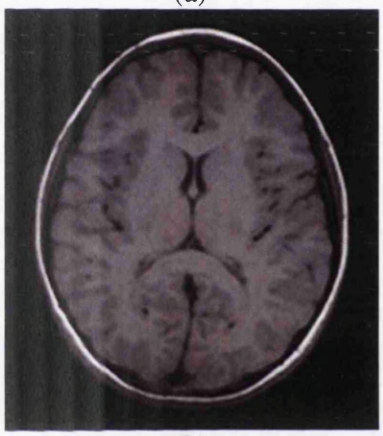

(b)

Figure 2.3 T1 difference between white matter and gray matter. White matter has a shorter T1 compared to gray matter. At an appropriate acquisition time, the T1 signal from white matter is stronger than from gray matter.

The flip angle is determined by the strength and the duration of the excitation pulse. Different flip angles could be produced using an excitation pulse with a different combination of strength and duration. A flip angle of less than 90° only partially converts the longitudinal magnetisation to the transverse plane. Therefore, the longitudinal magnetisation recovers more closely to its initial strength when the next radio frequency pulse comes. However, full strength of transverse magnetisation cannot be achieved using such a small flip angle. The strength of MR signal is not as strong as those

generated using a 90° flip angle. T1 contrast could be sacrificed. The selection of TR and flip angle needs to be considered carefully in order to produce good quality MR images. For any TR, there is an optimal flip angle that maximises the signal to noise ratio. This optimal angle is referred to as the Ernst angle[1] (Mitchell, 1999). The Ernst angle can be calculated mathematically by using equation 2.1.

$$\cos\alpha = e^{(-TR/T1)} \qquad (2.1)$$

where α is the Ernst angle and T1 is the T1 relaxation time of the imaging object.

(Mitchell, 1999) reported that an optimisation can be achieved by using a combination of 17 / 20°, 50 / 45° or 250 / 90°.

T2 and T2* weighted MRI images

[1] **The ernst angle is named after Richard R. Ernst, Nobel laureate in chemistry, 1991.**

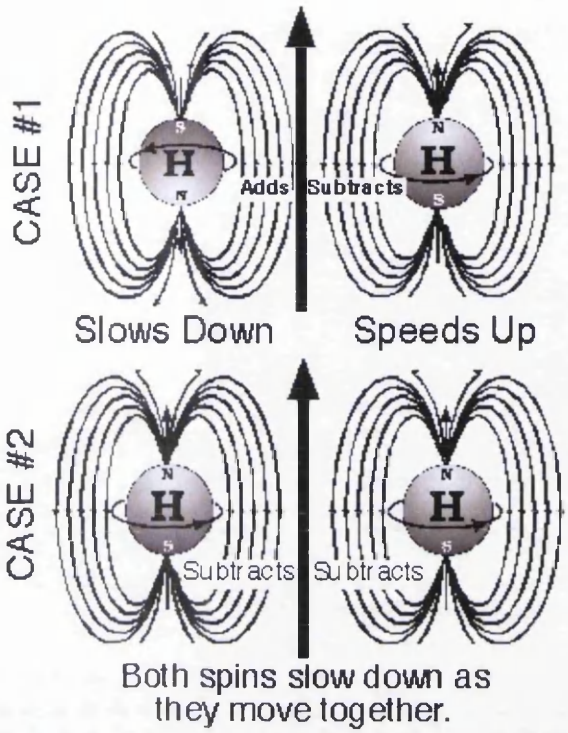

Figure 2.4 The interaction between two spinning protons could produce different results. If the magnetic axes of two protons have the same orientation, the spins slow down as they move together. Otherwise, proton whose magnetic axis is opposing the main magnetic field will spin slower as the other one will spin faster.
Image source: http://www.simplyphysics.com

When the longitudinal magnetisation is first tilted down to the transverse plane, proton precesses are all in phase. The precession frequency of an isolated proton is only related to the magnetic field that it experiences. As protons move together, the local magnetic fields begin to interact. As a result, some protons may spin faster than others (figure 2.4). Quickly, the proton precession will become out of phase and point to different directions in the transverse plane, so their magnetisation in the transverse plane cancels each other out. The transverse magnetisation is completely eliminated when protons are pointing in opposite directions. The decay of transverse magnetisation due to the interaction between protons is called ***T2 relaxation*** or ***T2***. The T2 relaxation time is defined as the time after

the excitation when the signal intensity has been reduced to 36.8% of its original strength. As with T1, each tissue has an identical T2 relaxation time. Table 2.2 lists T2 relaxation time for several typical human tissues. Figure 2.5a shows a representative example of a T2 curve. Figure 2.5b shows a T2 weighted MRI image.

	T2 (msec)
Fat	85
Liver	43
White matter	90
Muscle	47
Spleen	62
Grey matter	100
CSF	1400

Table 2.2 Representative T2 relaxation time.

T2 relaxation is independent of the strength of the external magnetisation field as the result of proton interactions. It explains the decay speed of MR signals under the assumption that the external magnetic field is absolutely homogeneous. However, in reality MR signals always decays faster than T2 would predict because of the imperfection of the magnetic field in homogeneity. There are many factors creating the inhomogeneity of the magnetic field: the external magnetic field may have flaws in its manufacture. The tissues have different magnetic susceptibility which distorts the field at tissue borders; the patients may have a metal implant. To explain the decays of MR signals in an imperfect magnetic field, a new parameter ***T2**** is defined. Equation 2.2 shows the mathematic definition of T2*.

$$\frac{1}{T2^*} = \frac{1}{T2} + \frac{1}{T2_{in\,hom}} \qquad 2.2$$

where $T2_{inhom}$ is the dephasing time caused by the inhomogeneity of the magnetic field.

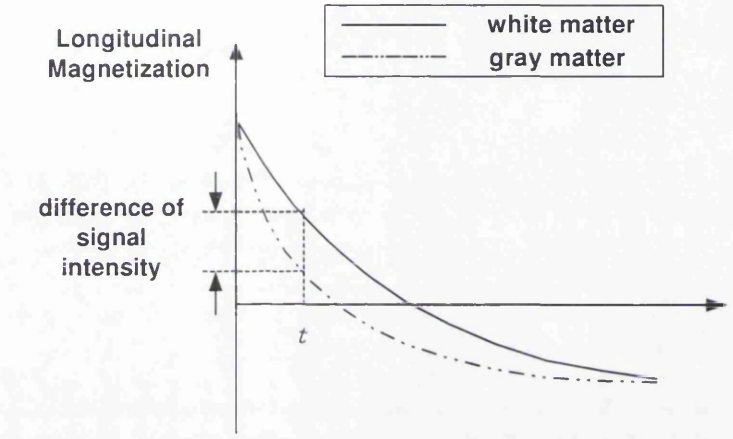

(a)

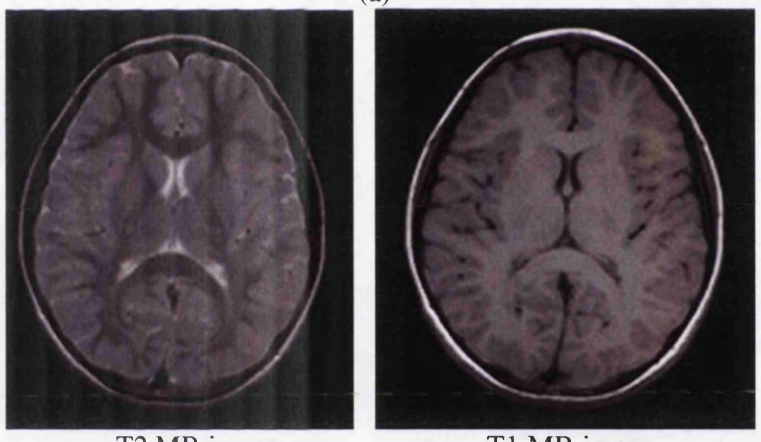

T2 MR image T1 MR image

(b)

Figure 2.5 (a). T2 relaxation curves of white matter and gray matter; (b) a T2 weighted MR image. For comparison, its corresponding T1 weighted image is also shown.

Similar to T2 relaxation, T2* is a unique property of a tissue. It could be particularly useful, especially for the design of the ultra-fast MR technique. But the fast decay of MR signals may corrupt the image quality severely. Many approaches, including rephasing

magnetic field gradients and 180° refocusing pulse, are applied to restore MR signals before data acquisition (Mitchell, 1999; Bernstein et al., 2004). Those techniques will be introduced in section 2.2.3

2.2.2 MR Image Generation

The generation of T1 or T2 / T2* MR images is decided by the combined setting of TR and TE. To produce a T1 weighted MR image, a short TR is chosen to prevent the full recovery of the longitudinal magnetisation and maximise the signal differences between different tissues. Meanwhile, the short TE is required to acquire the MR signals T2 relaxation starts, thereby minimising T2 contrast. For the T2 weighted MR images, a long TR is selected to allow the total recovery of the longitudinal magnetisation, minimising the T1 effects. A long TE is also needed in order to allow the decay of the transverse magnetisation to start.

Image Types	**TR**	**TE**
T1	Short TR	Short TE
T2 / T2*	Long TR	Long TE
Proton density	Long TR	Short TE

Table 2.3 The combined setting of TR and TE decides the type of MR image

Table 2.3 summarises the combined setting of TR and TE to produce different types of MR images. There is a third type of image called proton density weighted image. The proton density weighted image is generated by choosing a long TR greater than T1

(typically > 2000ms) and a short TE less than T2 (typically < 30ms). The long TR and short TE minimise the effects of T1 and T2. Therefore, the contrast of constructed image depends primarily on the density of protons in the imaging volume. Figure 2.6 shows an example of the proton density weighted MR image.

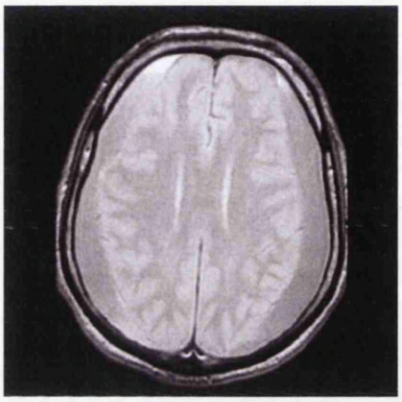

Figure 2.6 a proton density weighted MR image
image source: http://www.neuroradiologyportal.com/articles/semneuro_files

Anatomic segmentation of brain images is one of the major applications of the proton density weighted MR images (Bezdek et al., 1993; Clarke et al., 1995).

2.2.3 Magnetic Field Gradients

In MRI, a magnetic field gradient refers to a supplemental magnetic field which is superimposed on the main magnetic field. The strength of the magnetic field gradient varies linearly along a predetermined axis, ensuring that the total magnetic field has the greatest strength at one end and the least strength at the other. The magnetic field

gradients play a central role in MR imaging. Their primary function is to encode spatial information into MR signals so that it can be recovered later during the reconstruction process to form an image (Bernstein et al., 2004).

Slice selection gradient

When a slice selection gradient is present, protons in the tissues precess at varying frequencies along the direction of the gradient. If a radio frequency pulse is transmitted into a tissue during the application of a slice selection gradient, the radio frequency pulse excites only the tissues that precess at the appropriate frequency, corresponding to a particular position along the axis of the magnetic field gradient. Therefore, only a limited slice of tissue is excited (figure 2.7a). Two or more slice selection gradients applied simultaneously can locate an oblique 2D plane in 3D space (figure 2.7b).

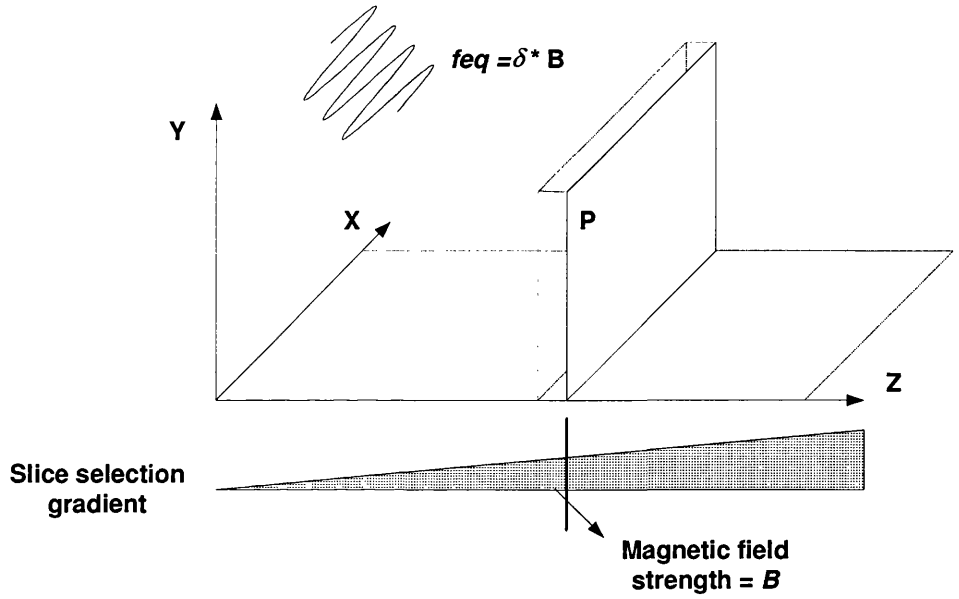

(a)

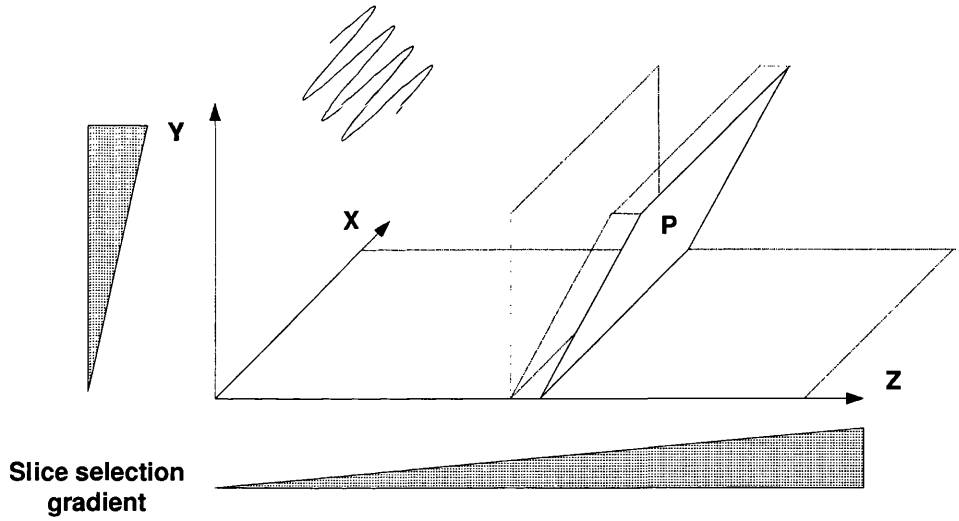

(b)

Figure 2.7 a). One slice selection gradient can locate a vertical or a horizontal plane; b). two slice selection gradients work together to locate an oblique plane.

The Frequency Encoding Gradient and the Phase Encoding Gradient

The frequency encoding gradient is often referred to as the readout gradient because it is always applied during a reading of the MR signals. In the absence of magnetic field gradients, protons in the tissue precess at an identical frequency. In the presence of the slice selection gradient, a particular region of tissue is excited by a transmitted radio frequency pulse. The frequency encoding gradient is applied perpendicular to the slice direction. Under the influence of this new magnetic field gradient, along its direction, the protons begin to precess at different frequencies depending on their position within the gradient, in accordance with equation 2.1 (figure 2.8).

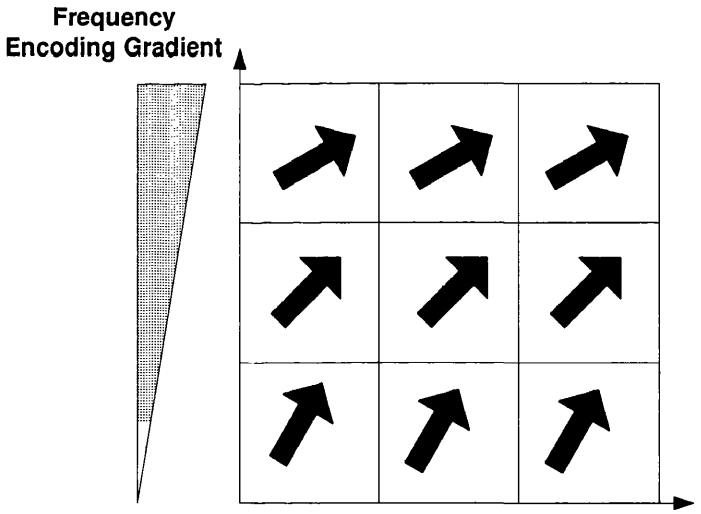

Figure 2.8 The frequency encoding gradient determines the MR signals from a 2D plane located by the slice selection gradient. The grid suggests the positions of protons. Each arrow represents a proton. The orientation of an arrow suggests the precessing frequency of a proton.

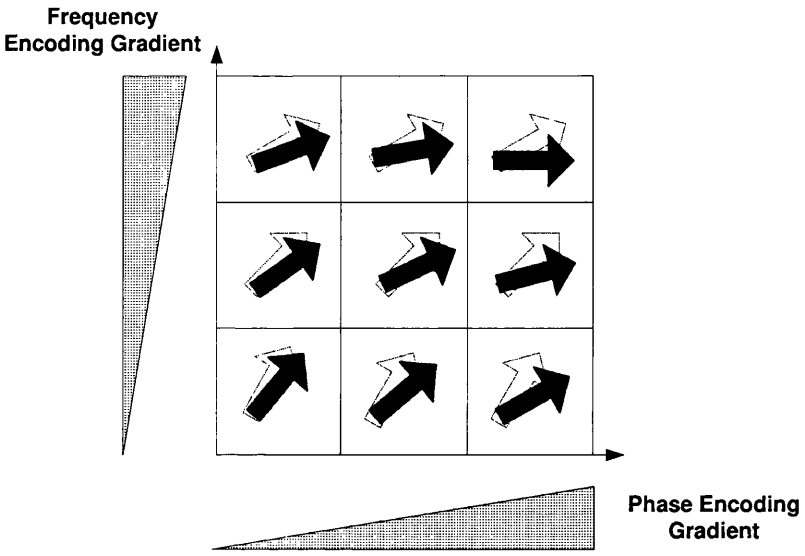

(a)

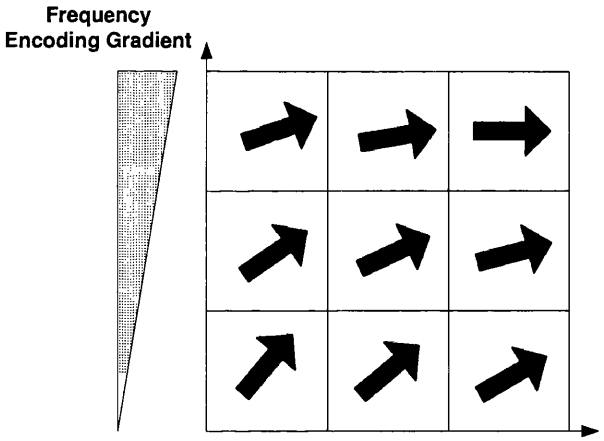

(b)

Figure 2.9 (a) The phase encoding gradient is applied when the frequency encoding gradient is activated. The dashed arrow indicates the frequency of protons before the application of the phase encoding gradient; (b) following the phase encoding gradient, the precessing frequency of protons returns to coherence, but with difference phase.

The frequency encoding gradient localises the first in-plane axis of the image by making the tissue precess at varying but predictable frequencies along its direction. The second

in-plane axis is localised by the so-called phase encoding gradient. The phase encoding gradient is perpendicular to both the slice selection gradient and the frequency encoding gradient. It is applied right before the application of the frequency encoding gradient, but is only present for a short period. The phase encoding gradient changes the precessional frequency of protons temporally. After the application of the phase encoding gradient, the frequencies of proton precession return to be identical but are ahead or behind in phase relative to their previous state. The phase encoding gradient along with the frequency encoding gradient give each proton in the excited region (imaging plane) a unique combination of precession frequency and phase (figure 2.9).

During the application of the frequency encoding gradient, MR signals, $S_{MR}(t)$ are picked up from the excited region. The signals can be described mathematically by equation 2.3

$$S_{MR}(t) = \sum_i S_i(t) \qquad 2.3$$

where $S_{i:i=1:N}(t)$ represents the signals released from different physical locations. Each $S_{j:j\in i}(t)$ has a unique combination of frequency and phase generated by the frequency encoding gradient and the phase encoding gradient. However, the unique phase works only in a limited range from 0 to 2π . Therefore, many positions will have integer multiples of phase values that other positions have. This would then make it impossible to identify a position uniquely, hence the phase encoding gradients must be repeated at different magnitudes so that the phase in the same physical position changes in a systematic way, which can be digitalised and derived by Fourier transform.

Data sampling and k-space

In the magnetic field gradient direction, transverse magnetisation decays quickly once created. Identical magnetic field gradients with opposite polarity or a 180° pulse is applied to refocus the transverse magnetisation (more details can be found in section 2.2.4). MR signals are picked up shortly before the full recovery of transverse magnetisation. So an MR signal always has a weak intensity at the beginning. It reaches a peak at the middle of the signal and then becomes weaker again due to the decay of the transverse magnetisation.

MR signals are in temporal space and continuous over time. It must be converted to a digital form in order to transform the signals to the more comprehensive physical space using computer. The digitalisation process is referred to as ***data sampling***. The selection of the data sampling rate is vital since it controls the image resolution and the signal to noise ratio (SNR) of the constructed image. Using a high data sampling rate, more data points are acquired within a particular time resolution resulting in high resolution MR images. However, a high data sampling rate is more sensitive to noise compared to a low data sampling rate, and therefore a constructed image will be more "noisy". Figure 2.10 graphically explains the difference between using a high data sampling rate and a low data sampling rate.

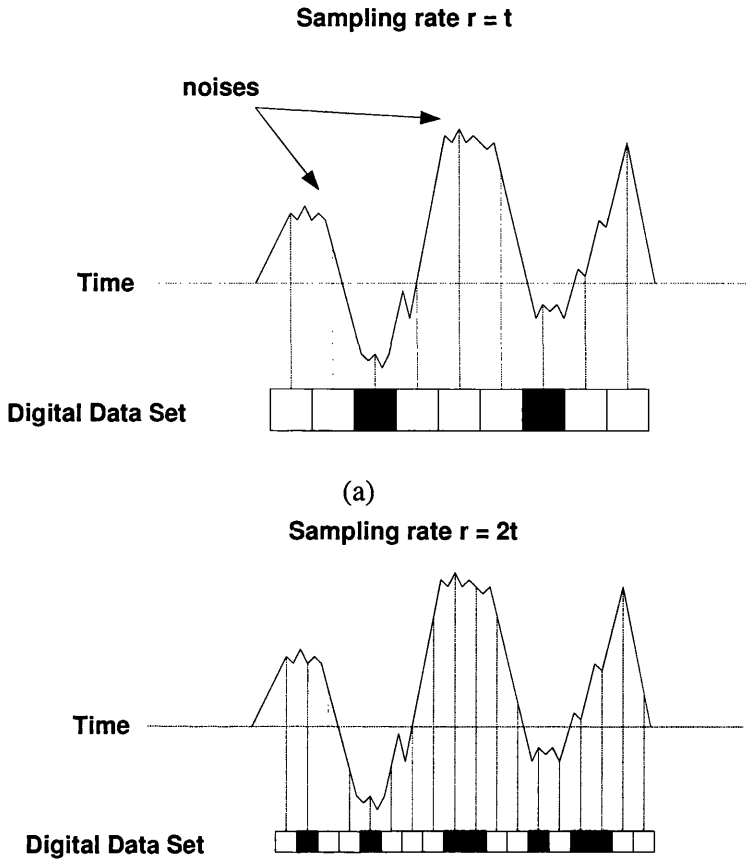

Figure 2.10 Using a low data sampling rate, the produced image resolution is low but less sensitive to the noise. (a) Data sampling with a rate of t; (b) Data sampling with a rate of 2t. The dark area in the digital data set indicates the portion may be infected by the noise.

Each time, the phase encoding gradient repeats, an MR signal is read. MR signals are digitalised and put together line by line, building a 2D map called ***k-space*** (figure 2.11).

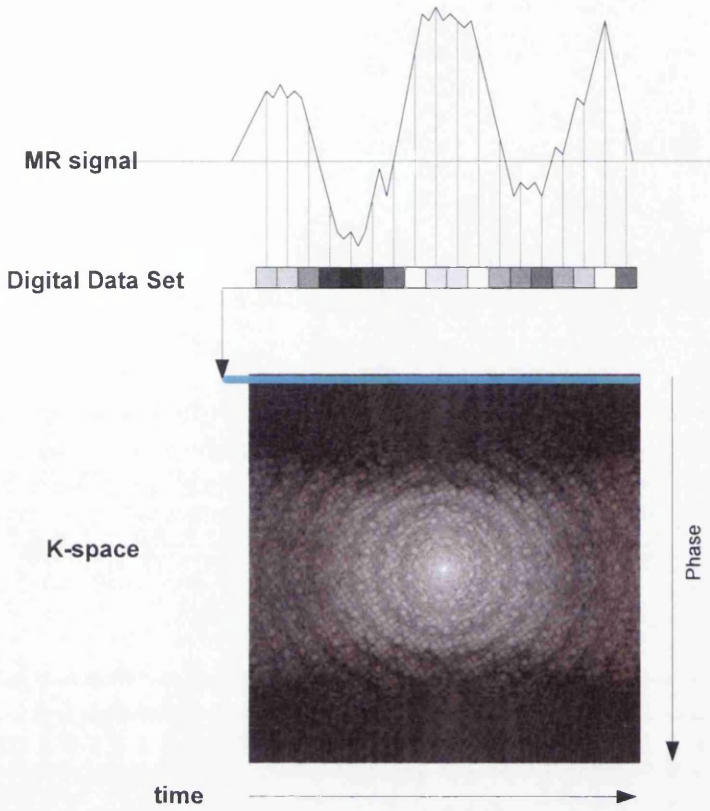

Figure 2.11 The construction of k-space

MR signals stored in k-space are generated in the physical space and labelled with a unique combination of phase and frequency. With a proper mathematic transform, the Fourier transform, k-space could be converted back to physical space, building the MR images.

The spatial resolution of the constructed image can be depicted from k-space. The largest image feature which is said to have the lowest spatial frequency is encoded in the center of k-space (Mitchell, 1999). On the other hand, the smaller image features, which have a high spatial frequency, are encoded in the periphery of k-space. Figure 2.12 shows

increasing blurring as data from the periphery of k-space are eliminated, suggesting that the centre of k-space contributes to most of the contrast of the constructed MR image. In figure 2.13, the centre of k-space is cut. The constructed image consists principally of fine detail and minimal image contrast.

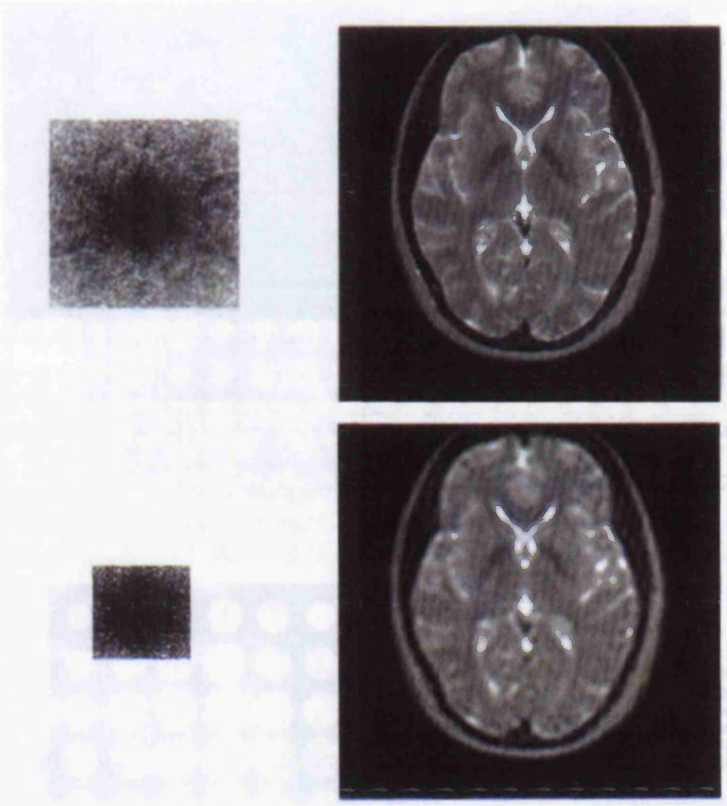

Figure 2.12 The center of k-space contributes to the image contrast

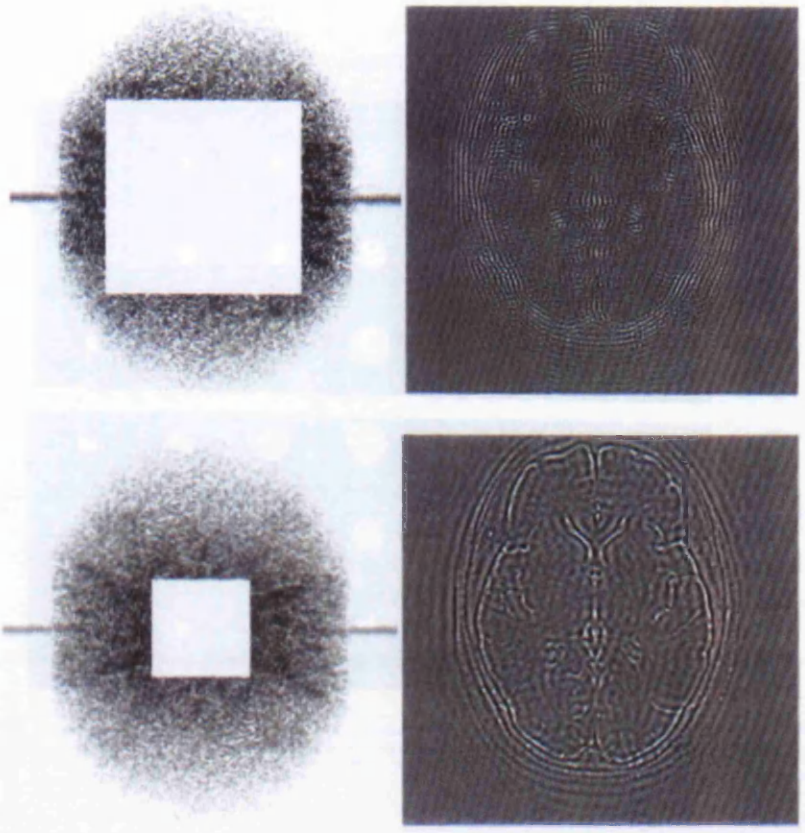

Figure 2.13 Images built from the signals locate in the periphery of k-space consist fine detail but low image contrast.

2.2.4 Pulse Sequences

Thus far, we have discussed the physical principles of MR technology. This includes the generation of MR signals and the application of magnetic field gradients. We have also introduced two types of MR images, the T1 weighted images and the T2 or T2* weighted images. A radio frequency pulse selectively excites protons in a magnetic gradient field, pushing the net magnetisation toward the transverse plane, building the transverse

magnetisation. The transverse magnetisation is the source of MR signals. Follow the radio frequency pulse, protons return to equilibrium. The recovery of the longitudinal magnetisation is referred to as the T1 relaxation. The decay of the transverse magnetisation is referred to as the T2 relaxation. The T1 relaxation time and the T2 relaxation time are constant properties of tissues at a given magnetic field strength. Both T1 weighted images and T2 weighted images can be the building of contrast in the MR images by exploring the difference of T1/T2 relaxation time between tissues. But the construction of MR images suffers a major difficulty because of the fast decay of MR signals could seriously affect the constructed image quality (see section 2.1.1). Scientists have discovered that an additional magnetic gradient with opposite polarity or a 180° pulse in the middle of the TE could restore MR signals. In recent decades, much work has been carried out to optimise and combine the use of magnetic field gradients and excitation pulses, which meet different requirements. The combination and use of radio frequency pulses and magnetic gradients is referred to as a ***pulse sequence***.

The pulse sequence is often graphically illustrated in scientific papers, books, etc. Figure 2.14 gives a basic example of a pulse sequence.

In figure 2.14, each line belongs to a different hardware component. One line is needed for the radio frequency transmitter, and one for the magnetic field gradients. For simplicity, we only show one gradient in this example.

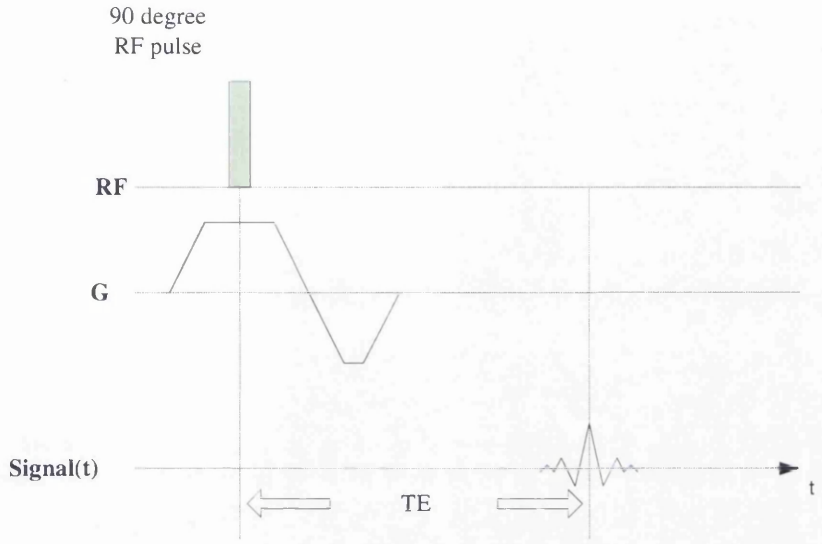

Figure 2.14 A basic pulse sequence used to refocus the dephased transverse magnetisation

The magnetic field gradient we used has two lobes with opposite directions. The first lobe is referred to as the dephasing lobe and the second lobe is the rephasing lobe (Mitchell, 1999). During the application of an imaging gradient's dephasing lobe, protons precess faster at one end than the other. Their precession phases will also be different. After the dephasing lobe, the frequencies of the proton precessions return to be identical but their phases will remain different. From section 2.1.1, we knew the strength of the net transverse magnetisation can be seriously reduced when the neighbouring protons in the imaging plane precess in different phases. The objective of the rephasing lobe is to regain phase coherence and therefore generate enough transverse magnetic field strength (MR signal strength) to produce images. Follow the dephasing lobe, the rephasing lobe is turned on. Protons that precess faster during the dephasing lobe are now precessing slower than protons at the other end. The phase difference created by the dephasing lobe

is closing. If the dephasing lobe and the rephasing lobe have the same amplitude and duration, the phase difference can be eliminated completely.

Three different kinds of magnetic field gradients are used in a pulse sequence to determine the spatial location of the imaging plane. The three magnetic gradients are the slice selection gradient (Gs), the frequency encoding gradient (Gf) and the phase encoding gradient (Gp). Figure 2.15 shows a practical pulse sequence.

The pulse sequence shown in figure 2.15 is called the gradient echo because the MR signals (echo) are created by the application of a pair of opposite magnetic gradients (Frahm et al., 1986). The slice selection gradients are on while a 90° excitation pulse is applied. The added magnetic field gradients increase the inhomogeneity of the magnetic field and increase the decay of the transverse magnetisation. The rephasing lobe of the selection gradient was applied to bring the strength of the transverse magnetisation back to its maximum. The phase encoding gradients were turned on for a short time to mark different phases along their directions before the application of the frequency encoding gradient. The frequency encoding gradients identify the MR signals in the last dimension. The frequency encoding gradient also dephases proton precession, reducing the strength of the transverse magnetisation. Again, we need the help of the rephasing lobe to bring back the strength of the MR signal.

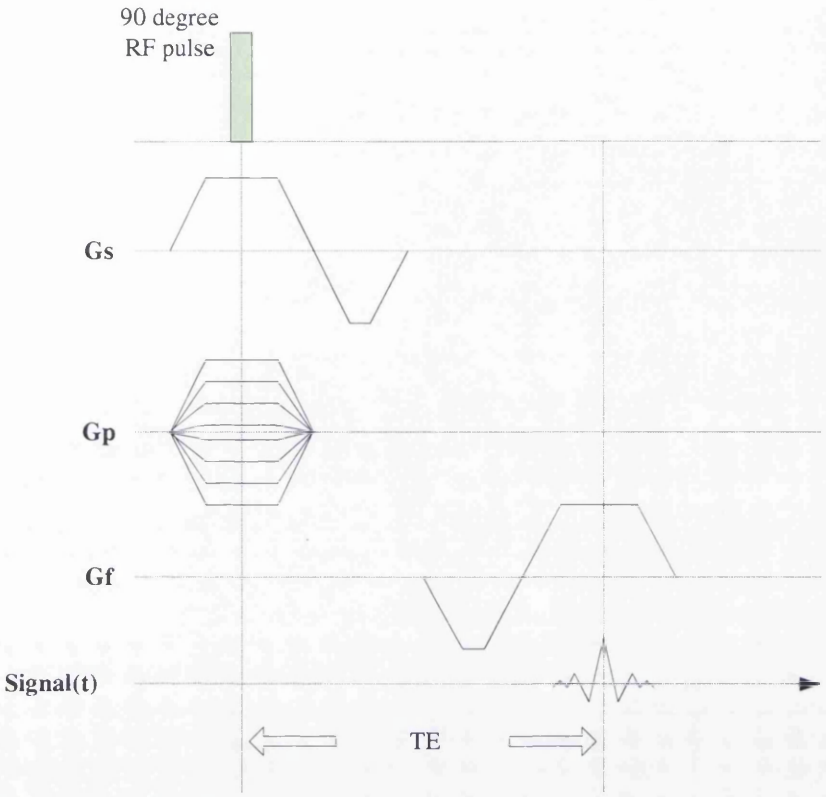

Figure 2.15 A classic gradient echo pulse sequence

Spin echo is another widely used pulse sequence. Spin echo is similar to the gradient echo, except that a 180° radio pulse is applied in the middle of the TE (Bernstein et al, 2004). The 180° radio pulse is called a refocusing pulse. It refocuses dephased traverse magnetisation caused by inhomogeneous magnetisation. Opposite magnetic gradients with identical amplitude are applied to compensate for the decay of MR signals in gradient echo techniques. However, magnetic field heterogeneity caused by other reasons, for example a metal implant, cannot by solved using this method. The refocusing pulse is applied in the middle of TE, splitting TR into two parts. In the first part of TE, some protons precess faster than others. The purpose of the 180° pulse is to rephase the spins of protons, causing them to regain coherence and thereby to recover transverse

magnetisation, producing a spin echo. In gradient echo, the rephasing lobe only compensates for the dephasing lobe. In spin echo, the refocusing pulse compensates for frequency variations due to magnetic field heterogeneity. Magnetic field heterogeneity is caused by many reasons, for example the imperfection of the main magnetic field, metal implant in the tissue, etc. Spin echo is considered as an ideal scan solution for the patients who have medical implants.

Figure (2.16) shows a basic spin echo sequence.

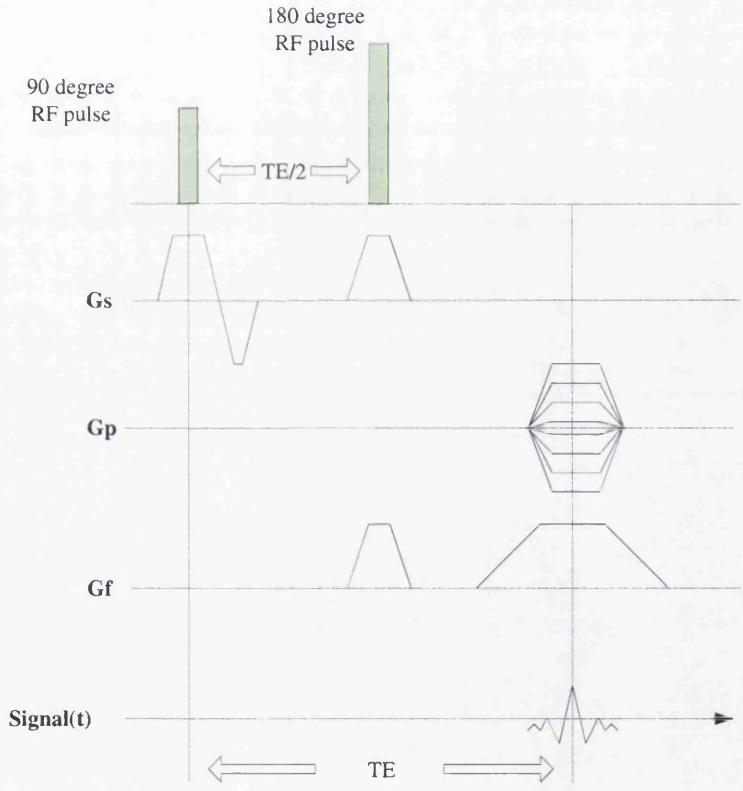

Figure 2.16 A spin echo pulse sequence. Spin echo technique is similar to gradient echo technique, except a 180° pulse in the middle of TE.

Chapter 3

Introduction to Cardiac MRI

3.1 The Functionality of the Heart

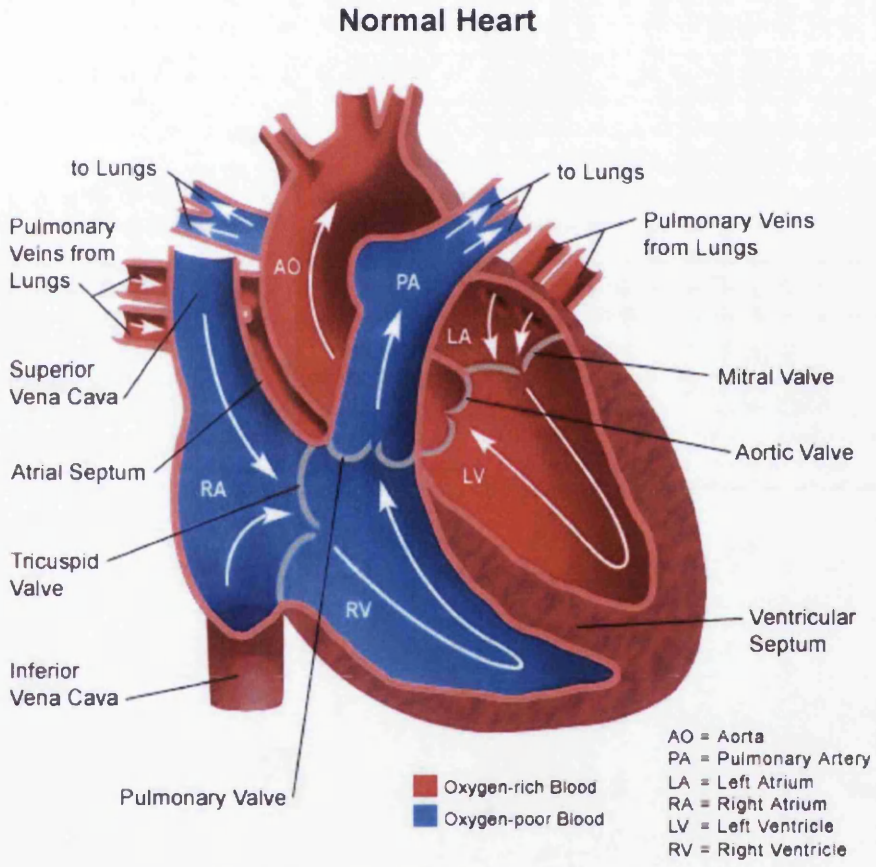

Figure 3.1. A four chambers view cardiac MRI image. [1]

A healthy heart weighs between 200 and 450 grams. Its size is slightly bigger than a fist. The heart lies in the mediastinum with its long axis oriented from the

[1] Source: http://www.gundluth.org

hypogastrium towards the right shoulder (Anderson & Becker, 1980). The heart comprises four chambers (figure 3.1). The upper chambers are called the right and left atria, and the lower chambers are called right and left ventricles. The right atrium connects to veins called the superior vena cava and the inferior vena cava. The blood from all parts of the body returns from the superior and the inferior vena cava to the right atrium. The right ventricle receives blood from the right atrium. During systole[2], the blood is forced out to the lung where it will be oxygenated. The oxygenated blood returns to the left atrium during systole through the pulmonary vein. The left ventricle receives blood from the left atrium and then sends it to every part of the body. This process repeats constantly. For each cycle, blood obtains nutrients and oxygen from the lung and then enters the left ventricle from the left atrium. The nutrients and oxygen along with the blood are sent throughout the body by the left ventricle. The waste from every part of the body is carried back by the blood from the right atrium to the right ventricle and forced back to the lung for exchange during cardiac contraction.

Normally, the walls of the atria are much thinner than those of the ventricles. This is most likely explained by the fact that the job of the ventricles is to pump blood into their respective ventricles which requires less force than pumping blood into circulation systems. The left ventricular has the thickest wall, which must create adequate pressure to force blood into the aorta (the largest artery in the body) and on through the blood vessels that constitute circulation (Solomom et al., 1990). A large

[2] The cardiac cycle is the sequence of events that occurs when the heart beats. Systole and diastole are two phases of this cycle. During systole, the ventricles compress. During diastole, the ventricles relax.

portion of known cardiac diseases which could severely damage health and may cause fatality, target the left ventricle (Julian, 1988; Timmis et al., 1997). Hence, studies on the left ventricle comprise a large proportion of cardiac MRI studies.

The blood flow in the heart is regulated by four valves. They are the mitral valve, aortic valve, tricuspid valve, and pulmonary valve. The mitral valve controls blood flow from the left atrium to the left ventricle. The aortic valve controls blood flow from the left ventricle to the aorta. During diastole, the mitral valve is open and the aortic valve is closed. The left ventricle receives blood from the left atrium. When the heart compresses, the mitral valve is closed, forbidding blood flow backwards to the left atrium. At this moment, the aortic valve is open, allowing high pressure blood flow to pass through the aorta to the body. The tricuspid valve and pulmonary valve perform exactly as the mitral valve and the aortic valve do. They cooperate to regulate the blood flow to the pulmonary system for gas exchange. Anatomically, each of the valves is held by a small muscle called a papillary muscle. In a cross-sectional MR image with an appropriate slice location, the papillary muscles can be clearly observed. However, in some situations, the papillary muscles may be "absorbed" by the myocardium during systole (figure 3.2). This has caused severe difficulty for precise cardiac motion studies, where manual or automatic segmentation is required.

The contraction of the myocardium pumps blood through the blood vessels and throughout the body, including the heart itself. Tiny vessels (diameter $< 300\,\mu m$)

cover the surface of the heart muscle forming a microcirculation system, making sure there is enough blood supply to this important organ of the human body. In some situations, the blood vessels may be blocked[3], causing ischaemic myocardium or myocardial infarction (Julian, 1988; Ball, 1995; Timmis et al., 1997). Ischaemic myocardium can be depicted with excellent contrast in advanced MRI techniques such as first-pass perfusion MRI (Saadi et al., 2000; Laddis et al., 2001; Wolff et al., 2004). Late contract enhanced MRI (see section 3.4) is widely used in the study of myocardial infarction (Wendland et al., 1999; Simonetti et al., 2001; Mahrholdt et al., 2003). At present, in the Glasgow Cardiac MR Unit, cardiac viability is assessed by visual evaluation of the wall motion abnormalities in combination with the presence or absence of late enhancement in the enhanced MRI images. Regions without late enhancement but with contractile dysfunction are considered as injured but still viable myocardium.

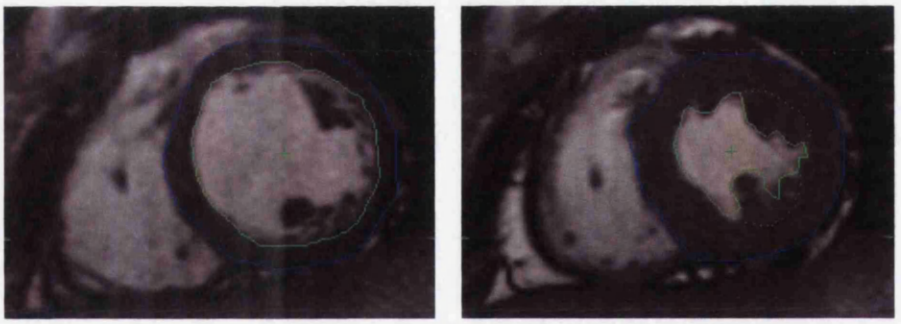

(a) (b)

Figure 3.2 Cross-section cardiac MR images. The contours of cardiac wall were defined manually in the end diastolic image (a) and the end systolic image (b). During the systole, papillary muscles move into cardiac wall, increasing the difficulty of the definition of endocardium. The dot line in image (b) was drawn by an expert, indicating the actual inner contour of cardiac wall.

[3] **Not only the small vessels can be blocked. The main coronary arteries with large diameters are often the cause of coronary artery disease.**

3.2 MR Anatomy of the Heart

MRI technology acquires cardiac images from any 2D plane in 3D space. The imaging planes are named with respect to the heart, such as the short axis plane and the long axis plane (figure 3.3a). The long axis plane which displays only the left ventricle and left atrium is called the two chamber long axis plane (figure 3.3b). The long axis plane, which shows both left and right ventricles and atria, is referred to as the four chamber long axis plane (figure 3.3c).

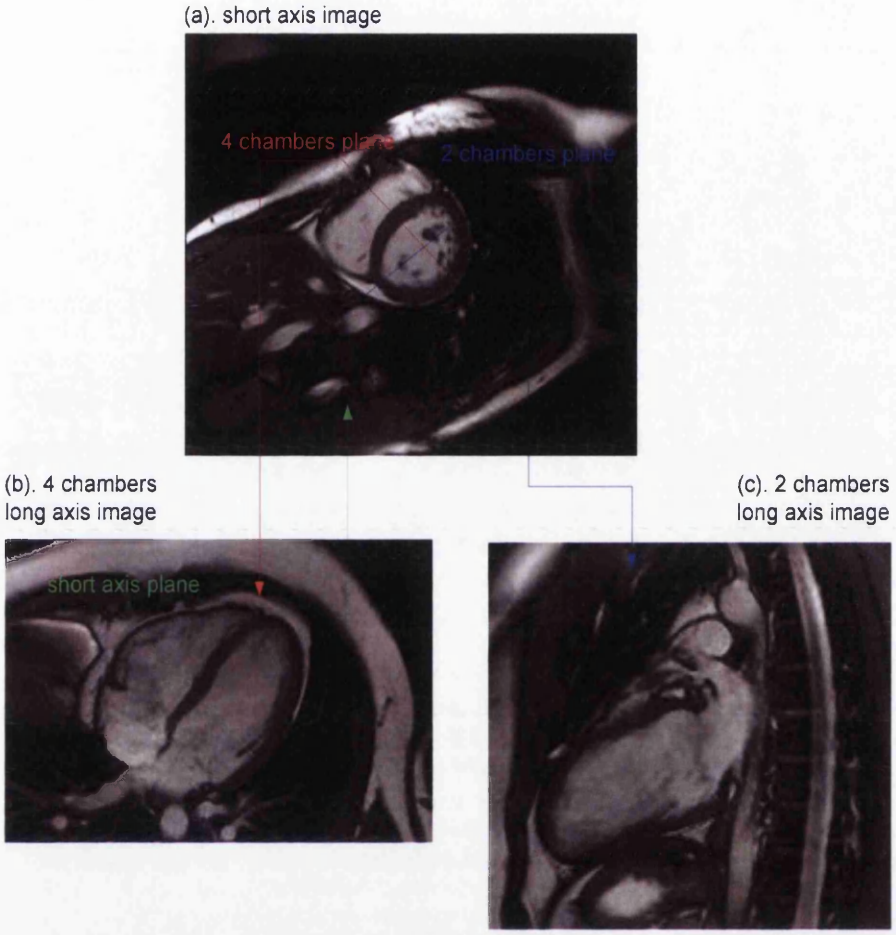

Figure 3.3 The MR imaging planes for cardiac studies. (a) the short axis imaging plane; (b) the 4 chambers long axis imaging plane; (c) the 2 chambers long axis imaging plane.

In the past decade, MRI technology has improved greatly. Ultrafast acquisition techniques along with the compensation for motion artifacts caused by tissue motion and flow were developed (Cohen & Weisskoff, 1991). The first cardiac cinematographic (cine) MR sequence was taken in 1987 (Aamer & Masataka, 2002). Since then, many ultrafast MRI techniques have been developed. The steady state free precession (SSFP) technique is a representative one (Gyngell, 1988). SSFP imaging

technique captures T2 / T1 weighted images[4], in which the myocardial structures can be distinguished clearly. As shown in figure 2.3, the brightest areas around the back and the stomach suggest the existence of the fat. Myocardium is shown as dark areas, as the blood pools in the mid-grey colour. The darkest areas are the bones or the air in the chest, which we will not be concerned with in our study. SSFP has been widely adopted in commercial MRI scanners, such as Siemens, Philips and GE systems. It is the state of the art at present. More details of SSFP will be discussed in the next section.

After the first acquisition of cardiac cine MRI images, many MR techniques have been developed, dramatically improving the assessment of the cardiovascular system. In the following sections, we will review several popular cardiac MRI techniques and their study methods. These techniques include the basic cardiac cine MRI, late contrast enhanced MRI which accurately depicts myocardial infarction, first pass perfusion MRI which locates ischaemic myocardium, and phase contrast MRI, a technique to measure blood flow velocity and indexing of aorta stiffness.

3.3 Cardiac Cinematographic MRI images

With the development of the MRI technique, it is possible to capture multiple images during a cardiac cycle, building cardiac cine MR images. Cine MRI is one of the most widely used cardiac MRI technique. At present, the ultrafast pulse sequence for cine

[4] T2/T1 weighted images exploit the T2 difference as well as the T1 difference between tissues. The contrast in a T2/T1 weighted image reflects the difference of T2/T1 ratio between tissues.

sequence acquisition is installed in most of the commercial MRI scanners. Although different names are used by different companies, for example, TrueFISP, TurboFLASH (Siemens Medical Solution), FIESTA (GE Medical systems) and balanced FFE (Philips Medical Systems), the ultrafast imaging techniques are based on a few underlying principles. The steady state free precession is one of them.

3.3.1 Steady State Free Precession

In the presence of the excitation pulse, the longitudinal magnetisation is rotated forward to the transverse plane creating the transverse magnetisation. The rotation angle, which is normally referred to as the flip angle, depends on the strength and duration of the excitation pulse. Following an excitation pulse with a flip angle of $\alpha°$, the T1 and T2 relaxation begins. In a significantly short TR, T, the second pulse with a flip angle of $-2\alpha°$ is applied to rotate the transverse magnetisation towards the negative transverse plane. If the pulses with the same strength but opposite polarity are repeated with an interval of 2T, the amount of transverse magnetisation at the middle of the interval will soon reach a ***steady state*** (Gyngell, 1988; Simonetti et al., 2001) (figure 3.4).

In the steady state, the amount of transverse magnetisation is decided by both T1 and T2. Imaging with SSFP exploits the differences of the T1/T2 ratio between tissues. A significant advantage of SSFP imaging is the very short TR, which significantly reduces the acquisition time. A practical pulse sequence of SSFP Siemens TrueFISP

imaging is shown in figure 3.5. Figure 3.6 shows a cardiac cine MR sequence produced using TrueFISP.

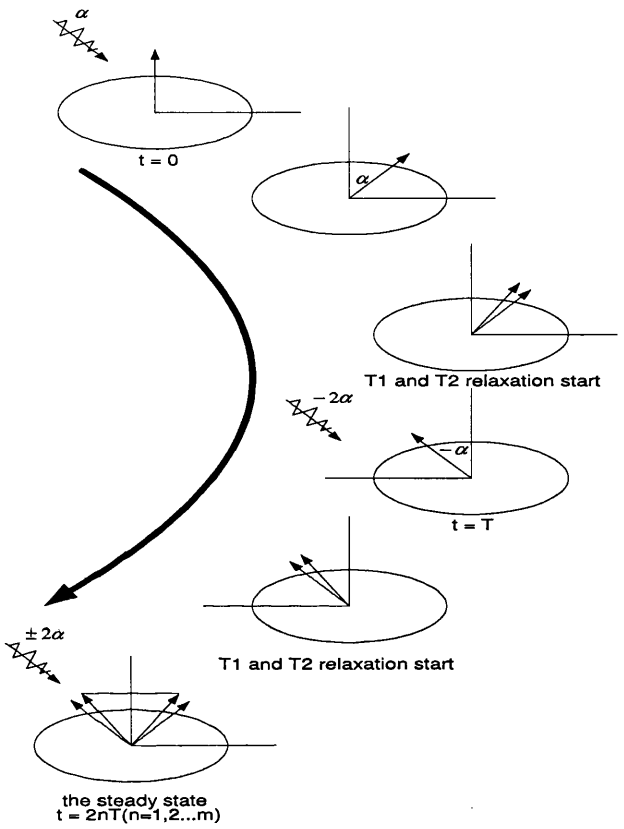

Figure 3.4[5] A α ° excitation pulse rotates the longitudinal magnetisation to the transverse plane by an angle of α °. After a short interval T, multiple excitation pulses with 2α ° and 2T bring the transverse magnetisation to the steady state almost immediately. Imaging with steady state technique is considered as an ultrafast imaging method.

SSFP technique is fast and able to produce multiple high resolution and high quality MRI images during the cardiac cycle. However, it still suffers severe artefacts if unexpected motion, for example respiratory motion, occurs. Hence, the cine cardiac MRI exam always requires breath-holding to ensure good image quality.

[5] **Source: (Mitchell, 1999)**

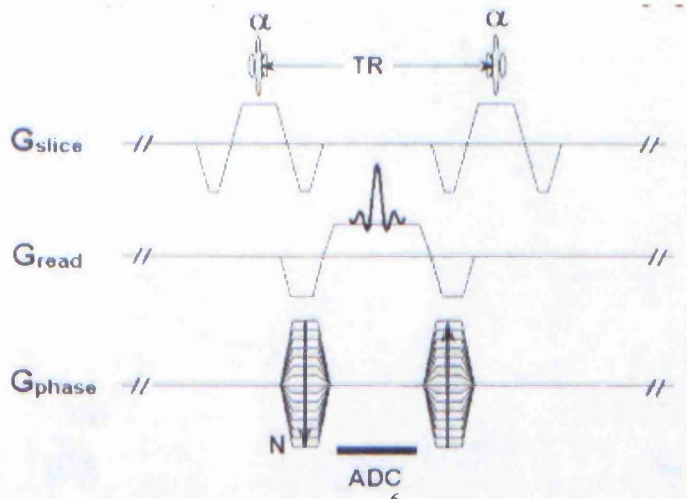

Figure 3.5 A trueFISP pulse sequence.[6]

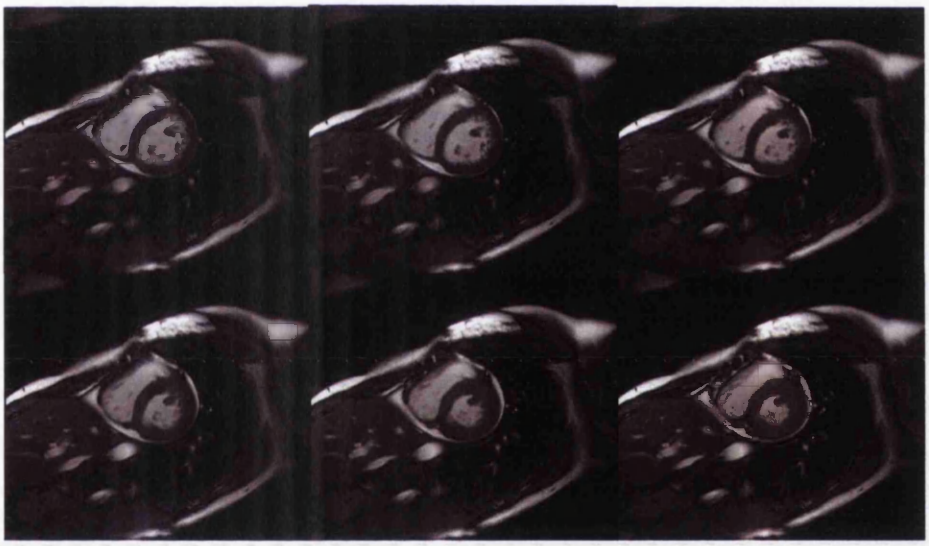

Figure 3.6 a Cross sectional TrueFISP cardiac cine MR sequence.

3.3.2 Quantitative study of cine MRI images

Cine cardiac MRI has become an important diagnostic tool. At present, the majority of the analysis of cardiac cine MR images is performed qualitatively and

[6] Source: Simonetti, et al., 2001

quantitatively. The qualitative assessment is an eye-ball assessment of the cardiac motion. The mainstay of quantitative assessment involves cardiac volumes and output measurement and the assessment of cardiac motion.

Cardiac volumes and output measurement

Figure 3.7 The thickness of a cross sectional MR imaging plane are normally 4-10mm thickness. There's a gap of 1~2mm between two image planes.

Multiple (typically 6–14) cross-section MR images are acquired on the imaging planes with a certain thickness to cover the entire myocardium. The location and thickness of the imaging plane is formally known as the ***slice location*** and ***slice thickness***. In practice, a small distance between two imaging planes is often set up to avoid the slice overlapping.

Cardiac contours are defined either manually or automatically in the end diastolic and the end systolic image of each slice. Mass volume (MV), the end diastole volume (EDV) and the end systole volume (ESV), can therefore be calculated using the modified Simpsons rule (equations 3.1 and 3.2). An extremely large EDV indicates a cardiac abnormality. One assumption is that the contraction of the dysfunctional myocardium cannot create sufficient blood pressure so that the myocardium has to expand itself to produce a stronger contraction.

$$V = \sum_i V_i \tag{3.1}$$

$$V_i = \begin{cases} A_i H_t + \dfrac{H_g (A_i + A_{i+1})}{2}, 0 \le i < N-1 \\ A_i H_t, i = N-1 \end{cases}_{7} \tag{3.2}$$

where A is the area of the defined contour, H_t is the slice thickness and H_g is the gap between two slices. N is the number of slices. The cardiac outputs are calculated from the cardiac volumes. The global ejection fraction (EF) and stroke volume (SV) are two parameters commonly used to define the cardiac outputs. EF and SV are calculated by using equation 3.3 and 3.4.

$$EF = \frac{EDV - ESV}{EDV} \times 100\% \tag{3.3}$$

$$SV = EDV - ESV \tag{3.4}$$

Table 3.1 lists a range of healthy cardiac parameters in respect to gender.

[7] In the equation, slice 1 is the 0th slice.

Gender-Related cardiac parameters[8]		
Parameter	**Males**	**Females**
LVEDV (ml)	168.5 ± 33.4	134.9 ± 19.3
LVESV (ml)	60.8 ± 12.0	48.9 ± 10.7
RVEDV (ml)	176.5 ± 33.0	130.6 ± 23.7
RVESV (ml)	79.3 ± 16.2	52.3 ± 9.9
LV Mass (g)	133.2 ± 23.9	90.2 ± 12.0
LVEF (ml)	64.2 ± 4.6	64.0 ± 4.9
RVEF (ml)	55.1 ± 3.7	59.8 ± 5.0
LVSV (ml)	107.7 ± 20.7	86.0 ± 12.3
RVSV (ml)	97.8 ± 18.3	78.3 ± 16.9

Table 3.1 Normal values for cardiac volumes and mass in adults based on the acquisition with SSFP.
LVEDV=left ventricle end diastole volume;LVESV=left ventricle end systole volume;
RVEDV=right ventricle end diastole volume; RVESV=right ventricle end systole volume;
LVEF=left ventricle ejection fraction;LVSV=left ventricle stroke volume
RVEF=right ventricle ejection fraction; RVSV=right ventricle stroke volume

Cardiac motion assessment

Cardiac cine MR images detail not only clear anatomic structure of myocardium but also the cardiac motion. The cardiac wall motion is studied quantitatively in different modalities. A widely used method is to compute the wall thickness difference between the end diastole and the end systole (Mahrholdt et al., 2003). A given number of radial lines start from the centre of gravity of the endocardium. Each of these radial lines has an intersection point with the endocardium and the epicardium, $P_{i,\ end}$ and $P_{i,\ epi}$. The displacement between $P_{i,\ end}$ and $P_{i,\ epi}$ represents the wall thickness in region i, Ti. The wall motion in region i, M_i can therefore be calculated by:

$$M_i = T_{i,\ systole} - T_{i,diastole}$$

[8] This table is modified from Khaled Alfakih, et al., "Normal Human Left and Right Ventricle Dimensions for MRI as Assessed by Turbo Gradient Echo and Steady Sate Free Precession Imaging Sequence", JMRI, 17:323-329, 2003.

The regional cardiac wall motion data can efficiently represented by a chart called a ***bulls-eye*** plot (figure 3.8).

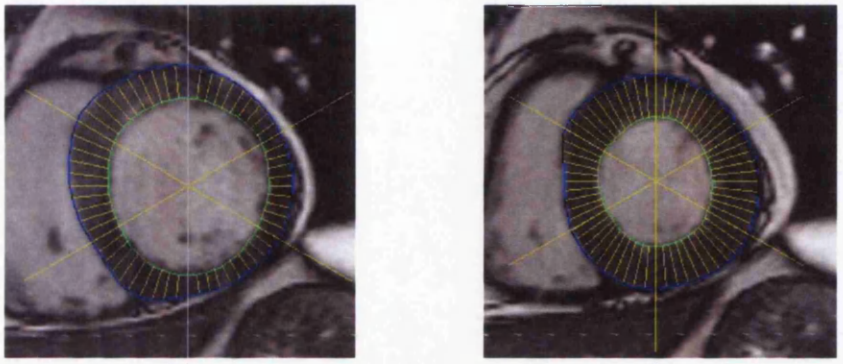

(a) (b)

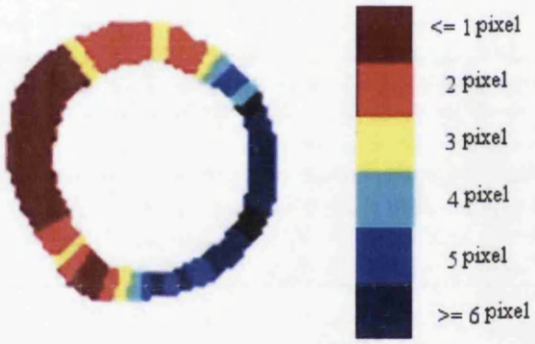

(c)

Figure 3.8 The measurement of the cardiac wall motion. The transmural lines start from the gravity center of endocardium are generated automatically in (a) the end diastolic and (b) the end systolic images. The wall motion can therefore be measured. The cardiac wall thickness was measured by Cardiowarp. The bulls-eye plot (c) was generated by using Matlab (MathWork).

Cardiac study based on the end diastole and the end systole image assumes linearity. However, cardiac contraction involves various forms of non-linear motion such as twisting, etc. Ideally, each image in a sequence should be studied correlatively to produce a more convincing result. For example, we could measure the non-linear

ejection fraction by defining the cardiac boundary through the whole cardiac cycle, building a volume-time curve. The slope of the best fitting line for the upstroke portion can be considered as the non-linear EF. Using the same method, it is also possible to measure the non-linear filling rate, which may be as important as the ejection fraction. Manual contour definition is time consuming, tedious and subjective. Using a traditional manual measurement, non-linear cardiac study could increase the diagnosis time dramatically. In this situation, an automatic contour definition algorithm is highly desired.

3.3.3 The partial volume effect

In theory, cardiac cine MRI can acquire images from any infinitely thin plane. But the signal to noise ratio may be too small to enable the production of a diagnostic quality image if the imaging plane is too thin. Conversely acquiring MRI images from a thick plane may amplify the so-called partial volume effect, increasing the difficulty of cardiac contour definition. The partial volume effect is referred to as the loss of contrast between two adjacent tissues in an image caused by insufficient resolution so that more than one tissue type occupies the same voxel (or pixel) (http://www.mr-tip.com). Mainly, the partial volume effect is caused by the slope of the cardiac wall. A thick plane has the longer slope which causes a smaller pixel intensity gradient in the cine MRI images. Beside the cardiac wall slope, the relatively static blood close to the cardiac wall and the tiny muscles on the cardiac wall will also contribute to the partial volume effect.

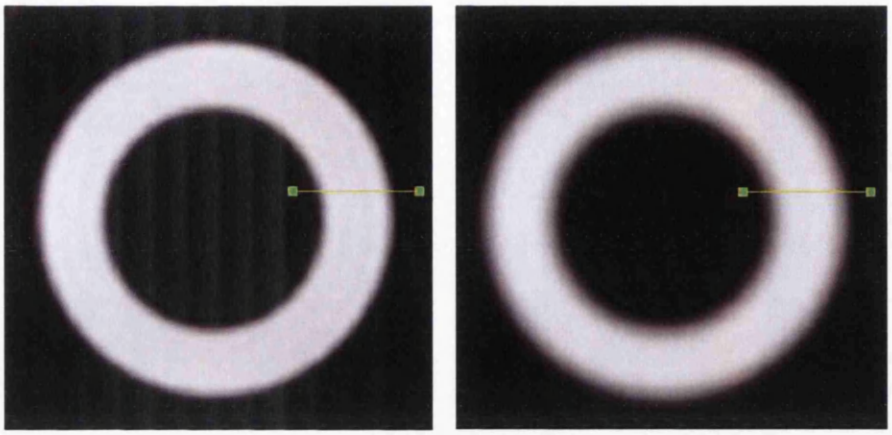

(a) (b)

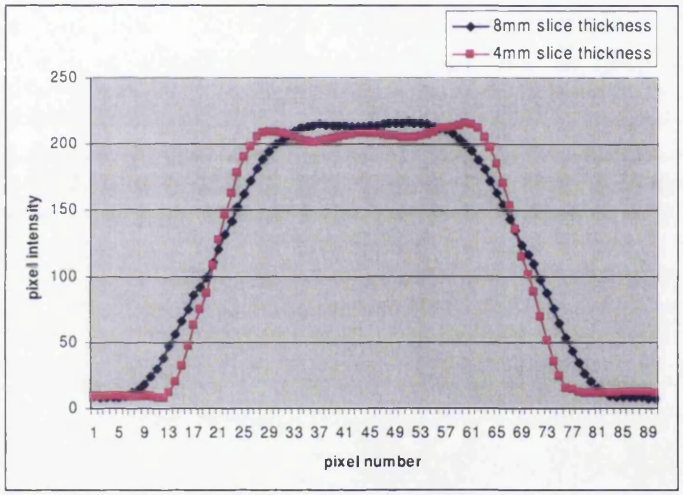

(c)

Figure 3.9 The cross sectional MR images of a cone phantom at the same slice location with a slice thickness of (a). 4mm and (b). 8mm. The partial volume effect is improved by using a smaller slice thickness. (c) shows the pixel intensity change along a reference line which passes through the inner and outer boundaries.

Practically, the plane thickness is selected to be 4mm and 8mm. Figure 3.9 shows the cross-section MRI images of a conical phantom with a slice thickness of 4mm and 8mm. With the same slice location, the image with a 4mm slice thickness is clearly sharper than the image with an 8mm slice thickness, which reduces the difficulty of

manual contour definition. With the same gap, a smaller slice thickness could reduce the interpolation error while measuring the volume and the ejection fraction. But to acquire MRI images with small slice thickness requires a large number of images in order to cover the myocardium. To study those images manually could be very time-consuming and subjective. Once again, this indicates that an automatic or a semi-automatic segmentation algorithm can play a rather important role to improve the efficacy of MRI.

3.4 Contrast Enhanced MRI

As with other parts of the human body, the myocardium needs a blood supply to maintain function. The heart has its own system of vessels. It is supplied with blood delivered by the two coronary arteries, the right coronary artery and the left coronary artery. Both coronary arteries have several major branches and numerous microscopic branches. Many of the branches open directly to the cardiac chambers. For many reasons such as ageing, smoking, unhealthy diet, etc., blockages could develop in the coronary arteries, resulting in ischaemic heart disease or even irreversible myocardial infarction.

Ischaemic heart disease causes the cardiac motion abnormality. However, a recent study shows that the assessment of cardiac motion cannot be used to rule out myocardial infarction due to the so-called the "neighbour effect" (Mahrholdt et al., 2003). Figure 3.10 shows a typical result of the neighbour effect.

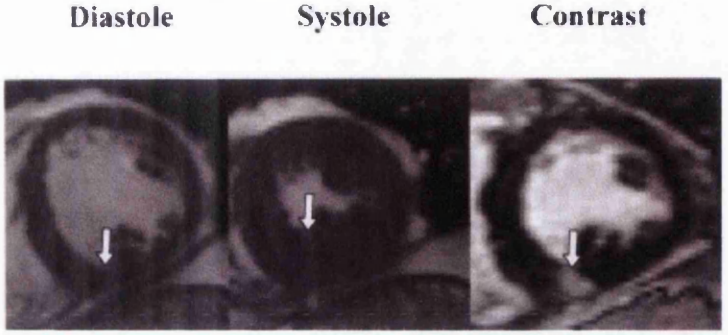

Figure 3.10 Significant wall thickening can be observed despite the presence of myocardial infarction. The contrast image depicts the location and the size of myocardial infarction (the bright region in myocardium).

At present, many myocardial infarction studies involve the use of MRI with contrast agent, such as gadolinium-diethylenetriamine pentaacetic acid (Gd-DTPA) (Wendland et al., 1999). In patients with an acute myocardial infarction, hyper enhancement is seen in MR images more than a few minutes (e.g. 10 minutes) after injection of the contrast enhancement agent (figure 3.11). This method is referred to as late contrast enhanced MRI.

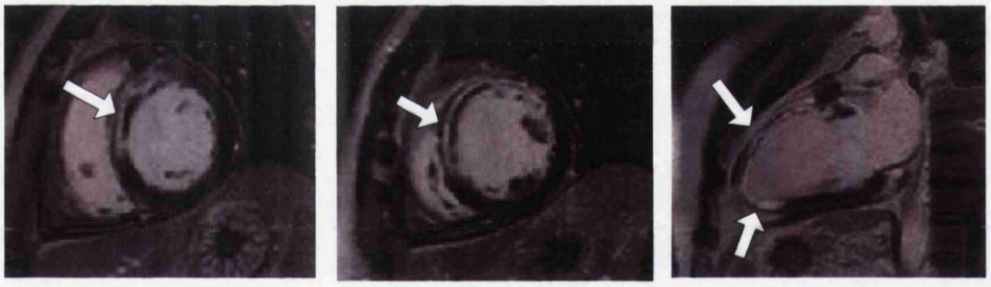

Figure 3.11 Myocardial infarction is highlighted by late contrast enhanced MRI

The underlying principle of the late contrast enhanced MRI is straightforward. Gd-DTPA is washed into the heart by the blood flow after the injection. It passes through the healthy myocardial wall freely via the microcirculation system but it is blocked by the myocardial infarction, where the circulation system is not properly functional. A

high concentration of Gd-DPTA in the infarction produces a localised change in magnetic field, changing the property of T1, resulting in a different contrast compared to the healthy myocardium

A late contrast enhanced MRI image is T1 weighted. Therefore, it can be captured by either the spin echo sequence or the gradient echo sequence (chapter 2, section 2.2.3). However, to design a high standard pulse sequence for late contrast enhanced MRI, two practical questions need to be answered.

1. How to maximise the contrast difference between the myocardium with and without the contrast agent.
2. How to acquire sufficient MR signals efficiently.

The answer to the first question is a 180° radio frequency pulse which is often referred to as a ***preparation pulse***.

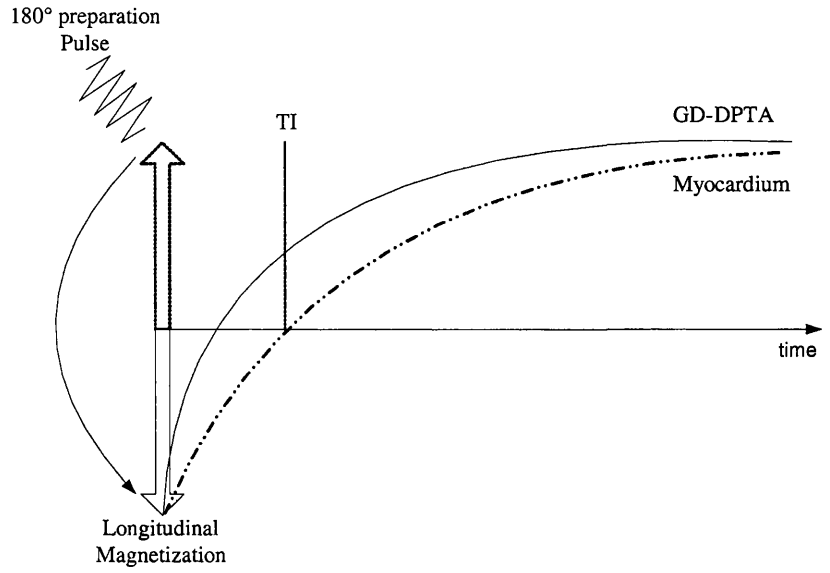

Figure 3.12 180°preparation pulse null normal myocardium

The 180° preparation pulse doubles the effects of the 90° pulse, inverting the longitudinal magnetisation completely to the negative longitudinal axis. After inversion, the longitudinal magnetisation starts recovering. Following the 180° pulse, T1 relaxes. At time *t*, the longitudinal magnetisation will reach 0 (figure 3.12). *t* is referred to as the inversion time (TI). With the TE carefully selected around time TI, good visual contrast can be achieved by nulling the normal myocardium.

The imaging of myocardial infarction normally requires breath-holding to minimise the motion artifacts. An ultrafast pulse sequence is needed to ease the challenge, especially for elderly patients. However, following the 180° preparation pulse, a time delay is required to allow the T1 relaxation, increasing the difficulty of the fast acquisition technique. In the Glasgow Cardiac MR Unit, we implement Siemens

TurboFLASH imaging techniques specifically designed for the late contrast enhanced MR imaging.

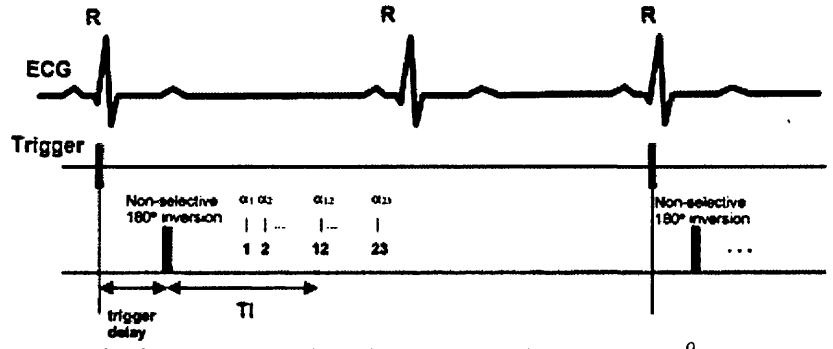

Figure 3.13 A ECG gated TurboFLASH pulse sequence. [9]

TurboFLASH is ECG gated and triggered by an R wave. A variable trigger delay allows acquisition of the image data at the end diastole. After the preparation pulse, a time delay is used to allow T1 relaxation. TurboFLASH is relatively fast because it partitions the recovery of the longitudinal magnetisation in many segments. For each segment, an MR signal is acquired to build a line of the k-space. As discussed in chapter 2, the centre of k-space contributes to the contrast of the constructing image. In the TurboFLASH sequence TI, which nulls the normal myocardium, is set to be at the center of the k-space, ensuring that good contrast between the injured myocardium and the healthy myocardium can be achieved. The number of k-space lines constructed during a T1 relaxation time is limited by the repetition time TR and the duration of diastole. In Siemens' implementation, a small flip angle is used to achieve 8ms TR. 23 k-space lines are constructed in 184ms which is fast enough to be insensitive to cardiac motion in the middle of diastole. The pulse sequence is triggered every other cardiac cycle to acquire sufficient MR signals. With this

[9] Source: [Simonetti, et al., 2001]

implementation, image acquisition necessitates a typical breathhold duration of 12 cardiac cycles (≈ 10s). Figure 3.13 shows a TurboFLASH pulse sequence.

Late contrast enhanced MRI is simple, reliable and able to produce high quality and high resolution images. It has become an important tool to assess myocardial viability. Recent studies suggest that Gd-DPTA enhancement closely matches the infarcted area in dogs (Simonetti et al., 2001) and other modalities such as Positron Emission Tomography (PET) (Klein et al., 2002) and Single Photon Emission Computerised Tomography (SPECT) (Ibrahim et al., 2003).

The contrast enhanced area of the myocardium is found to be irreversible. However, the area without contrast enhancement is not necessarily the healthy myocardium. In some situations, blood vessels were only partially blooded. The blood delivered to the heart is insufficient to maintain the proper function, resulting in ischaemic myocardium. Locating ischaemic myocardium is clinically important as it could turn into irreversible myocardial infarction without proper medical treatment. The location of the ischaemic myocardium can be determined by the combined study of cardiac motion using cine MRI and late contrast enhanced MRI. Alternatively, it can be located using advanced MR imaging such as first-pass perfusion MRI.

First past perfusion is another form of contrast enhanced MRI technique. MR images are acquired immediately after injection of the contrast enhancing agent, for example Gd-DPTA. Ultrafast MRI sequences are able to image multiple slices during each

cycle in order to obtain images of the passage of Gd-DPTA into the left ventricular myocardium (Saadi et al., 2000; Laddis et al., 2001; Wolff et al., 2004).

Areas of reduced perfusion appear as darker areas, while normal myocardium enhances during the passage of gadolinium (figure 3.14). In order to show up differences in myocardial perfusion efficiently, pharmacological stress is achieved using adenosine. This increases the blood supply to the normal myocardium by 2-3 times by causing smooth muscle relaxation in the coronary arteries via the adenosine A2a receptors. This process is impaired in coronary artery disease with endothelial dysfunction as there is little or no increase in flow in these arteries, increasing the difference in perfusion between normal and ischaemic myocardium.

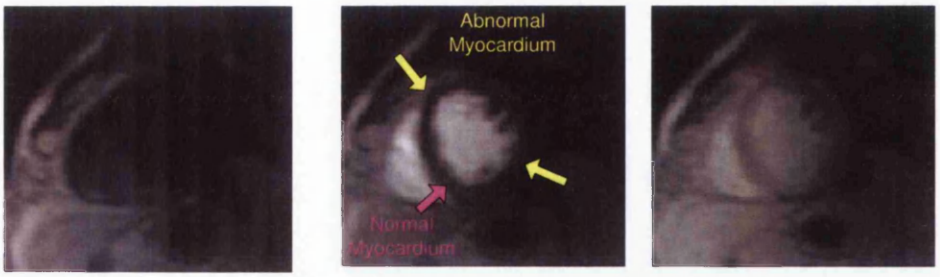

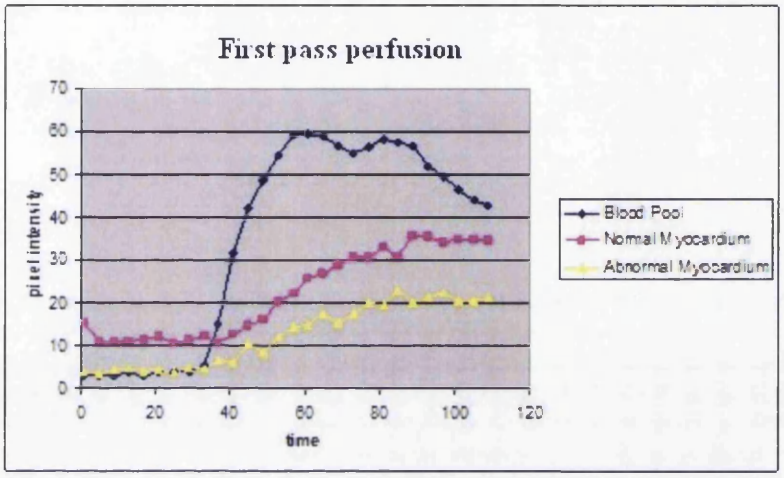

Figure 3.14 The Analysis of first pass perfusion MR images. The images were acquired in the short axis view after injecting the contrast enhancing agent, Gd-DPTA. The arrows point to the normal and the abnormal myocardium. The perfusion curves were produced by using Angus (Siemens medical systems).

First-pass perfusion appears to be a promising technique for the quantitative assessment of ischaemic myocardium. It has been validated using other imaging modalities such as PET, SPECT (Penzkofer et al., 1999) and animal models (Epstein et al., 2002). However, the quantitative or semi-quantitative analysis of first-pass perfusion MR images is facing several significant difficulties, limiting its clinical application. The technical challenge of the study of first-pass perfusion MRI and our solution will be presented and discussed in chapter 7.

3.5 Phase contrast MRI

There has been much interest recently in the relationship between arterial stiffness and cardiovascular disease, including hypertension and increased left ventricular mass (Blacher et al., 1999; London et al., 2001). Arterial stiffness may be measured using a variety of invasive and noninvasive methods. Pulse wave velocity (PWV) is increasingly used to identify patients at increased cardiovascular risk (Mackenzie et al., 2002). According to the Moens-Korteweg equation (Nichols et al., 1998),

$$PWV = \frac{1}{\sqrt{\rho(1/\varepsilon + 2R/Eh)}}$$

where ε denotes the modulus of fluid elasticity, R is the inner radius of the vessel, E is the modulus of wall elasticity (Young's modulus), and h is the vessel thickness, the pulse wave velocity, which is related to the square root of the elasticity modulus, rises in stiffer arteries.

The elastic properties of the aorta and central arteries are important determinants of cardiovascular coupling, and the PWV measured along the aortic pathway appears to be most clinically relevant. Arterial stiffening occurs normally with ageing (Rogers et al., 2001) but also correlates with the prevalence of atherosclerosis.

Pulse wave velocity is the speed at which the forward pressure is transmitted from the aorta through the vascular tree. The more rigid the wall of the artery, the faster the wave moves. Clinically, a simpler equation is used to calculate PWV:

$$PWV = \frac{\Delta dist}{\Delta t} \tag{3.5}$$

where $\Delta dist$ is the distance traveled by the blood flow and Δt is the time of the traveling. Traditionally, two simultaneous Doppler flow tracings are taken at the aortic arch and the femoral artery in the groin with a Doppler unit. The travel time Δt can therefore be measured. The distance $\Delta dist$ travelled by the blood flow is measured over the body surface as the distance between the two recording sites. The major difficulties are:

1. The central arteries are inaccessible and therefore the nearest superficial arteries are used.
2. The actual distance $\Delta dist$ cannot be accurately estimated.

Using MRI technology with the so-called phase contrast pulse sequence, a more direct measurement of PWV is possible (Gao & Mark et al., 2004).

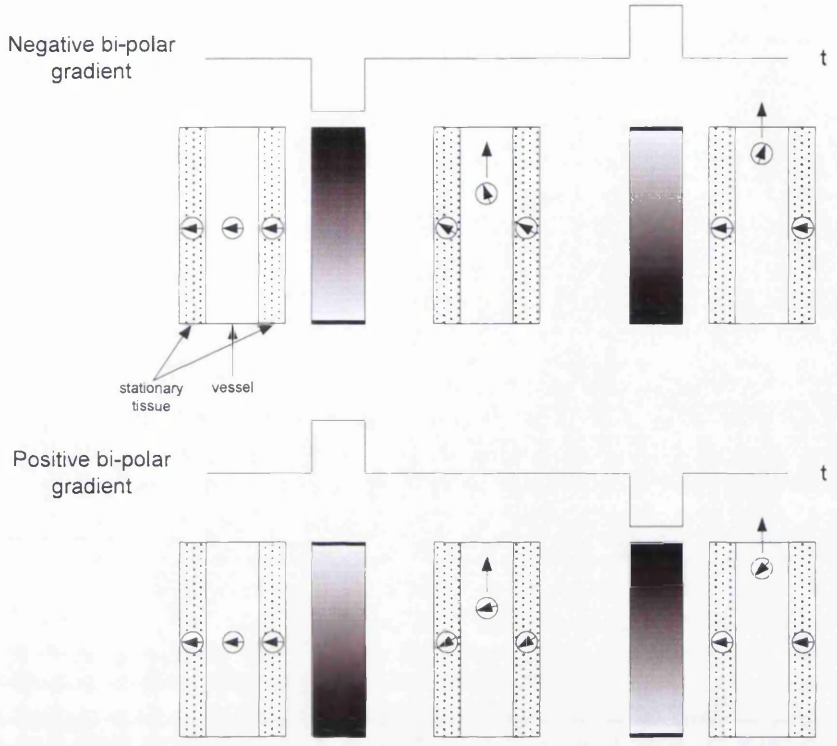

Figure 3.15 The bipolar gradient pulse does not affect the stationary spins. However, the phase shift of flow spins is added to produce a net magnitude.

Phase contrast MRI (PCMRI) measures blood flow velocity using a bi-polar gradient which has both a negative and positive lobe (Pelc et al., 1991). A positive bipolar gradient pulse has the positive lobe first and a negative bi-polar gradient has the negative lobe first. The positive and the negative lobes have the same duration and amplitude. In the external magnetic field, protons precess with the Larmor frequency and phase. When the negative part of the bi-polar magnetic gradient is on, protons in the neighboring stationary tissue and the flowing blood spin with an equal frequency and phase shift. After a short interval *t*, the positive magnetic gradient is on to cancel the effect to the stationary tissue. However, the flowing blood has separated from its original neighbours to be in a different magnetic field strength during the application

of the positive magnetic gradient (figure 3.15). The result is that the phase of the stationary tissue will return to zero while the flowing blood will accumulate a phase shift proportional to the distance moved. In theory, the positive and the negative bi-polar gradient should have the same effect to stationary spins but opposite effects to flowing spins.

PCMRI generates a pair of image sequences in which the first has a positive bi-polar magnetic gradient and the second a negative bi-polar magnetic gradient. The raw data from the two images are subtracted to produce a sequence of PCMR images. In this case, MR signals from stationary spins are cancelled while signals from flowing spins are added to produce a net magnitude, which is proportional to the velocity of flow. Regions of interest are placed on PCMR images. Mean pixel intensities are calculated to establish intensity curves over time. The time shift t is calculated using various methods such as foot to foot method (Vulliemoz et al., 2002) and best correlation method (Rogers et al., 2001). (For more details, this will be discussed in chapter 7, section 7.1.2) In our study, PCMRI uses a velocity sensitivity 150m/s, which will be sufficient to produce accurate time shift t (Roger et al., 2001; Vulliemoz et al., 2002). The aortic length is measured using a high resolution aortic MR image from the longitudinal view. PWV is therefore calculated from equation 3.5.

MRI measurement permits potentially direct non-invasive pulse wave analysis of the central vessels allowing greater understanding of central haemodynamics and their impact on the risk and progression of vascular disease. This represents a clear

improvement on current methods using Doppler which is operator dependant and makes inaccurate assumptions regarding distance of blood flow. Clearly, the measurement of PWV using MRI could be an improvement to arterial studies.

Chapter 4

Image Registration

4.1 Background

Image registration is a fundamental image processing technique. Basically it is the process of finding a transformation function T that aligns one image to another. In the past decades, image registration was successfully applied in various areas, including:

- **Medical image analysis**. A common medical application of image registration is so-called multimodal registration, where images of the same subject have been taken by different sensors, for example, CT, PET, SPECT and MRI. Different types of imaging technologies have their advantages and disadvantages. Cross-examination often requires the identification between two types of images. The image registration technique is also applied frequently in functional MRI studies, where the misregistration between images over time needs to be corrected. In recent years, robust image registration techniques have been employed to track cardiac motion.
- **Remotely sensed data processing**. Remotely sensed data processing is among the earliest applications of image registration. It is valuable for both military and

civilian applications. For example, analysis of satellite images of the same region in different periods can reveal important information such as geographical change or urban growth

- **Computer vision and pattern reorganization**. Image registration has been successfully used in different tasks such as object recognition, 3D modeling, motion detection, etc.

Based on its application, the image registration technique can be divided into four categories (Brown, 1992):

1. Multimodal registration: the medical application of the multimodal registration has been described briefly above. Another example of the multimodal registration is the remotely sensed data processing. Images from different sensors on the satellites focus on different geographical aspects.
2. Viewpoint registration: where the same subject is captured with the same sensor at the same moment but from a different position. In computer vision, registering two images of the same object from two similar sensors with a defined angle can reveal the depth of the object from the disparity maps and a 3D model of this object can therefore be built.
3. Temporal registration: where the same subject is captured with the same sensor from the same viewpoint, but at different times. In medical imaging, temporal registration is used to track the motion of tissues, for example, temporal registration is adopted to track and correct for the respiration motion in the first-

pass cardiac MRI analysis. In the application of computer vision, temporal registration is used to detect the motion of objects and compute the motion velocity.

4. Template registration: where the template is built statistically from a large set of images taken from the same or similar sensors.

The challenge of multimodel image registration is the variety of pixel intensity (Maes et al. 1997). For different imaging modalities, the same object could appear in different color. Accurate alignment of those images often requires a similarity measurement function which is insensitive to the change of pixel intensity. The pixel intensity variety involved in the viewpoint, temporal and the template image registration is modest. However, the object motion or deformation may be significant. The research priorities of those registration algorithms are the efficiency and the accuracy.

One objective of this work is to track the cardiac motion during systole, which is relies on a temporal image registration algorithm. Before the future discussion, a full understanding of image registration is vitally important. In this chapter, I will introduce the image registration technique from the theoretical level to the practical implementation.

4.2 Theory of image registration

Given two images I and J, image registration finds the transformation functions such that:

$$I`(x, y) = g(I(f(x, y))$$

where

$$\gamma = \min \delta(I`, J)$$

δ is a predefined similarity measurement function. γ is the possible minima of the function δ.

The transformation functions may contain a 2D spatial transformation f and a 1D pixel intensity transformation g. A simple example of the pixel intensity transformation is ***contrast stretching***. The 1D function g is not always necessary since the shape is the major concern in many studies.

4.3 Transformation

A transformation is a function that maps points from one image to another. Common transformations include rigid transformation, affine transformation and non-rigid transformations.

Rigid transformation is the oldest and the most familiar form of transformation. The two-dimensional rigid transformation has four parameters, the vertical and horizontal translations, the rotation angle and the scaling factor. The affine transformation is more complicated but has more degrees of freedom compared to the rigid transformation. Non-rigid transformations are often in pixel or sub-pixel level, which means for each pixel in the image, a vector is assigned to find its corresponding pixel in the other image. Obviously, the non-rigid has the highest degrees of freedom. In recent years, it has been widely applied in medical image analysis to correct for the elastic motion of tissues.

4.3.1 Rigid Transformation

If the distances and the angles between all the points on the object do not change after a transformation, the transformation is referred to a rigid transformation. A rigid transformation processes three degrees of freedom in a 2D plane or six degrees of freedom in a 3D space. In this study, we will focus on the 2D transformation only.

The three degrees of freedom of the rigid transformation in a 2D plane include two translations along the two axes and the rotation around a point. Given a point A(x, y), its translation into point A`($x$`, y`) can be described as:

$$\begin{aligned} x` &= x + t_x \\ y` &= y + t_y \end{aligned} \tag{4.1}$$

where the t_x and t_y are the translation displacement for axes x and y.

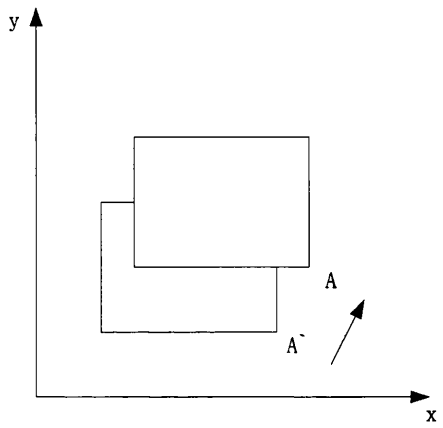

Figure 4.1 Translation of a rectangle. Distances between points in the rectangle did not change.

The translation is the most simple transformation form. The rotation is more complex. Knowing the rotation angle α, the position of $x`$ and $y`$ are defined by:

$$\begin{pmatrix} x` \\ y` \end{pmatrix} = \begin{pmatrix} \cos\alpha & -\sin\alpha \\ \sin\alpha & \cos\alpha \end{pmatrix} \begin{pmatrix} x \\ y \end{pmatrix} \tag{4.2}$$

This can be rewritten as:

$$x` = y\sin\alpha + x\cos\alpha$$
$$y` = y\cos\alpha - x\sin\alpha$$

From equation (4.1) and (4.2), a rigid transformation can be described as:

$$\begin{pmatrix} x` \\ y` \end{pmatrix} = \begin{pmatrix} t_x \\ t_y \end{pmatrix} + \begin{pmatrix} \cos\alpha & -\sin\alpha \\ \sin\alpha & \cos\alpha \end{pmatrix} \begin{pmatrix} x \\ y \end{pmatrix}$$

The rigid transformation had been widely used in remotely sensed data registration, for example, the geographical image registration. The low computational complexity is a

clear advantage of the rigid transformation but its applications in medical imaging are rather limited because most of tissues are elastic and their motions are non-rigid.

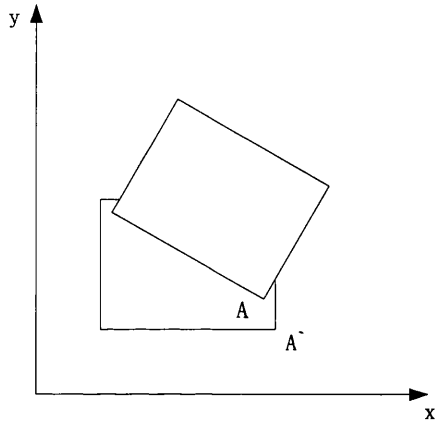

Figure 4.2 2D rigid transformation includes two degrees of translation and one degree of rotation.

4.3.2 Affine Transformation

The rigid transformation is the most basic form of transformation. However, in most situations, a rigid transformation cannot satisfy the requirement. Other forms of transformation are required. Affine transformation is more complicated and flexible than rigid transformation. A 2D affine transformation includes the 3 degrees of freedom, two degrees of translation and a rotation which has already been included in the rigid transformation. In addition, the structure deforming transformations such as scaling and shearing are also allowed in an affine transformation. The scaling and shearing are described mathematically by (4.3) and (4.4)

$$\begin{pmatrix} x` \\ y` \end{pmatrix} = \begin{pmatrix} s_x & 0 \\ 0 & s_y \end{pmatrix} \begin{pmatrix} x \\ y \end{pmatrix} \tag{4.3}$$

where s_x and s_y are the scaling factor along x and y axes.

$$\begin{pmatrix} x` \\ y` \end{pmatrix} = \begin{pmatrix} 1 & shear_x \\ shear_y & 1 \end{pmatrix} \begin{pmatrix} x \\ y \end{pmatrix} \tag{4.4}$$

where $shear_x$ and $shear_y$ are distortions of pixels along axes x and y.

(4.5) is the general description of a 2D affine transformation.

$$\begin{pmatrix} x` \\ y` \end{pmatrix} = \begin{pmatrix} t_x \\ t_y \end{pmatrix} + \begin{pmatrix} s_x & shear_x \\ shear_y & s_y \end{pmatrix} \begin{pmatrix} x \\ y \end{pmatrix} \tag{4.5}$$

After an affine transformation, the distances and angles between points in the object change. But the parallel lines in the object will remain parallel.

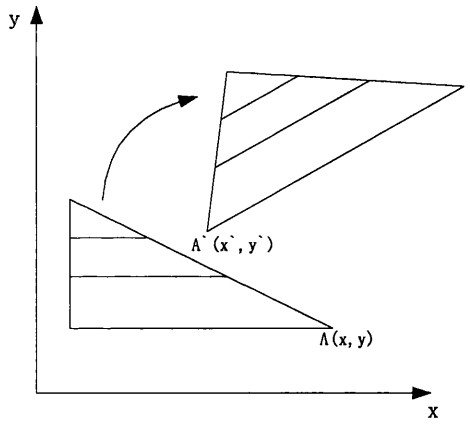

Figure 4.3 Affine transformation does not reserve the angles and distances between points. But parallels lines will remain parallel after the transformation.

Affine transformation is frequently employed to register the global motion of the source object. For example, in medical image registration, affine transformation could be used to compensate the misregistration caused by patient motion during the image acquisition.

But the natural tissue motion such as cardiac motion is too complex to be described accurately by affine transformation. To register the tissue motion, a more complex form of transformation, the non-rigid transformation is introduced.

4.3.3 Non-rigid transformation

Image registration is playing a more important role in medical image analysis as medical imaging technologies such as CT and MRI rapidly improve. A non-rigid transformation model is always required to accurately register the medical images.

A popular approach of non-rigid transformations is the free-form deformation (FFD) model. The basic idea of the FFD is to deform an object by manipulating an underlying mesh of control points based on some forms of constraint, for example, cubic B-splines. The mesh deforms as the control points move. A weighted interpolation map is built to recalculate the intensity for every pixel in the image using the warping algorithm such as two pass warping and three pass warping (Gomes et al., 1999). Figure 4.4 shows an example of B-spline based FFD.

The other widely recognized method of non-rigid transformation is called optical flow. Unlike FFD, optical flow considers the transformation as a form of motion instead of deformation. If a series of images are acquired over time, and there are moving objects in the images, the calculation of optical flow finds a velocity vector $\boldsymbol{T}$ for each pixel in the

image, building a velocity vector map with the same resolution as the input images. Given two images, I and I`, it is possible to digitally warp the image I to match the image I` using the calculated velocity vector map (4.6).

$$I``(x, y) = I(\boldsymbol{T}(x, y)) \tag{4.6}$$

where $I``$ is the warped version of image $I`$. $\boldsymbol{T}$ is the velocity vector map calculated from image $I$ and $I`$.

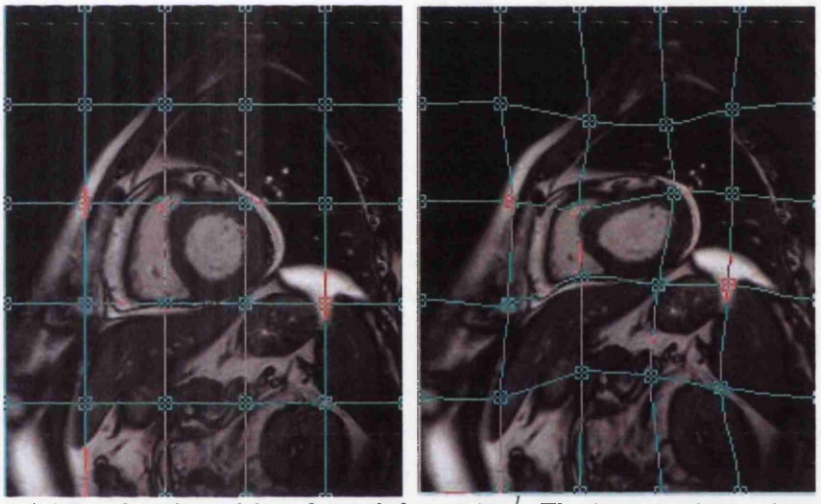

Figure 4.4 B-spline based free form deformation[1]. The intersection points of the grid indicate the locations of the control points. The warping algorithm such as two-pass warping builds weighted interpolation map, which is used to calculate the new intensity of each pixel in the image.

A velocity vector can be either an integer or a floating-point number. A sub-pixel level accuracy could be achieved when a floating-point velocity is used. Pixel intensity in a fractional position can be calculated using interpolation algorithms, for example, the bi-linear interpolation.

[1] **The images are the screen shots of an image processing software, Paint Shop Pro Ver8.0 (Jasc Software)**

Bilinear interpolation explores four points neighboring the point *p(a, b)*, and assumes that the brightness function is bilinear in this neighborhood. Its calculation is shown in figure 4.5.

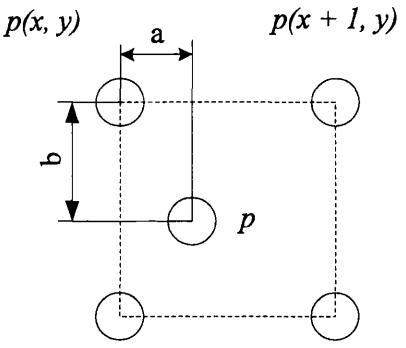

$$p = (1-b)\{(1-a)p(x, y) + ap(x+1, y)\} + b\{(1-a)p(x, y+1) + ap(x+1, y+1)\}$$
$$a \in [0,1), b \in [0,1)$$

Figure4.5 Calculation of bilinear interpolation.

FFD is frequently used in functional MRI image registration, where the misregistration of brain is mainly caused by patient movement. In this work, we chose an optical flow based non-rigid image registration technique since a major objective is to extract cardiac motion during a cardiac cycle.

Non-rigid transformation has so far the largest number of degrees of freedom. However this significantly increases the number of the similarity measurement which is time-consuming. The exhausted searching may take hours to align two images with the matrix

size of 256x256. Increasing the efficiency as well as the accuracy has become one of the major directions in the research of image registration.

4.4 Similarity measurements

To bring two images into spatial alignment, the transformations are applied to one of the two images. The purpose of the similarity measurements is to evaluate how well the two images match by returning a value (Freire et al., 2002).

In this chapter, we will discuss three most widely used measurement techniques, mean square error, cross-correlation and mutual information.

4.4.1 Mean Square Error

Similarity measures of image registration are calculations used to define the similarity between two images under certain transformations. One of the earliest methods is mean square error (MSE).

MSE involves taking a template from one image and then computing the MSE between the template and various **2-d sections** from the second image.

$$MSE = \frac{\sum \sqrt{\left(I(x,y) - I`(x,y)\right)^2}}{MN}$$

where M and N is the dimensions of the 2D matrices, $x\varepsilon(0,M]$, $y\varepsilon(0,N]$, $I(x,y)$ and $I`(x,y)$ are pixel intensities range from 0 ~ 255 for a 8 bits image.

MSE is straightforward, fast and easy to be implemented by both hardware and software. But it does not work well when the pixel intensity is significantly different between the two images.

There are other measures similar to MSE which have been reported as used in image registration. For example, the sum of the absolute differences (SAD):

$$SAD = \sum_x \sum_y |I(x,y) - I`(x,y)|;$$

the sum of difference square (SDS):

$$SDS = \sum_x \sum_y |I(x,y) - I`(x,y)|^2$$

All these techniques share similar principles and will produce similar results.

MSE measures the similarity based on the assumption that the two images are completely the same. It is straightforward and computationally efficient. But any forms of noise or distortion could affect the results significantly (figure 4.6).

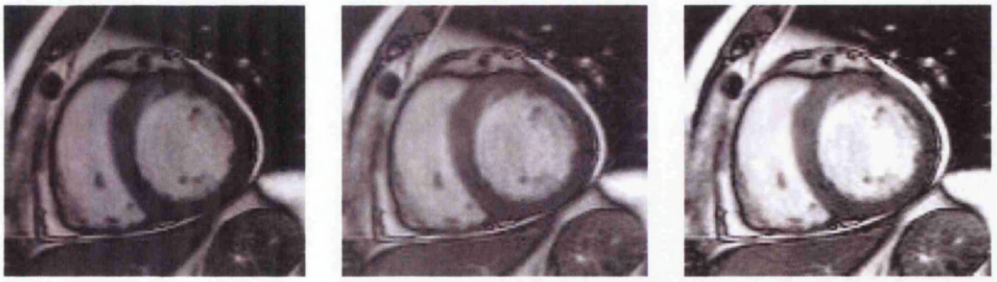

I_a | $I_b=I_a+40$ MSE = 0.28 | $I_c = I_a * 1.8$ MSE = 0.50

Figure 4.6 The image I_a is an 8-bit-per-pixel image. The image I_b is manipulated from image I_a by increasing the intensity of each pixel, $I_a(x,y)$ by a value of 40. Similar to I_b, each pixel in I_c equals to its corresponding pixel in I_a times 1.8. The MSE between the I_b and I_a, I_c and I_a vary significantly, showing that MSE is not tolerant to the linear change in pixel intensity.

4.4.2 Cross-correlation

Given a pair of variables x and y, the correlation between x and y is defined by:

$$C = \frac{\sum (x-\bar{x})(y-\bar{y})}{\sqrt{\sum (x-\bar{x})^2}\sqrt{\sum (y-\bar{y})^2}}$$

where $\bar{x}$ and $\bar{y}$ are the means of variables x and y. The value of C lies between 1 and -1. If the value of C is 1, the variables x and y are in "complete positive correlation". If C is -1, x and y are in "complete negative correlation". A value of C near zero indicates x and y are uncorrelated. Figure 4.7 shows examples of positive correlation, negative correlation and non-correlation.

For two 2D images I (x, y) and $I`$(x, y), x = 1, 2, …, M and y = 1, 2, …, N, their cross-correlation, $C(i \in x, j \in y)$ is calculated by:

$$C(i,j) = \frac{\sum_i \sum_j [I(i,j) - \bar{I}][I`(i,j) - \bar{I`}]}{\sqrt{\sum_i \sum_j [I(i,j) - \bar{I}]^2} \sqrt{\sum_i \sum_j [I`(i,j) - \bar{I`}]^2}}$$

where $\bar{I}$ and $\bar{I`}$ are the means of $I$(x, y) and $I`$(x, y).

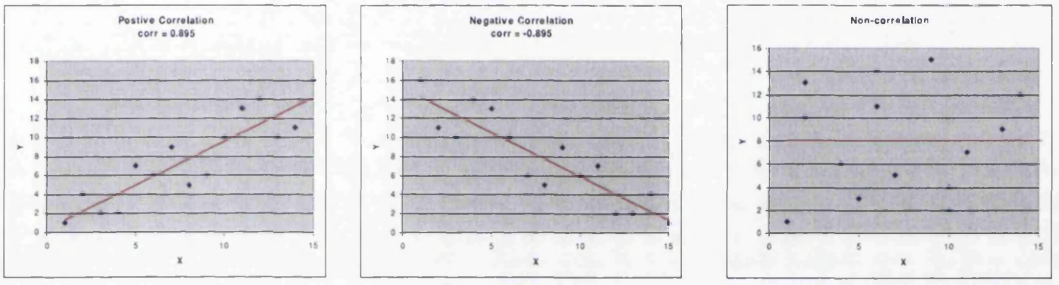

(a) (b) (c)

Figure 4.7 (a). positive correlation; (b). negative correlation; (c). non-correlation.

The correlation is a linear similarity measurement. The value of C measures only the strength of the linear relationship. It is not sensitive to the linear variety between the two images. The cross-correlation tests show the images used in the MSE discussion (figure 4.6) are no different (r_{11} = 1.0, r_{12} = 1.0 and r_{13} = 1.0).

The linear property makes cross-correlation immune to any linear change in pixel intensity. Given a set of images with different degrees of amplitude, although the brightness changes significantly, their correlation remains the same. But in the end, cross-correlation is a pixel intensity based measurement. Non-linear change of pixel intensity

(for example, random noise) will significantly affect the correlation results. In situations such as multiple modalities image registration, where the pixels intensities between the two input images are often varied, cross-correlation will be invalidated. To register images produced by different imaging modalities, feature-based similarity measurement criterion, such as mutual information is introduced (Pluim et al., 2003).

But also, the results could be meaningless, if the two variables x and y are correlated in a non-linear relationship. Also, the result of correlation could easily be affected by random noises. All the three examples shown in figure 4.8 have correlation of 0.90. The data shown in figure 4.8a distribute normally by the side of a line. Their correlation explains the situation relatively accurately. Figure 4.8b show a strong curvilinear relationship which cannot be explained by the linear correlation. Figure 4.8c illustrates of effect of noise. Most of the data points locate perfectly along a straight line. But the strong linear relationship is broken by an error datum (noise).

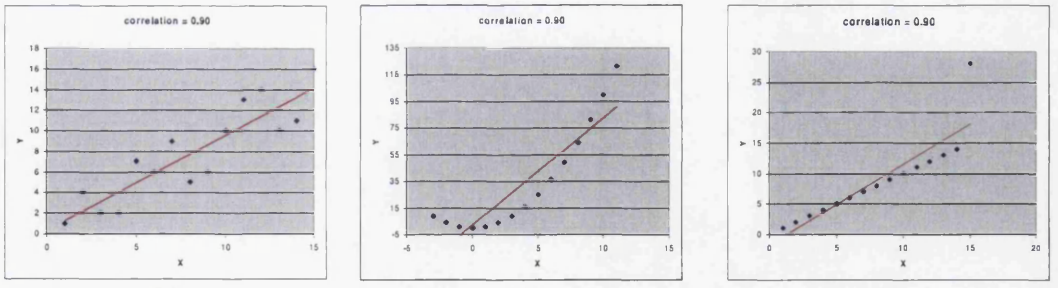

(a) (b) (c)

Figure 4.8 Three sets of data for which correlation = 0.90.

4.4.3 Mutual Information

Mutual information is a useful concept to measure the amount of information shared between two vectors. Given two vectors X and Y, mutual information is defined to:

$$MI(X,Y) = H(X) + H(Y) - H(X,Y) \qquad 4.7$$

in Claude E. Shannon's famous information theory (Shannon, 1948). In equation 4.7, $H(X)$ is the entropy of the vector X and $H(X, Y)$ is the joint entropy of vectors X and Y.

In physics, the word entropy implies the amount of "disorder" of a system. Mathematically, the entropy of the vector x is defined as:

$$H(X) = -\sum_{x} p(x) \log p(x) \qquad 4.8$$

where $p(x)$ is the probability of a element x in the vector X. The joint entropy of vectors X and Y is then defined by:

$$H(X,Y) = -\sum_{x,y} p(x, y) \log p(x, y)$$

$p(x,y)$ is the joint probability of $x \in X$ and $y \in Y$ in the vector $Z = X \cup Y$.

In recent years, mutual information was widely used in the image registration as a similarity measurement criterion. The two parameters, vector X and Y can be replaced by two images I and I' when mutual information is applied as an image analysis method. For an 8-bit grey scale image, each pixel in the image has 256 possible intensities (0 ~ 255). For each possible intensity $x \in (0, 255)$, its probability $p(x)$ in a given image I can be calculated from the histogram of the image I. The entropy of the image I, $H(I)$ can therefore be calculated based on equation (4.8). Similarly, the joint entropy of the image I and I' are computed from their joint histogram. Figure 4.9 shows the construction of the joint histogram from two images.

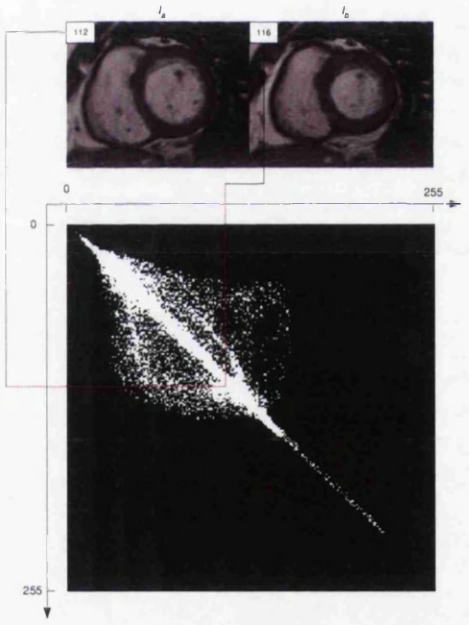

Figure 4.9 The generation of the joint histogram between two images

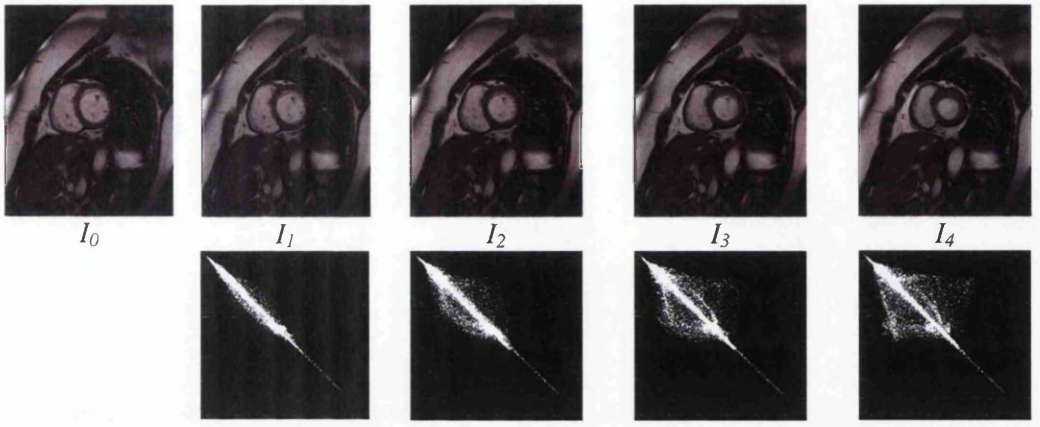

Figure 4.10 The first row shows a cardiac cine MRI sequence during systole. The images in the second row are the joint histograms between I_0 and $I_{n=1...4}$. The joint histogram disperses with each increment of misregistration during a cardiac cycle.

In Shannon's definition, mutual information is associated with the entropies of the two input images, $H(X)$ and $H(Y)$ and their joint entropy $H(X,Y)$ (equation 4.7). Entropy describes the physical property of a given image. Neither $H(X)$ nor $H(Y)$ presents the share information Therefore, the mutual information is in inverse proportion to the joint entropy $H(X,Y)$. When the joint entropy is minimal, the mutual information reaches its peak. By contrast, the mutual information is minimal if the joint entropy is maximal. As an image processing method, small joint entropy means a sharp definition in the joint histogram. For example, figure 4.10 shows a sequence of cardiac MRI images within a cardiac cycle. From the diastole to the systole, the images in the sequence are referred to as I_0 to I_4. The joint histogram between the first two images I_0 and I_1 has the sharpest definition along the diagonal due to the good similarity. As the myocardium moves toward the systolic phase, the joint histogram disperses because the degree of misregistration increases.

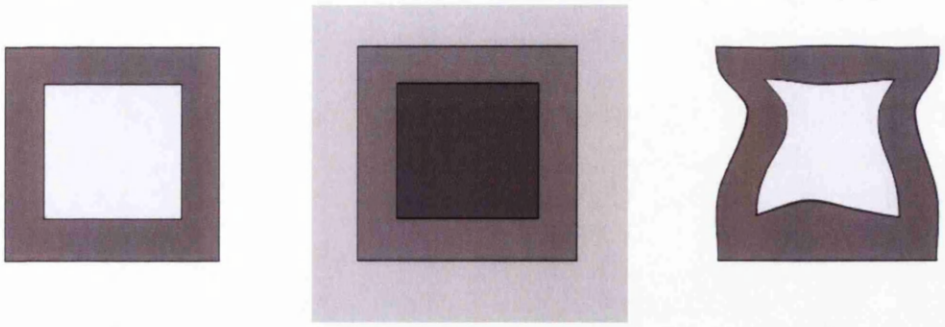

I_a I_b I_c

Figure 4.11 The three images we used to compare the properties of cross-correlation and mutual information as a similarity measurement technique.

Mutual information is a robust similarity measurement tool. It is especially useful for medical image registration because it is immune from the pixel intensity differences between two images.

Figure 4.11 shows three manipulated images. From left to right, the first two images share the same shape but with different pixel intensity. The third image is the deformation of the first image. Therefore, they have the same pixel intensities but a different shape. For simplicity, we call the three images, I_a, I_b and I_c. Table 4.1 summarized the mutual information and cross-correlation between the three images.

	I_a		I_b		I_c	
	MI[2]	r[3]	MI	r	MI	r
I_a	1.55	1	1.55	0.59	1.14	0.80

Table 4.1 Comparison between mutual information and cross- correlation.

[2] **MI = Mutual Information**
[3] **r = Cross-correlation**

The mutual information between I_a and itself, $MI(I_a, I_a)$ is 1.55, which is the maximum possible value. Although the pixel intensity of I_b is significantly different with I_a (cross correlation r = 0.59), their mutual information $MI(I_a, I_b)$ remains at the maximum, because the shape of I_b is identical to I_a. Compared to I_a, I_c has similar pixel intensities but a different shape. Both the mutual information and the cross-correlation between the two images decrease. This experiment practically proves mutual information's immunity to pixel intensity variation while cross-correlation is sensitive to both the shape and pixel intensity.

4.4.4 Complexity analysis

Thus far, we have introduced the properties of the MSE, cross correlation and MI. In this section, we will discuss the computational complexities of the three similarity measurement method.

Operator	MSE	CC	MI
+	L	5L	6L + 1
-	2L	6L	1
×	L + 1	3L + 2	3L + 3
÷	1	3	3L
$\sqrt{}$	0	2	0
Log	0	0	3L

Table 4.2 Number of mathematic operations involves in the similarity measurement.
L is the number of pixels in an image

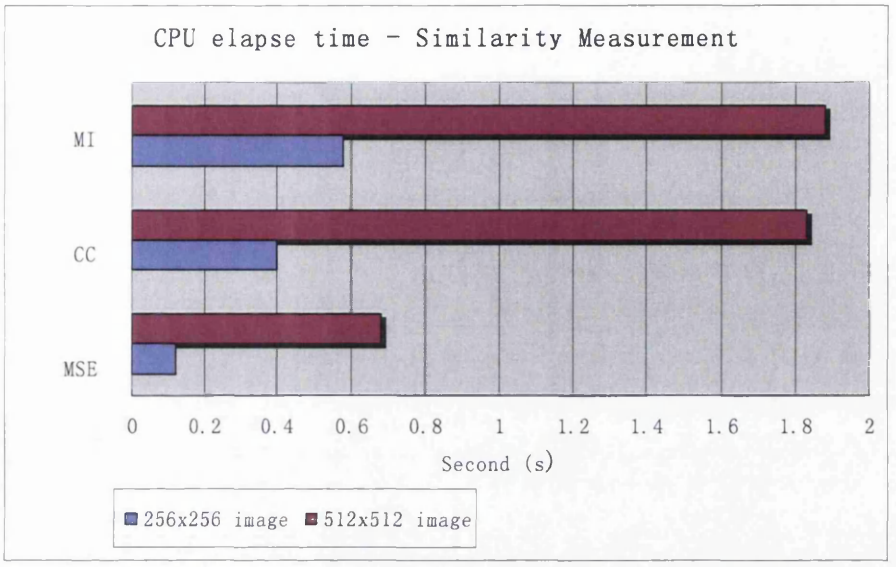

Figure 4.12 MSE has the least computational intensity. Its CPU elapsed time is significantly shorter than CC and MI.

At present, using a mainstream personal computer (Intel P4-1.7GHz, 512MB RAM), the similarity measurement in terms of MSE, CC and MI between two 256x256 images could be all less than 100ms. However, in image registration, the similarity measurement between two images is often repeated to determine the best match, which could be rather time-consuming. MSE is a pixel-based similarity measurement, which has the lowest complexity compared to the other two measurements, CC and MI. Table 4.2 summarised the number of the operations involved in the similarity measurement using MSE, CC and MI.

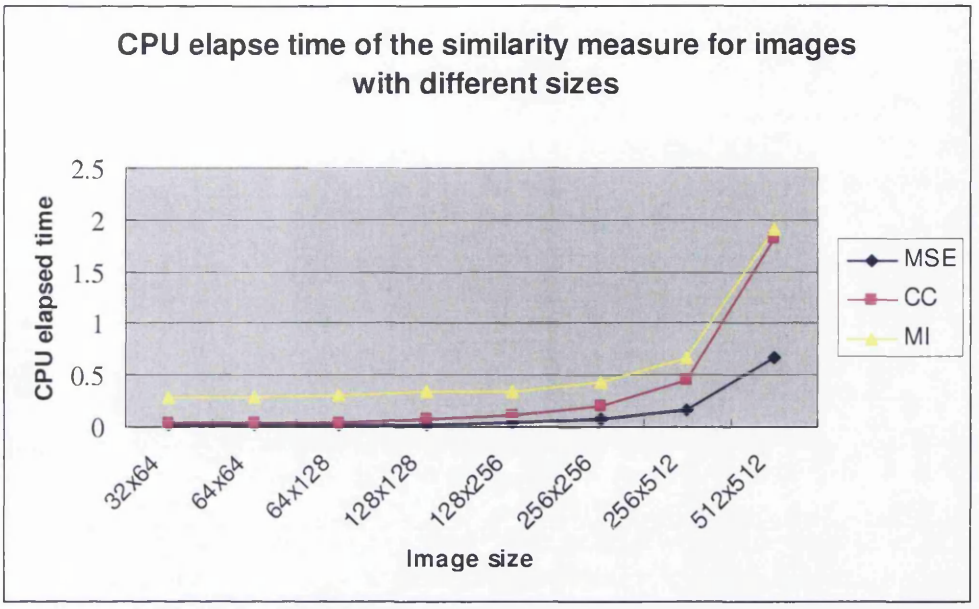

Figure 4.13 The CPU elapsed time for the similarity measurement increases as the image size increases.

The calculation of MI appears to have the greatest number of operations and presumably the highest computational complexity. Practically, we measured two pairs of images with different sizes using MSE, CC and MI. For each measurement, the similarity criteria are computed iteratively for 100 times to get the CPU elapsed time. The experiment was carried out using a personal computer equipped with an Intel 1.7GHz processor and 512 RAM. The data are shown in figure 4.12. The CPU elapsed time increases as the size of the images increase. However, the increment is not linear. Figure 4.13 shows the relationship between the image size and the CPU elapse time. In many image registration algorithms, the images are partitioned into overlapping or non-overlapping blocks. The similarity measurement matches the blocks instead of the entire image to seek the local maxima which reduces the computational intensity.

4.5 Searching strategy

Given two images I_a and I_b, the objective of image registration is to decide a transformation function T which will match image I_a to image I_b following a defined criterion such as cross-correlation. Either global or local transformations are allowed in searching for the best match. The global transformation is the transformation in which a single mathematical expression applies to an entire image. The global image registrations traverse every possible transformation iteratively to maximize some similarity criterions. The similarity measurement is not necessary to apply to the entire image. Alternatively, several control points can be defined either manually or automatically on both the two input images. By using matched the control points and their neighbouring pixels, the global transformation function can be derived with a significantly lower computational complexity (Ardeshir, 1986; Ardeshir, 1988). The application of the global image transformation is limited in medical imaging. It is often employed to compensate the motion artefacts caused by inevitable patient motion such as respiration motion (Raghavendra et al., 2004; Rohlfing et al., 2003). To register more elastic tissue motion such as cardiac motion, local image registration algorithms with free form deformation (Rueckert et al., 1999; McLeish et al., 2002; Raghavendra et al., 04; Rao et al., 2004) and optical flow are often required (Dougherty et al., 1999). The local method is more complex. Besides the similarity measurement, the constraints between local areas such as the volume preserve (incompressibility) constraint (Rohlfing et al., 2003) and curvature regularization (Agostino et al., 2003) also need to be carefully considered. However, local registrations have the greatest number of degrees of freedom. Consequently, its

computational burden is significantly higher than the global method. The efficiency was the major barrier preventing local image registration technique from being used practically. In the past decades, many efficient searching strategies have been proposed. Studholme et al. use gradient descent (Studholme et al., 1995), Cideciyan et al. use the simplex method (Cideciyan et al., 1992), Pelizzari et al.(Pelizzari et al., 1989) and Collignon et al. (Collignon et al., 1995) use Powell's minimization. Many methods also incorporate a multiple-resolution structure to further increase the registration speed (Studholme et al., 1995; Thevenaz et al., 1998; Makela et al., 2002; Periaswamy et al., 2003).

The multiple resolution structure is often referred to as the image pyramid in image processing. The image pyramid is first reported by Adelson and his colleagues (Adelson et al., 1984). An image pyramid is a collection of images of reduced resolutions of the original image. Given an image I, each layer of the pyramid I_l is built by low pass filtering its previous layer after which is subsampled by a factor of n horizontally and vertically (4.14). The pyramid layer I_l contains low spatial frequency information present in the pyramid layer I_{l-1} but has only $\frac{1}{n^2}$ the number of pixels. Such an image pyramid is referred to as Gaussian pyramid.

Since its invention, image pyramid has found many applications, including loss/lossless image coding (Cockshott et al., 2003; Cockshott and Tao, 2003), image segmentation, image registration, etc. The implementation of the image pyramid is straightforward and

more importantly, it can be adopted in any existing searching model. For such reasons, many practically working image registration algorithms involved the application of image pyramid.

Figure 4.14 Construction of a Gaussian image pyramid. The images were downsampled by a factor of 2 horizontally and vertically.

The pyramidal image registrations always start from the layer with the lowest resolution (top of the pyramid). Since the initial estimations from the low resolution layers are quick, full searching is therefore possible producing the best results. In moving successively to the layers which have the greater details and the higher resolution, the initial estimations are used to cut the searching areas into local regions. This efficiently reduces the searching time, making it easier to eventually find the global maxima in the bottom layer (original image). In this work, we employed an efficient and robust image registration based on the difference image pyramid to extract the cardiac wall motion.

Chapter 5
Measurement validation

The objective of this work is to develop an algorithmic method to assess cardiac viability. A versatile software package, Cardiowarp (GCMRU, UK) was developed to implement the data validation. The functions of CardioWarp include the measurement of left ventricle volume, left ventricle mass, ejection fraction, etc. The measurement is based on the manual definition of cardiac contours, including epicardium and endocardium. Before starting the analysis, a validation of the software package is essential. The validation involves two procedures:

1. Validate data against a designed phantom;
2. Validate data against a widely used and approved for medical use commercial software package, Argus (Siemens, Erlangen, Germany).

5.1 Validate the measurement against designed phantom

5.1.1 The phantom

To validate the accuracy of the software package we developed, a simple cone-shape phantom was built by the mechanical workshop of the Western Infirmary, Glasgow. The phantom contains two components, a lip and a base. There is a gap between the lip and the base, in which MRI visible material such as water can be sealed. The design and parameters of the phantom are shown in figure 5.1.

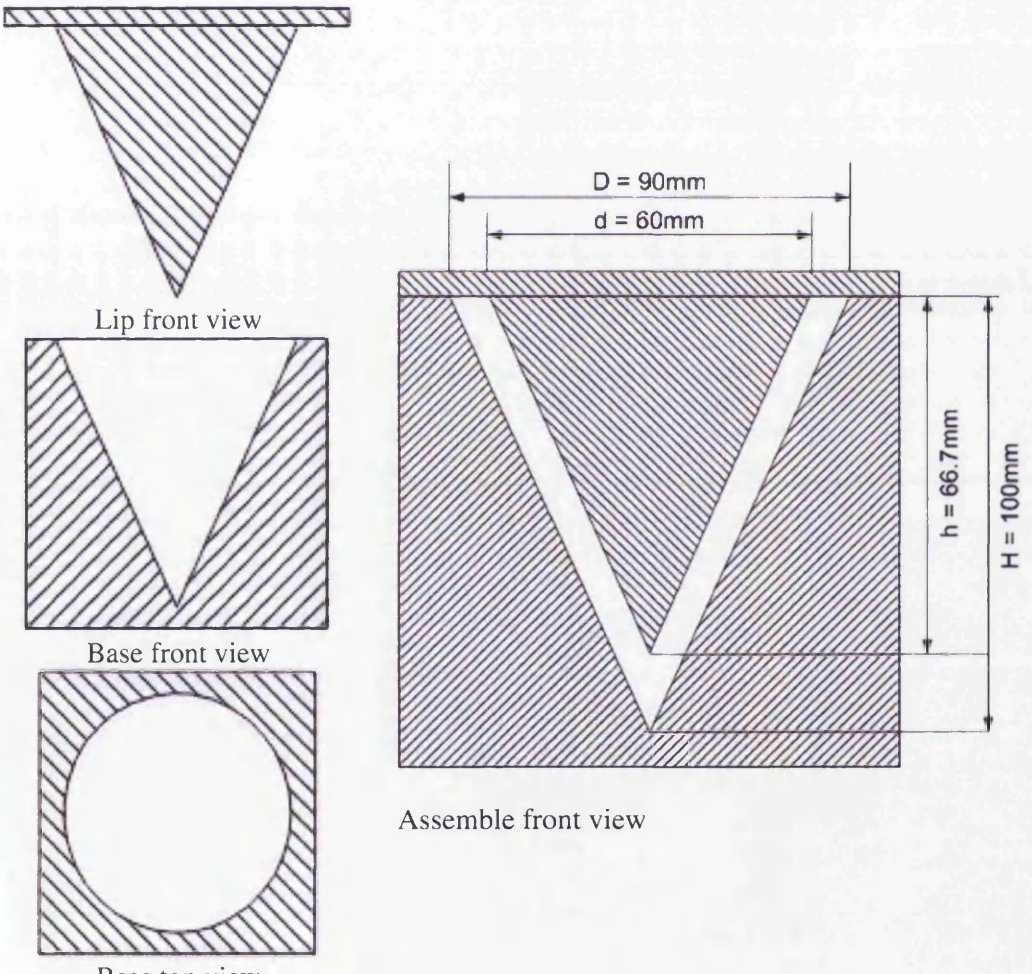

Figure 5.1 The cone-shape phantom designed to validate the accuracy the measurement.

Figure 5.2 shows the pictures of the phantom. The phantom was filled with pure water during the MRI acquisition.

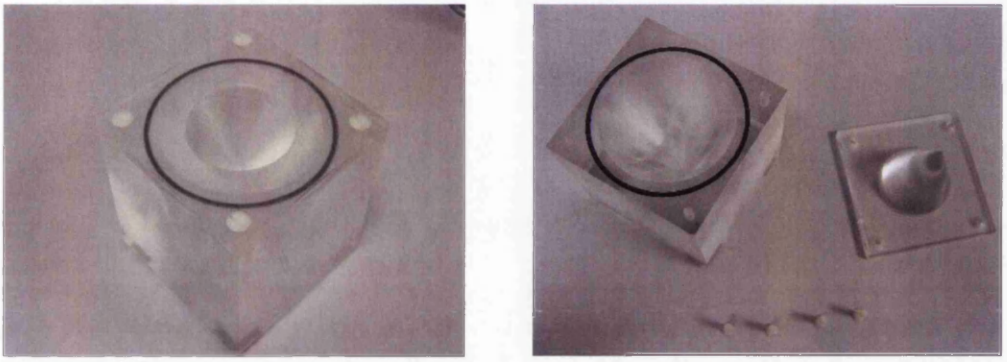

Figure 5.2 The cone-shape phantom.

MRI was performed on a Siemens Sonata 1.5T system. The pulse sequence TrueFISP, which was used to acquire cardiac CINE MR images, was utilised to acquire images of the phantom. Image resolution was 208 x 256 pixels Pixel dimensions were 1.33 x 1.33mm. TR/TE = 47.1 / 1.57. Flip angle = 60°. Slice thickness = 4mm plus 1mm gap. The images are shown in figure 5.3.

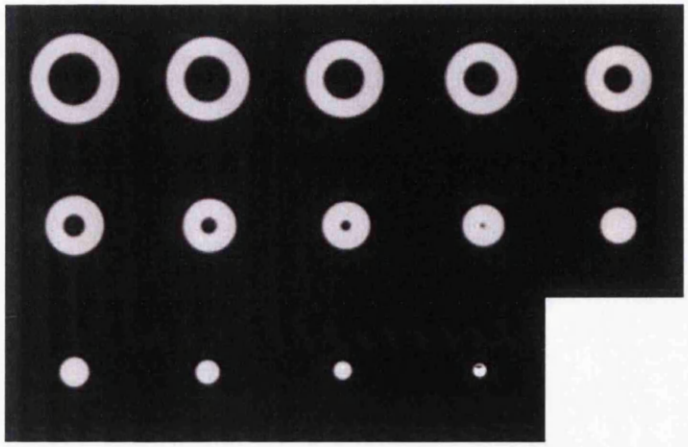

Figure 5.3. MRI images of the cone-shape phantom. Pixel resolution = 1.33 x 1.33mm. TR/TE = 47.1 / 1.57. Flip angle = 60°. Slice thickness = 4mm plus 1mm gap

The phantom is made of perspex® which is invisible in MRI image (dark area). The water inside the phantom shows up as a bright ring. We consider the outer and inner contours of the ring as the outer and inner surface of the myocardium.

5.1.2 Calculation of the phantom volume

With the given parameters (figure 5.1), the volumes of the parts of the phantom, including the cone on the lip and the cone in the base can be calculated simply as follows.

$$Volume_{cone,base} = \frac{\pi D^2 \times H}{3} = \frac{3.14 \times 45^2 \times 100}{3} = 211.95ml$$

$$\frac{D}{H} = \frac{d}{h} \Rightarrow h = \frac{d \times H}{D} = \frac{30 \times 100}{45} = 66.7mm$$

$$Volume_{cone,lip} = \frac{\pi d^2 \times h}{3} = \frac{3.14 \times 30^2 \times 66.7}{3} = 62.83ml$$

**D, H, d and h are labelled in figure 5.1.*

But in practice, 2D MR images were acquired from different slice location to cover the entire myocardium (figure 5.3). The slice thickness and gap between slices were defined manually before the data acquisition. Generally, the volume is estimated from the slices using a modified Simpson's rule as shown in equation 3.1 and 3.2.

To compare the phantom volume with software such as Argus and Cardiowarp, we should therefore recalculate the phantom volume using the same method. Figure 5.4 illustrates the recalculation of the cone on the lip. After the recalculation, the volume changed from 62.8ml to 68.5ml.

In this test, the inner contour of the ring is manually defined for every image. The volume is estimated using Cardiowarp and Argus. The estimation using Cardiowarp is compared with the calculated volume and the estimation using Argus. In addition, the measurement of Argus was compared with the phantom to estimate the subjective errors.

Table 5.1 summarises the experimental results. The measurement error for each stack is shown in figure 5.5. To highlight the subjective errors, the measurement error of Argus is shown in figure 5.5. The measurement of volume by Cardiowarp was found to be systematically larger than the phantom. But the same form of errors can be observed between the comparison of Argus and the phantom. Therefore, we presumed the errors are subjective and may be caused by the manual contour definition. Analysis by student t-test showed that there was no significant difference between the measurement using CardioWarp, Argus (p = 0.47) and the calculation volume (p = 0.47).

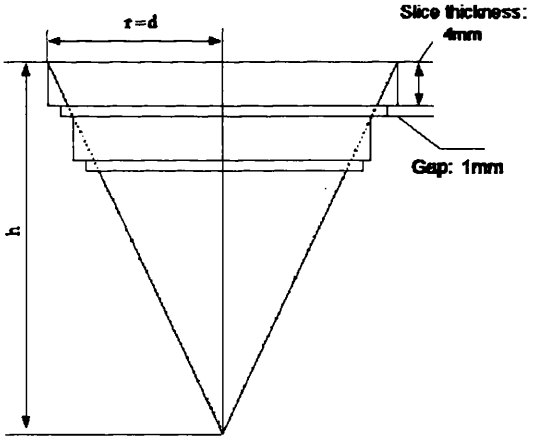

$$V_i = A_i t + \frac{g(A_i + A_{i+1})}{2}$$

$$V_i = 4\pi r_i^2 + \frac{\pi r_i^2 + \pi r_{i+1}^2}{2}$$

where

$$\frac{r_i}{h-(4+1)i} = \frac{r_{i+1}}{h-(4+1)(i+1)} \rightarrow r_{i+1} = \frac{r_i(h-(4+1)(i+1))}{h-5i}$$

$$V = \sum_i V_i$$

The volumes of the phantom are:

$$Volume_{cone,lip} = 68.5ml$$

Figure 5.4 Modified volume calculation of the phantom. After recalculation, the volume increases because the cone is considered as stacks of column.

Slice ID	Phantom (ml)	Argus (ml)	Cardiowarp (ml)	Difference (cardiowarp-phantom) (ml)	Difference (cardiowarp-Argus) (ml)
1	13.9	13.6	12.9	-1.0	-0.67
2	11.9	12.3	12.0	0.1	-0.27
3	10.0	10.5	10.6	0.6	0.09
4	8.3	8.8	8.8	0.4	0.00
5	6.8	7.2	7.0	0.2	-0.24
6	5.4	5.8	5.8	0.4	-0.09
7	4.2	4.6	4.5	0.4	-0.03
8	3.1	3.5	3.3	0.2	-0.14
9	2.2	2.5	2.5	0.3	-0.06
10	1.4	1.7	1.6	0.2	-0.05
11	0.8	1.1	0.9	0.1	-0.17
12	0.4	0.5	0.5	0.1	0.02
Mean (±SD)				0.2 ± 0.4	-0.1 ± 0.2

Table 5.1 Comparison between the slice stacks measured using Cardiowarp, Argus and the phantom.

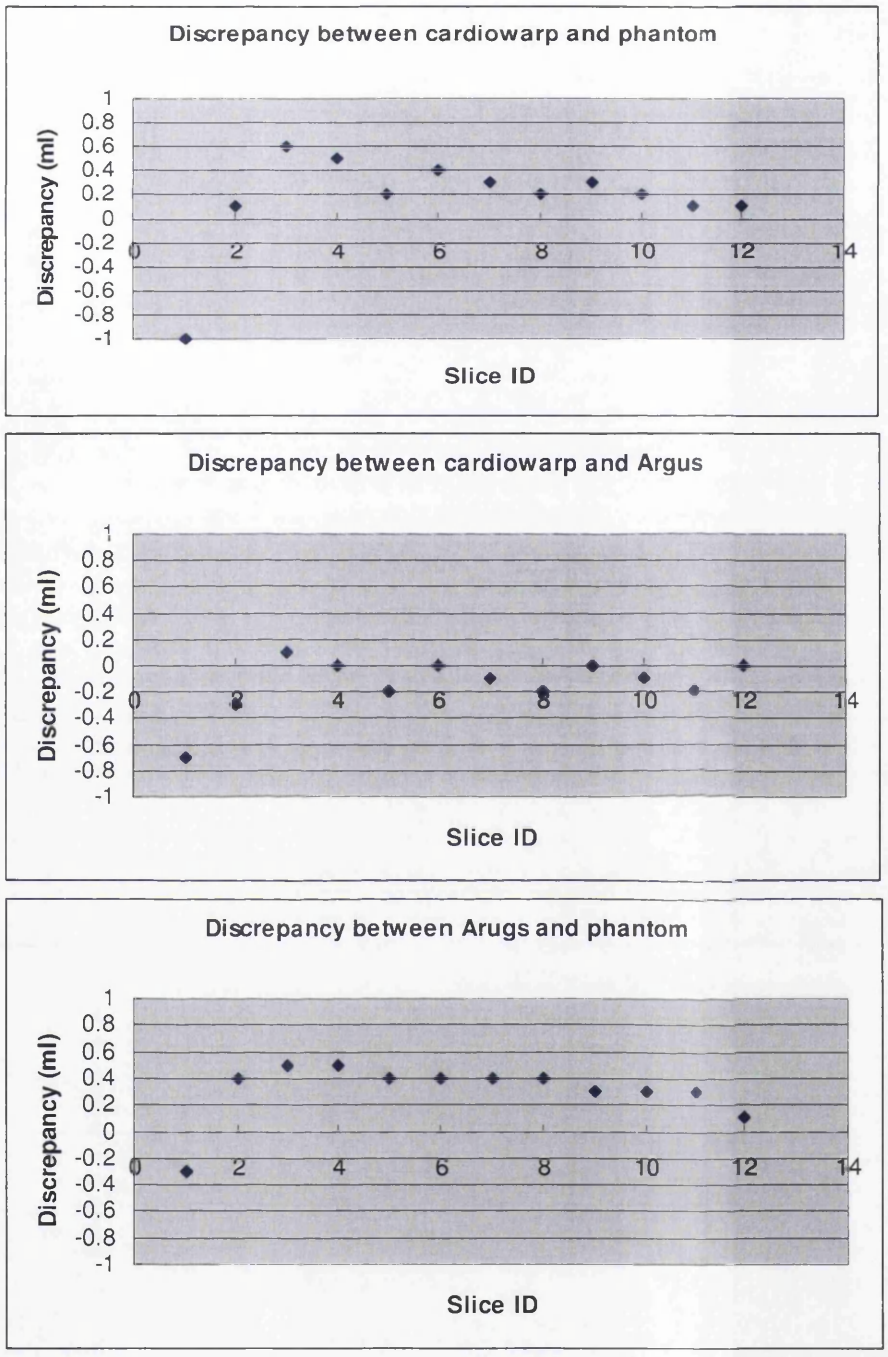

Figure 5.5 The measurement error of Cardiowarp for each stack compared to the phantom and Argus. To estimate the subjective errors, the Argus was also validated against the phantom.

5.2 Validate the measurement against commercial software package

8 consecutive scans were selected from the database of the Glasgow Cardiac MRI Unit. The left ventricle end diastolic volume is measured manually using both Cardiowarp and Argus. To avoid unnecessary subjective errors, the measurement using Cardiowarp is implemented immediately after the measurement using Argus. Table (5.2) compares the experimental results as well as the mean volumes and student t-test. The experimental results show no significant difference between the measurement using Argus and Cardiowarp.

ID	Argus (ml)	Cardiowarp (ml)	Difference (%)
1	153.25	147.35	4
2	185.06	180.95	2
3	136.28	130.60	4
4	72.84	76.49	5
5	226.03	229.65	2
6	81.7	80.88	1
7	118.92	120.50	1
8	191.91	190.54	1
Mean	145.47	145.43	2.5 ± 1.5
Student t-test	0.47		

Table 5.2. Comparison between Argus and Cardiowarp by measuring the left ventricle endocardium volumes of 8 sequential patients.

5.3 Conclusion

A versatile cardiac MRI software package, Cardiowarp was developed in this work. It was essential to ensure that Cardiowarp was validated before any further measurements were made. Cardiowarp was validated against a specially designed phantom and a commercial software package, Argus (Siemens, Erlargen, Germany). The experimental results showed no significant difference between the measurement of Cardiowarp (70.4ml) and the phantom (68.5ml, $p = 0.47$) and the measurement of Argus (72.0ml, $p = 0.47$). In addition, 8 sequential patients were selected from the database of GCMRU. The left ventricle volumes were measured using both Argus and Cardiowarp, mean(Argus) / mean (Cardiowarp) = 145.75 / 145.37, average error = 2.5% ± 1.5%, student t-test $p = 0.49 > 0.05$.

Practically, the results proved that Cardiowarp was accurate and reliable for clinical use. Therefore, it was ready for the forthcoming studies.

Chapter 6
A Motion Study of Late Contrast-Enhanced MR Images

6.1 Cardiac Viability Assessment Using MRI

The steady state free precession (SSFP) technique is a fast MRI acquisition technique which exploits the ratio of T2 / T1 to produce high quality MRI images (Gyngell, 1988). SSFP has been widely used by commercial MRI scanners, for example, in Siemens it is know as True FISP. Using SSFP, it is possible to capture multiple MRI images in a cardiac cycle, building cardiac cine MRI images.

A typical cine cardiac MRI sequence contains 10 to 50 images depending on the heart rate. cine MRI images reveal the anatomical structure of the myocardium as well as the cardiac wall motion. There are three common reasons for the reduced myocardial wall motion: the hibernating myocardium (Braunwald & Rutherford, 1986; Conversano et al., 1999), the stunned myocardium (Conversano et al., 1999) and myocardial infarction (Ball, 1995). The hibernating myocardium and the stunned myocardium must be differentiated by myocardial infarction because they are both viable and potentially reversible after revascularisation. Clinically, the hibernating

myocardium and the stunned myocardium have different causes. Hibernating myocardium, which can be defined as wall motion abnormality is related to the myocardial blood flow (MBF). The wall motion reduces as the MBF reduces. Acute ischaemia (e.g. major coronary occlusion) can lead to stunned myocardium, which persists for a variable period of time, up to two weeks, even after ischaemia has been relieved. In this work, we attempt to locate the myocardium which moves abnormally but is not acute myocardial infarction. The myocardium with abnormal wall motion could be either the hibernating myocardium or the stunned myocardium. For simplicity, we use the "hibernating myocardium" to represent the hibernating myocardium and the stunned myocardium in this study.

In patients with acute myocardial infarction, late contrast enhancement can be observed from 10 minutes after gadolinium-diethylenetriamine pentaacetic acid (Gd-DTPA) injection. The paramagnetic Gd-DTPA blocked by the myocardial infarction changes the local magnetic field and shortens the T1, whereas for the normal myocardium, the inversion time used nulls the signal from the tissue since its T1 changes in a relatively smaller degree compared to the myocardial infarction. This technique is called late contrast enhanced MRI (see chapter 3). Late contrast-enhanced MRI presents precise information about the myocardial infarction, including the location, the shape and the size of the myocardial infarction (Ibrahim et al., 2003).

The acquisition of late contrast enhanced MRI requires a relatively long inversion time before data collection to ensure the best contrast by completely nulling the signal from healthy myocardium. It takes longer to produce an image compared to the other techniques such as SSFP, which has no such nulling involved. At present, only static late contrast enhanced MRI can be produced.

The study of late contrast-enhanced MRI images, in combination with cardiac wall motion from the cine MRI sequence, allows a cardiac viability score to be derived.

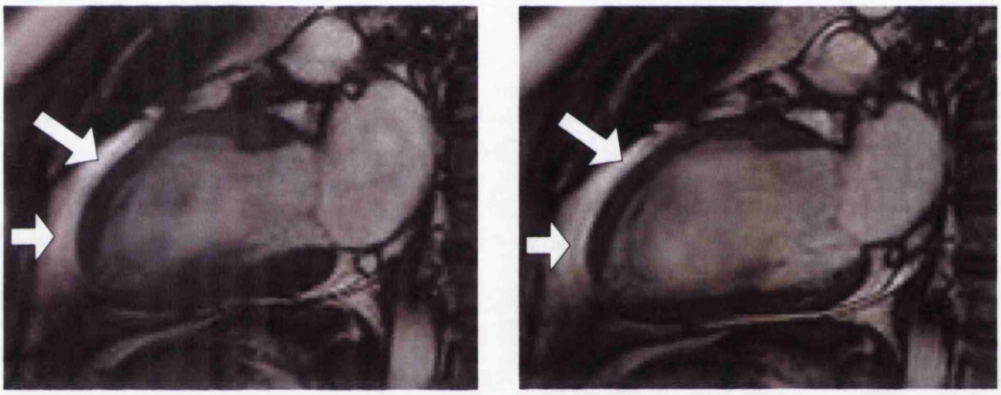

(a) (b)

Figure 6.1 Reduced cardiac wall motion suggests the dysfunction of myocardium. (a). Systole; (b). Diastole. The arrows indicate the areas which have reduced cardiac wall motion.

By using a cardiac viability score, clinicians seek to locate the hibernating myocardium.

At present, late contrast enhanced MRI and cine MRI are acquired separately, and then compared with each other to facilitate assessment. However, in situations where

patient motion and respiratory motion are present, such an approach may introduce diagnostic error. To address this issue, research is underway to produce a cine MRI with late contrast enhancement.

6.2 Post Gd-DTPA cine MR images

The injected contrast agent, Gd-DTPA, will pass through the cardiac wall via the microcirculation system. However, it cannot pass through the myocardial infarction easily since the microcirculation system is not functional. The local magnetic field around the myocardial infarction is changed because of the high concentration of the Gd-DTPA. Therefore since the T1 change is proportional to the change in local magnetic field, the area of myocardial infarction appears as having different pixel intensity in T1 weighted MRI

After the injection of the Gd-DTPA, some contrast enhancement can be observed in the T1 weighted cine MRI sequence. An example of such motion late contrast enhanced MRI sequence is shown in figure 6.2.

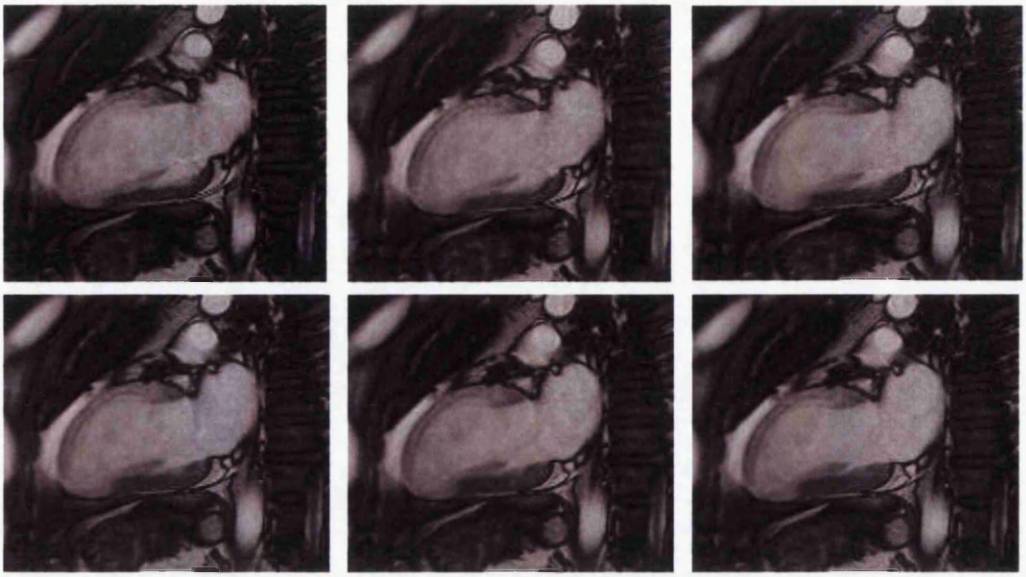

Figure 6.2 A sequence of post Gd-DTPA MR images from the long axis view.

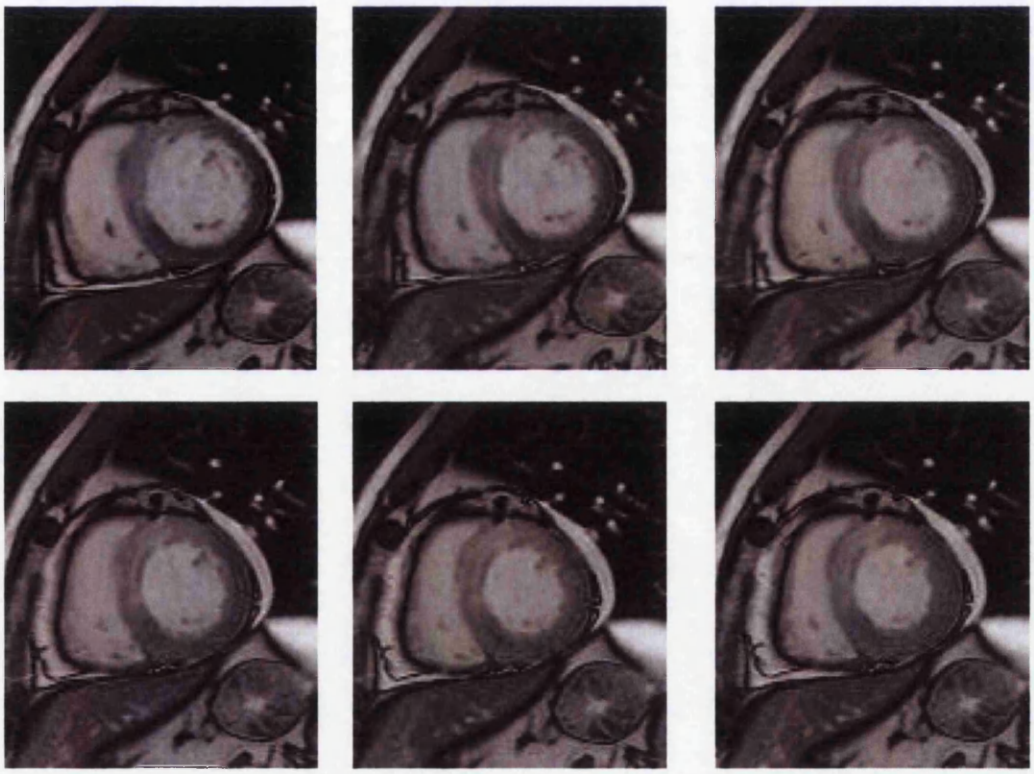

Figure 6.3 A sequence of post Gd-DTPA cine MR images from the short-axis view.

Figure 6.3 shows the motion late contrast enhanced MRI images from the short axis view.

The direct acquisition of a contrast enhanced image using an ultrafast pulse sequence such as TrueFISP was first reported and evaluated by Q. Chen and his colleagues in 2003 (Chen et al., 2003). The major advantage of this method is its simplicity. It can be performed using a conventional MRI scanner with widely used cardiac MRI pulse sequence. However, without the time-consuming preparation pulse, the contrast enhancement is not always easily visible. In some situations, the contrast enhancement is too weak to provide clinically useful information (figure 6.3). In this study, we set out to develop an image registration based software solution to integrate the contrastenhanced image into the cine MR images using image registration, in order to build a cine late-contrast enhanced MRI sequence. The proposed method is novel, efficient and accurate.

Additionally this method enables the assessment of existing contrast enhanced images since it is a post-processing technique.

6.3 A software solution

The proposed software solution to build motion late contrast enhanced MRI images

involves the following two major steps:

1. Extracting the motion fields of the myocardium from cardiac cine MR images.
2. Generating cine late contrast enhancement images using the motion field.

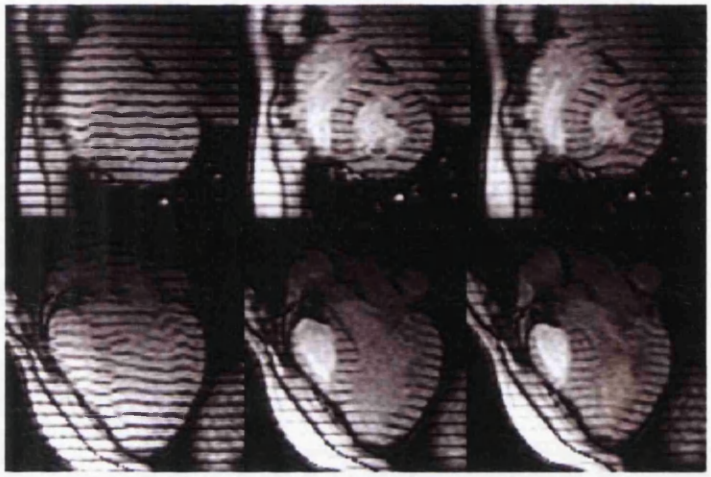

Figure 6.4 Tagged cardiac MR images. The deformation of the magnetic strips indicates the cardiac motion.[1]

Cardiac wall motion is not rigid. Within the 2D acquisition plane, multiple forms of motion, including contraction, translation, rotation and other forms of complex motion, can be observed. The quantitative study of cardiac motion using MRI has attracted many investigations in recent years. Tagged MRI appears as a robust tool that provides detailed quantitative assessment of myocardial deformation (Kraitchman et al., 1995; Park et al., 1996; Doughty et al, 1999; Eusemann et al., 2001; Garot, 2004). Cardiac tagged MRI applies a magnetisation grid to the selected imaging plane (figure 6.4) at the beginning of the cardiac cycle that persists during systole. The deformation of the dark strips reflects the myocardial wall motion as it moves with the

[1] Source: http://www.mri.jhmi.edu/MedImgLab/papers/mcveigh94_1/paper.html

heart. However, even the quantitative study of the strip deformation is proved to be difficult. In recent years, many methods have been proposed, many of which used image registration (Doughty et al, 1999; Chandrashekara et al, 2002; Suinesiaputra et al., 2003). In this study, we attempt to simplify the problem by extracting cardiac deformation from cardiac cine MR images.

In our experiment, an image registration algorithm will be employed to extract the motion data directly from cardiac cine MR images. The chosen registration algorithm will meet the following requirements:

1. Non-rigid. The cardiac motion is non-rigid. A non-rigid image registration algorithm produces more realistic cardiac motion data compared to its rigid counterpart.
2. Accurate and robust. The image registration will be accurate and robust to produce clinically useful data.
3. Efficient. The efficiency of an algorithm is the measure of the amount of time for the algorithm to execute. To make this technique practically useful, the image registration algorithm must produce results efficiently.

In the following sections, we will present such an image registration algorithm and this technique in detail. Experimental results and discussion will also be presented. The last section of this chapter will form a conclusion for this technique.

6.4 Image registration

The background knowledge required for the image registration has been discussed in chapter 4. In this chapter, we will focus on the algorithms used to generate motion late contrast enhanced images.

Our experiments have utilised an image registration technique: multiple scales signal matcher (MSSM), which was originally designed to measure apparent motion between pairs of stereoscopic images. MSSM was developed in the Computing Science Department[2], Glasgow University[3]. It has been successfully used in three dimensional modelling (Siebert et al., 1994; Marshall et al., 2000).

6.5 Multiple scales signals matcher (MSSM)

The purpose of MSSM is to construct a disparity map from a pair of digitised images, I and $I`$. The disparity map is a two-dimensional matrix which specifies for each pixel $p(x,y)$ in $I$ the distance to a corresponding pixel $p`(x, y)$ in $I`$.

[2] http://www.dcs.gla.ac.uk
[3] http://www.gla.ac.uk

Cross-correlation (see chapter 4) was employed in MSSM as the similarity measurement. The calculation of the cross-correlation is computationally complex. To increase the matching speed, we built a scale differential image pyramid. The building of the scale differential image pyramid is discussed in the following section.

6.5.1 Forming of the scale differential image pyramid

The image pyramid was first reported by Adelson and his colleagues (Adelson et al., 1984). An image pyramid is a collection of images of reduced resolutions of the original image. The layers of the scale image pyramid are constructed by:

$$G_0 = I$$

$$G_{i+1} = Scale(G_i, f)$$

$$Pyr_i = Scale(G_{i+1}, f) - G_i$$

where I is the input image. $Scale(G, f)$ is a low-pass filter which scales the image G by a factor f in both the width and the height of the image. Figure 6.5 is the flow diagram which illustrates the construction of the differential image pyramid.

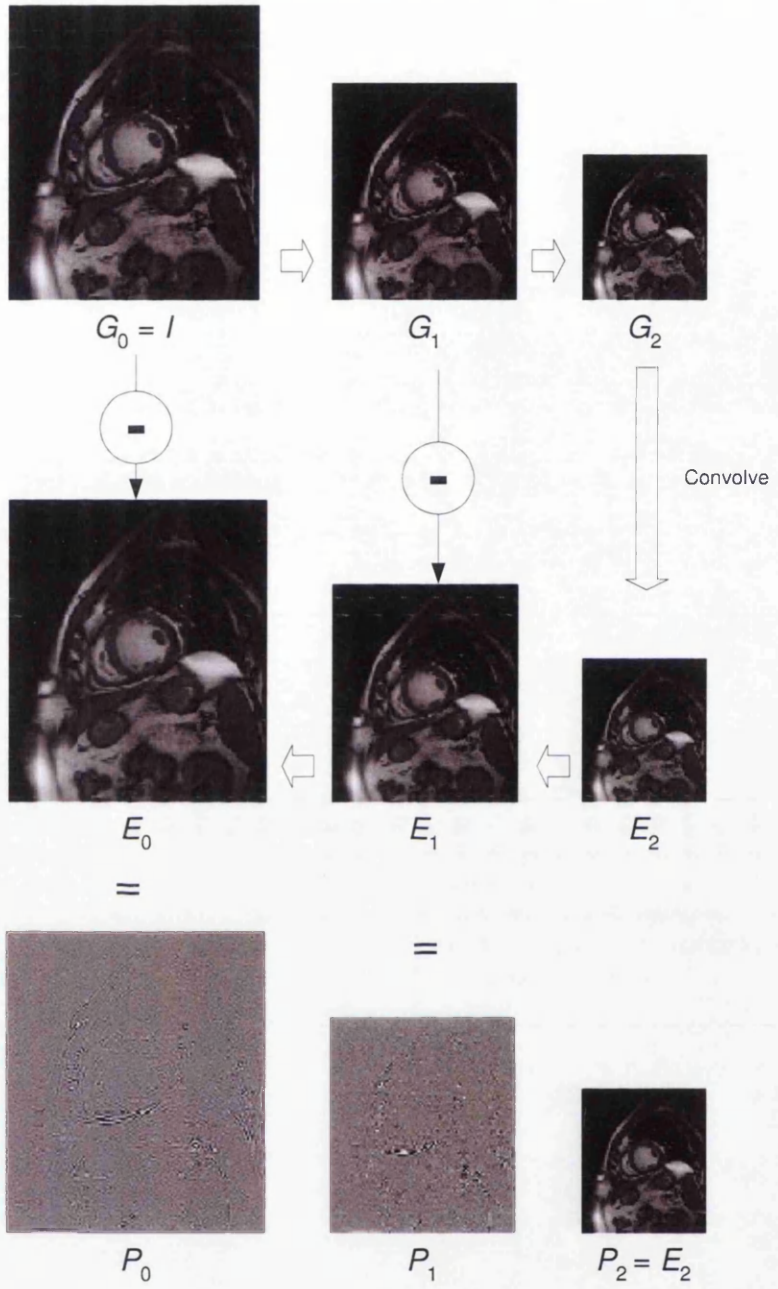

Figure 6.5 Construction of a 3-level differential image pyramid. The matching of MSSM is performed on the differential image pyramid. Image G_0 is the input image. It was downsampled to produce image G_1 and G_2. G_0, G_1 and G_2 were the three layers of the image pyramid, P_g. Image G_2 was low-pass filtered to produce image E_2. Image E_2 was scaled to match the size of G_1, producing image E_1. Using the same way, image E_0 was produced. E_0 together with E_1 and E_2 form the second image pyramid P_e. The differential pyramid P was constructed by subtracting each layer of the pyramid P_e from its corresponding layer in the pyramid P_g except the top-most layer. The top-most layer of the differential pyramid is identical to the top-most layer in the pyramid P_e, which is E_2 in this example.

The matching process is run on each successive scale of the pyramid starting with the top-most layer of the pyramid. In moving to successively greater layers of the pyramid, the initial estimates of the disparity map for each layer are provided from the results of matching the previous layer.

The differential image pyramid represents the original image in the frequency space. The benefits of matching in the frequency space are:

1. The matching will focus on the high frequency areas which normally present the contours and the shapes.
2. The matching will be less sensitive to the variation of pixel intensity, which could not be shown in the frequency space.

6.5.2 Matching and warping

For each layer, the matching outputs a disparity map, including three floating-point vector maps, $\boldsymbol{H}$, $\boldsymbol{V}$ *and* $\boldsymbol{C}$. $\boldsymbol{H}$ and $\boldsymbol{V}$ are the horizontal and vertical vector maps indicating the translation of each pixel from image I to image I'. $\boldsymbol{C}$ is called the confidence map which specifies the degree of confidence with which the disparity is

held.

For each pixel $p_1(i,j)$ *in image* I_1

1. *let* $C_{i,j}(\hat{i},\hat{j})$ *be the correlation between the neighbourhood around* $p_1(i,j)$ *and the neighbourhood around pixel* $p_2(\hat{i},\hat{j})$ *in image* I_2.
2. *Compute the horizontal correlations* $C_{i,j}(i-\delta,j)$, $C_{i,j}(i,j)$, $C_{i,j}(i+\delta,j)$. δ *is a fraction of one pixel. The initial chosen value of* δ *is 0.5.*
3. *Fit a parabolic function, for example,* $C_{x,y} = ax^2 + by^2 + cxy$, *through these points and:*
4. *if the function has a negative second derivative, it has a maximum* C_{max} *at the point* x_{max}
   a. *If* $x_{\max} \in (i-1.5\delta, i+1.5\delta)$, *add i -* x_{max} *to* $H_{i,j}$, *the horizontal disparity.*
   b. *If* $x_{\max} \notin (i-1.5\delta, i+1.5\delta)$, $x_{\max} \longleftarrow 1.5\delta$, *add i -* x_{max} *to* $H_{i,j}$, *the horizontal disparity.*
5. *if the function has a positive second derivative, find* C_{max} *at the point* $x_{\max} \in (i-1.5\delta, i+1.5\delta)$, *add i -* x_{max} *to* $H_{i,j}$, *the horizontal disparity.*
6. *proceed similarly in the vertical direction.*
7. *Set* C_{max} *to be the average of the maximums of the correlations in the horizontal and vertical directions.*
8. *Add* $C \longleftarrow 0.7C_{\max} + 0.3C_{i,j}$ *to* $C_{i,j}$, *the confidence map.*
9. $\delta \longleftarrow 0.5\delta$, *repeat until the terminal condition is met.*

Figure 6.6 The sub-pixel matching strategy of MSSM

The matching process is performed on the sub-pixel level. The pixel between four neighbouring pixels, $p_{(i,\ j)}$, $p_{(i+1,\ j)}$, $p_{(i,\ j+1)}$, $p_{(i+1,\ j+1)}$, is interpolated using a 4-point

bilinear algorithm (chapter 4).

Figure 6.6 shows the matching strategy applied on the layers of the pyramid.

The image I_1 is warped to match the image I_2 by:

$$I_2`(i,j) = I_1(i + H(i), j + V(j))$$

On each layer of the pyramid, the horizontal and vertical vector maps, $\boldsymbol{H}$ and $\boldsymbol{V}$, are iteratively refined by matching the warped image $I_2`$ to I_2. The refinement process is illustrated on figure 6.7

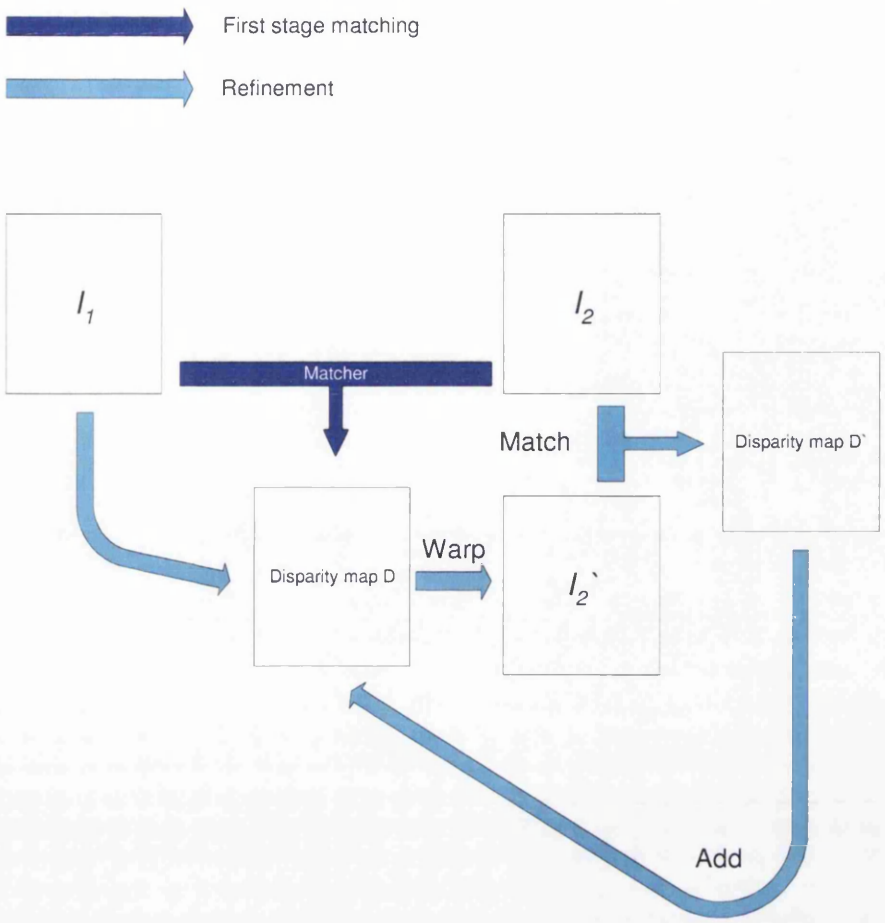

Figure 6.7 Refining the disparity maps by matching the warped image with the target image. Disparity map D was produced after matching image I_1 with I_2. I_1 was warped to match I_2, producing a warped image I_2`. The errors between $I_2$ and $I_2$` are estimated by matching I_2 with I_2`. The constructed disparity map D` is added to D, reducing errors produced by the first stage matching. The refining process could be iterated to yield better results.

At the beginning, all pixels in ***H*** and ***V*** were initialised to **0.0** and all pixels in ***C*** were initialised to **1**. In moving to successively greater layers, Pyr_i, the pixels in ***H***, ***V*** and ***C*** are provided from the matching performed in the previous layer, Pyr_{i-1}.

In figure 6.8, the disparity maps are shown encoded on a grey scale for simple

demonstration. Positive displacement is shown in a bright colour while negative displacement is dark.

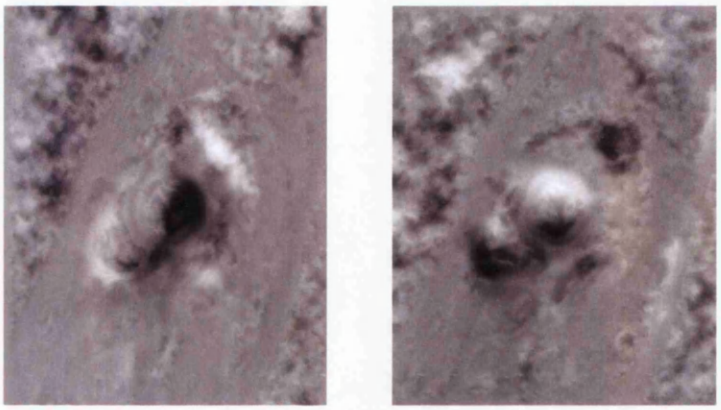

(a) (b)

Figure 6.8 The end systole and the end diastole of a random selected cardiac cine sequence were co-registered using MSSM. A horizontal disparity map (a) and a vertical disparity (b) were produced. The two disparity maps were encoded as brightness with positive displacements light and negative displacements dark.

Figure 6.9 shows a result of the warping. For comparison, absolute difference between and after the warping will also be shown in figure 6.8.

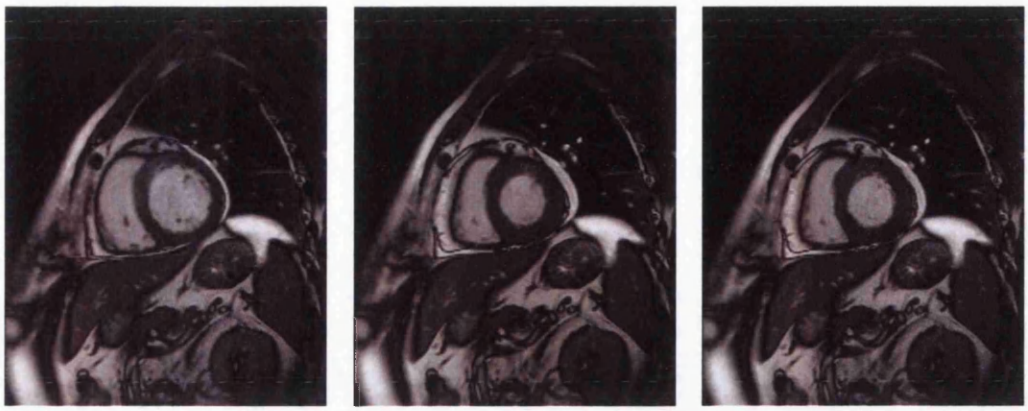

(a) (b) (c)

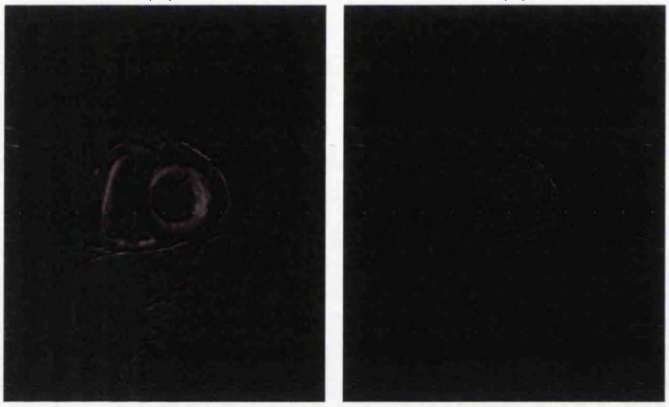

(d) (e)

Figure 6.9 (a) and (b) present the end diastole and the end systole in a cardiac cylce. MSSM matched (a) with (b), producing an image (c). (d) and (e) were the absolute difference between (b), (a) and (b), (c).

Using the horizontal and vertical disparity maps, cardiac motion is derived. Figure 6.10 shows cardiac motion of a patient with acute myocardial infarction in the vector space. The blue arrows show the normal motion while the red arrows indicate the abnormal motion.

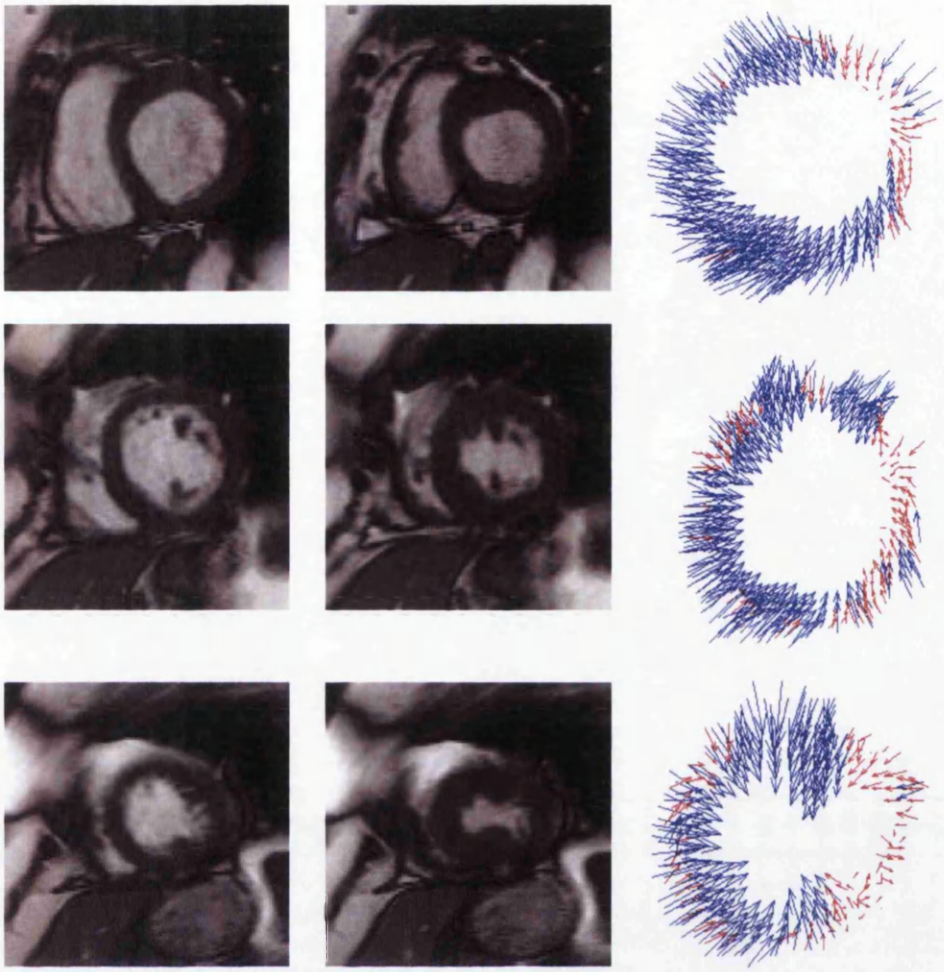

Figure 6.10 Cardiac MR images were acquired from the base, middle and the apex of the myocardium. MSSM matched the end diastolic and the end systolic images, producing disparity maps. Cardiac motion was derived from the disparity maps and shown as small arrows. The direction and the length of the arrows showed the direction and distance of cardiac motion. A threshold can be manually defined (5mm in this study) to differentiate healthy and unhealthy cardiac motion. The arrows with a length greater than the threshold are shown in blue color indicating the normal cardiac motion. In a similar way, the arrows shorter than the threshold are shown in red color suggesting the abnormal cardiac motion.

The benefits from MSSM are:

- It is insensitive to the contrast change.

- It is easier to find globally optimum disparity with the pyramid structure than by an exhaustive search algorithm.
- No user intervention is required to determine an initial set of matching points or region.

6.6 Building of the motion late contrast enhanced MR images

6.6.1 Correction of the late contrast enhanced MR image

Given a cardiac cine MRI sequence $I_{n=1...m}$, the cardiac wall motion data could be extracted by registering a reference image $I_{i\in n}$ with the other images in the sequence. This enables a set of disparity maps to be produced which estimates the motion of each pixel in the reference image. The disparity maps can be used to digitally warp the corresponding contrast enhanced MRI image if it has an identical or similar shape to the reference image.

Since cardiac images produced with MRI are ECG gated, it is possible to determine the trigger time point t of an MRI scanner during a cardiac cycle. Theoretically, if a reference image were acquired at the same time point as the acquisition of the late contrast enhanced image, the two images should be perfectly registered. However, in

practice, identical trigger time points cannot be guaranteed. Therefore, the image with the closest trigger time to the contrast enhanced image will be chosen as the reference image.

At present, contrast enhanced MRI image and cine MRI images are acquired separately. The patient motion, which is inevitable, could cause mis-alignment between the contrast enhanced image and the cine images (figure 6.11). In order to reduce the motion artifacts, the mis-registration must be corrected before further processing.

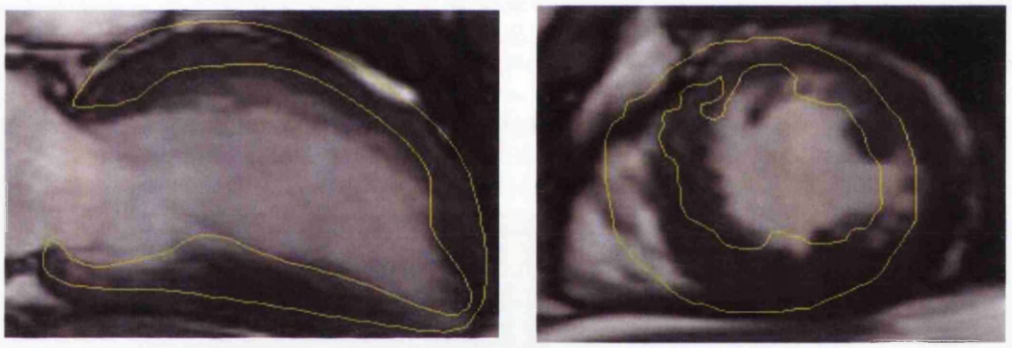

(a) (b)

Figure 6.11 The misregistration between cine MR images and the late contrast enhanced MRI image from (a) long axis view; (b) short axis view. The contours were defined manually on the late contrast enhanced images and projected to the cine images.

The correction involves a mutual information based rigid registration. Mutual information measures the shared similarity between two images by exploiting the characterisation of the data distribution in the joint-histogram. Mutual information is a powerful similarity criterion especially in multi-modality image registration because

of its immunity to the contrast variety. In this study, the inherent image contrast in contrast enhanced images and the cine images is generally different. We believe the employment of mutual information can enhance the results. A global searching was utilised to find the optimised transformation. Since the research interest is mainly focused on the left ventricular myocardium, the global searching can be simplified to the searching of a region of interest (ROI) in a slightly larger searching window (figure 6.12). Both the ROI and the searching window are adjustable in order to handle different images. We suggest that the searching window should be at least 10 pixels larger in both the height and the width of the ROI to tolerate the relatively significant motion.

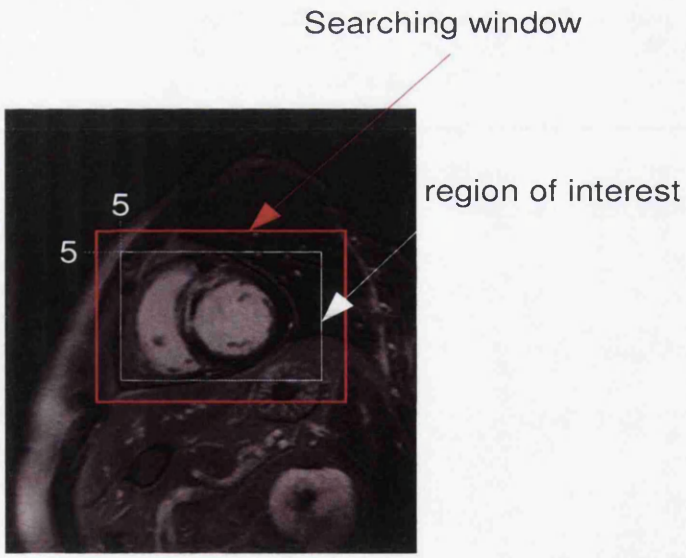

Figure 6.12 The searching strategy of the rigid image registration algorithm, which aligns the late contrast enhanced MR image to its corresponding cine image.

D. Rueckert et al. suggested the use of an affine transformation to compensate the motion artefacts in their work (Rueckert et al., 1999). The estimation of affine transformation parameters by full search algorithm is time consuming. In our study, we acquired images from the same imaging plane for both cine MR images and the late contrast enhanced MR images. We postulated that a rigid transformation which involves only two degrees of translation would be sufficient because of the limited motion space inside an MRI scanner. Once the translation function T is determined, it is applied to the entire image. We introduced a checkerboard system to examine the alignment results. A checkerboard image shows square blocks of two images alternately for the comparison purpose. Figure 6.13 examines three images after the alignment using the checkerboards. The images include two short axis slices with small and large areas of contrast enhancement and a long axis slice with a large area of contrast enhancement.

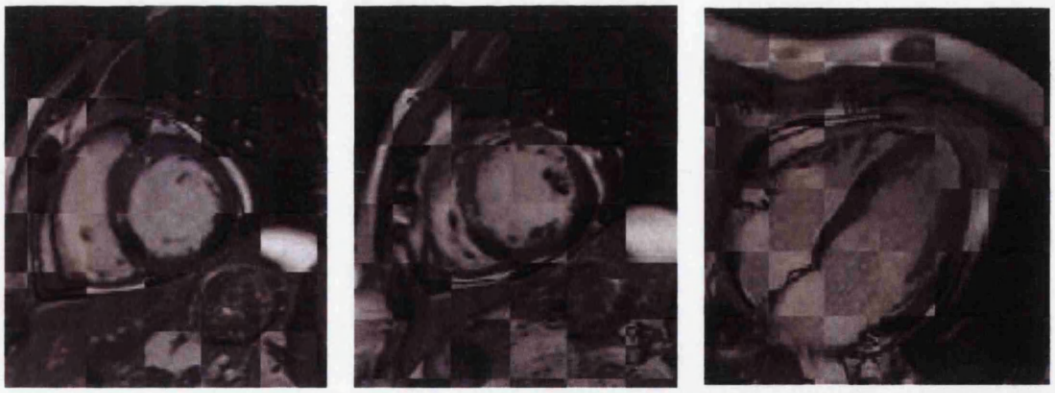

Figure 6.13 The late contrast enhanced images were registered with its corresponding cine MR image. The alignment results were shown as checkerboards with segments from two aligned images. .

6.6.2 Building of the cine late contrast enhanced images

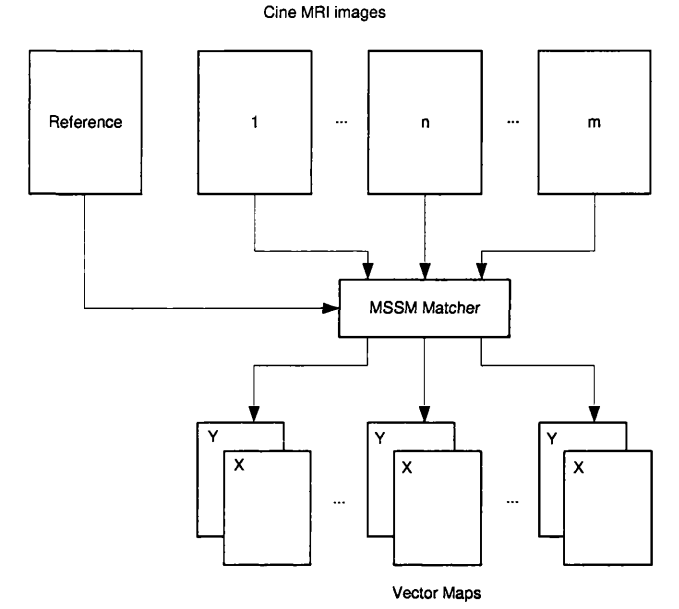

(a)

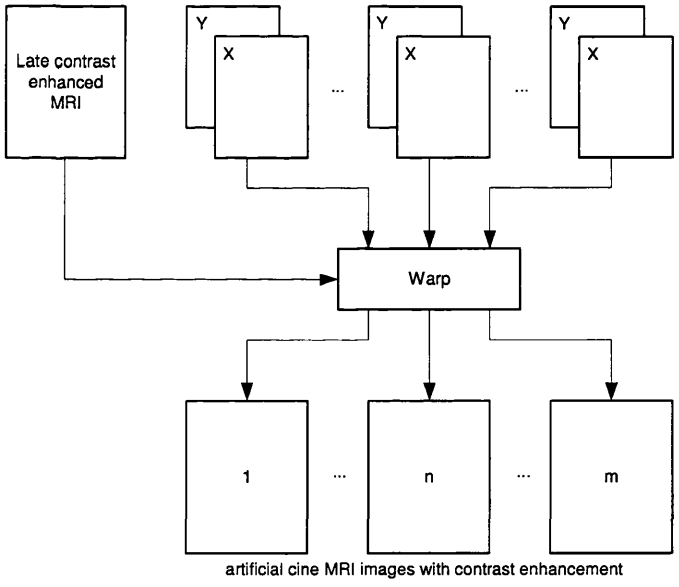

(b)

Figure 6.14 a). A reference image is manually selected from a cine MRI images. It was matched with the other images in the sequence, which produces a set of disparity maps; b). the late contrast enhanced MRI image is digitally deformed to create a image sequence using the generated vector maps. The sequence is considered as a sequence of artificial cine image with late contrast enhancement. In this study, we referred this method to as the "all to one" matching.

The reference image $I_{i\in n}$ is selected to register with other images in the cine sequence using MSSM, building a set of disparity maps. The motion corrected late enhanced inage l is digitally warped using the disparity maps.

The output images $l_{i=0,\ldots,m}$ are the artificial cine images incorporating the late enhancement information. Figure 6.14 illustrates that the process which produces the notion late contrast enhanced images.

This method is called "all to one" matching. Alternatively, we can choose a so-called "one to one" matching method. The "one to one" matching runs on each adjacent pair of images starting from the selected reference image r (figure 6.15). The late contrast enhanced MRI image is then warped progressively to produce the motion late contrast enhanced sequence.

Using the pyramidal structure, MSSM can find the global maxima efficiently. However, in the situation of significant cardiac motion, a one-to-one matching strategy has the potential to produce more precise results because the degree of motion between two neighbouring images is limited. However, MSSM utilises a low-pass filter iteratively during the matching and the warping, which smooths the warped image. Using the one to one matching strategy, an image is constructed from the previous constructed images. Therefore the smooth effect will accumulate from the previous images to the constructed image. In such a case, the visual quality of the

inage at the end of the image sequence could be severely affected, especially when long image sequences are employed.

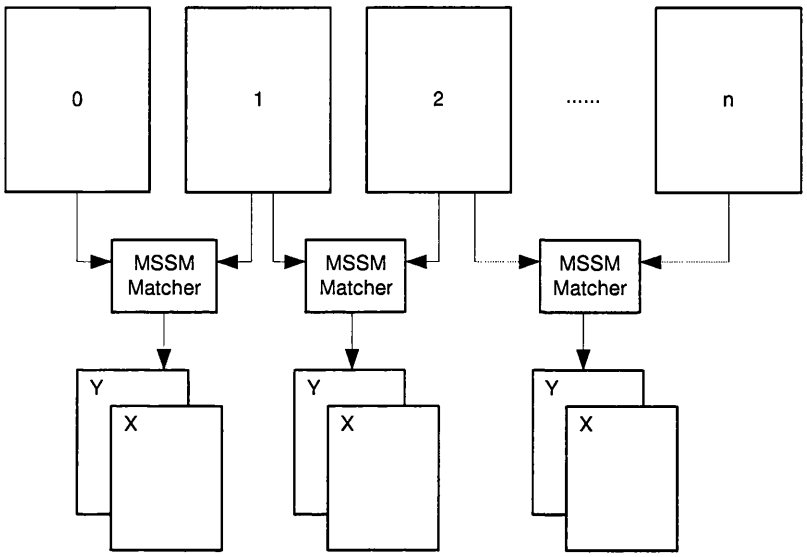

Figure 6.15 In the one to one matching strategy, the matching process starts from the selected reference image (the first image in this example). Each image in is matched with its neighbour, producing a disparity map. The late contrast enhanced MR image is then warped progressively to produce the cine late contrast enhanced sequence.

To utilise the advantage of the "one to one" method while avoiding its disadvantage, we developed a so-called "n to one" matching strategy.

Using the "n to one" matching strategy, the image sequence is divided into groups. Each group contains n images. The first image of each group, I_0, I_n, I_{2n}, ... are matched "one to one". Within the groups, images are matched with the first image using the "all to one" strategy.

Figure 6.16 illustrates the process of the "n to one" method.

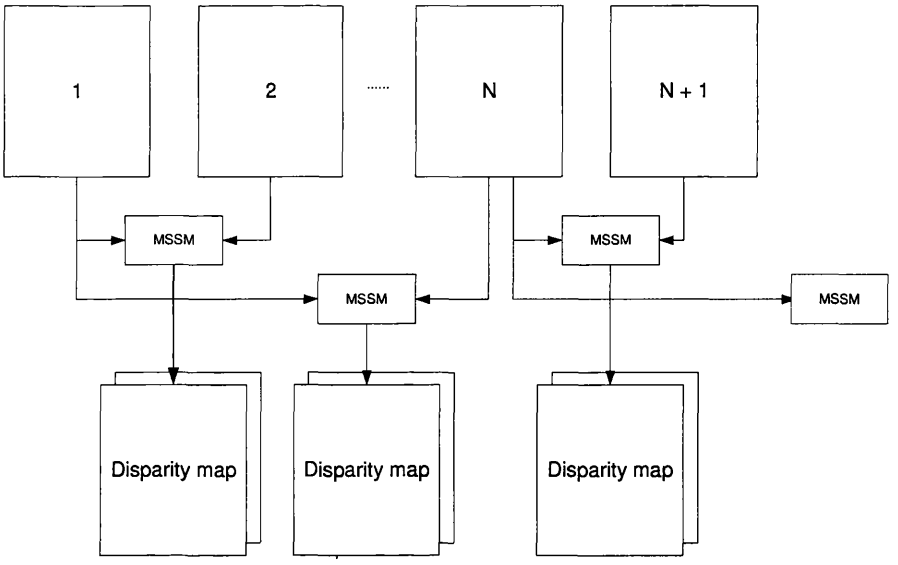

Figure 6.16 In the "n to one" matching strategy, the image sequence is partitioned into groups, each of which contains n images. For each group, a reference image is selected. The reference image is matched with the other images in the group using the "all to one" matching strategy. The reference images in the groups are matched using the "one to one" strategy.

The "n to one" matching strategy seeks the balance between the "all to one" method and the "one to one" method. It produces better estimation by matching the images with limited motion and avoids the image quality decay due to the iterative warping. Our pilot study concludes that the "n to one" method has the best overall performance. The experimental results will be discussed in the following section.

6.7 Experimental Results

6.7.1 Data acquisition

MRI was performed on subjects with a median age of 69 years on a Siemens Sonata 1.5T system using a phased array chest coil. LV dimensions were evaluated using a cine TrueFISP breath-hold sequence. Cardiac triggering was used in the scan. Image parameters were TR/TE of 3.2 ms/1.58ms, 208 x 256 matrix sizes, flip angle 52°.

Late contrast enhanced MR was performed 10 minutes after injection of 0.2 mmol/kg gadolinium-DTPA using a breath hold segmented TurboFLASH inversion-recovery sequence. The image parameters, including the FOV, matrix size, slice thickness and slice gap, were identical to the corresponding cine MR images.

6.7.2 MSSM

The MSSM algorithm has been applied to match the cine MRI images selected from the database of Glasgow Cardiac MR Unit. We assess the performance of MSSM from its: 1). Accuracy; 2). Efficiency and 3). Robustness.

Accuracy

In the experiment, the end diastole and the end systole were defined manually. The end diastolic image was matched with and warped to the end systolic image. To evaluate the quality of the warped images, we compared them with the original end systolic images in terms of the mean square error (MSE) and the correlation coefficient (CC),

$$MSE = \frac{\sum_m \sum_n (I(x,y) - I`(x,y))^2}{m \times n}$$

$$CC = \frac{\sum_n \sum_m (I(x,y) - \bar{I})(I`(x,y) - \bar{I`})}{\sqrt{\sum_m \sum_n (I(x,y) - \bar{I})^2 \sum_m \sum_n (I`(x,y) - \bar{I`})^2}}$$

where m and n are the width of height of the input images. $I(x,y)$ and $I`(x, y)$ are the pixel intensity, where $x \in n, y \in m$. $\bar{I}$ and $\bar{I`}$ are the mean pixel intensities of the two input images.

Five cine MRI sequences were selected from consecutive studies from the database in Glasgow Cardiac MR Unit to evaluate the three matching strategies, including the "all to one" method, the "one to one" method and the "n to one" method. For each sequence, a short axis slice was selected from the middle of the heart. The end diastole and the end systole were manually defined. For all of the five slices, the end

diastole images were warped to match the end systolic images following the "all to one" strategy, the "one to one" strategy and the "n to one" strategy. For the "n to one" strategy, n is set to 3. The warped systolic images are compared with the original systolic image in term of MSE and CC. The results are summarised in table 6.1:

Comparison in term of MSE				
Subject	Before MSSM	After MSSM All to one	After MSSM One to one	After MSSM N to One (n=3)
1	30.07	11.37	12.08	11.15
2	27.42	16.92	17.3	15.78
3	26.67	14.13	11.43	9.29
4	22.70	10.74	10.55	7.93
5	18.58	9.97	10.12	7.55
Mean±SD	25.09±4.49	12.62±2.87	12.3±2.90	10.33±3.35

Comparison in term of CC				
Subject	Before MSSM	After MSSM All to one	After MSSM One to one	After MSSM N to One (n=3)
1	0.81	0.95	0.93	0.97
2	0.77	0.94	0.92	0.92
3	0.72	0.74	0.93	0.97
4	0.75	0.90	0.91	0.96
5	0.87	0.95	0.93	0.98
Mean±SD	0.78±0.06	0.89±0.09	0.92±0.01	0.96±0.02

Table 6.1 *Cardiac cineMR images were acquired from 5 subjects. For each subject, a slice was chosen from the middle of myocardium. For each slice, the end diastolic image was warped to match the end systolic image. The warped images were compared with the original end systolic images by both MSE and CC.*

From table 6.1, the n to one matching strategy has the best overall performance.

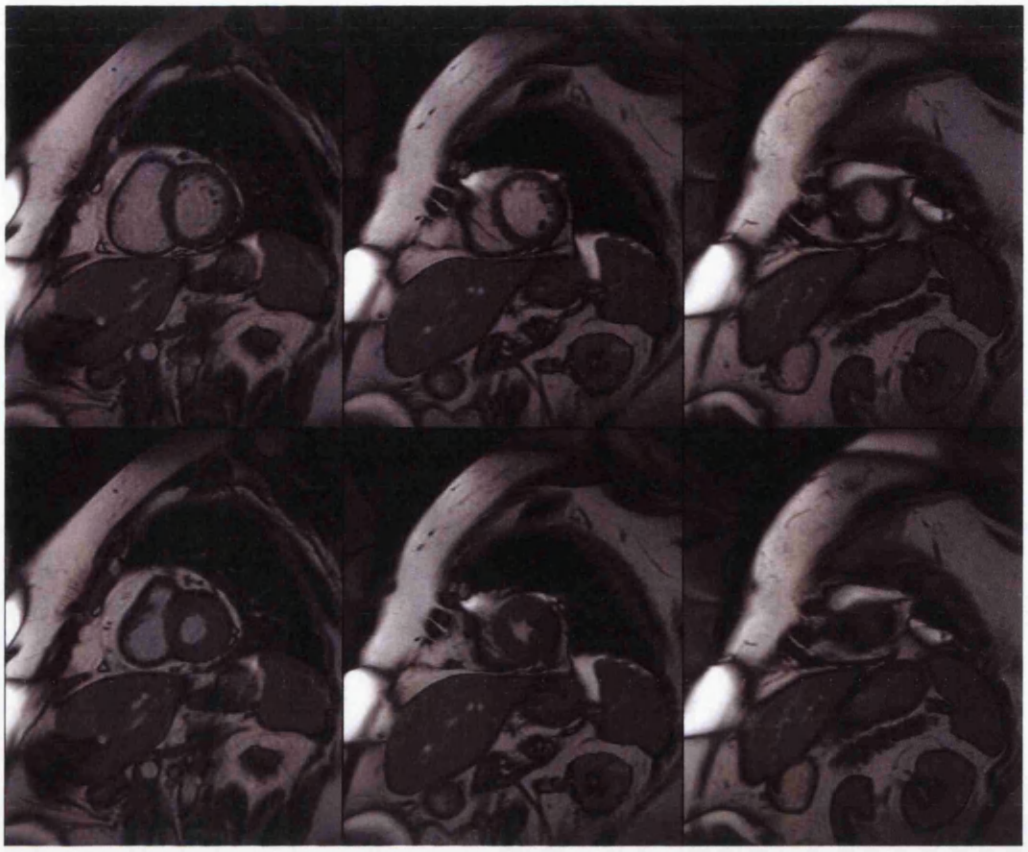

Basal Mid Apex

Figure 6.17 For each scan, a basal slice, a middle slice and an apical slice were chosen in the MSSM accuracy test. The first row shows the end diastolic images and second row shows the end systolic images.

Twenty CINE MRI scans were selected from consecutive studies from the database in the Glasgow Cardiac MR Unit. For each sequence, three short-axis slices were chosen from the base, the middle and the apex of the heart following the America Heart Association recommendation (Cerqueria et al., 2002). A randomly selected image set from the testing data is shown in figure 6.17. For each of the 60 slices, the end diastolic image and the end systolic image were manually defined.

The warped end systolic image was evaluated against the original end systolic image

using both MSE and CC. However, since most non-cardiac tissues in the MRI images were relatively static compared to the myocardium, a region of interest is selected to cover only the left and the right ventricles, ensuring that the evaluation would focus on the myocardium (figure 6.18). Table 6.2 summarises the results of the registration quality of the healthy volunteer data set in terms of MSE and CC.

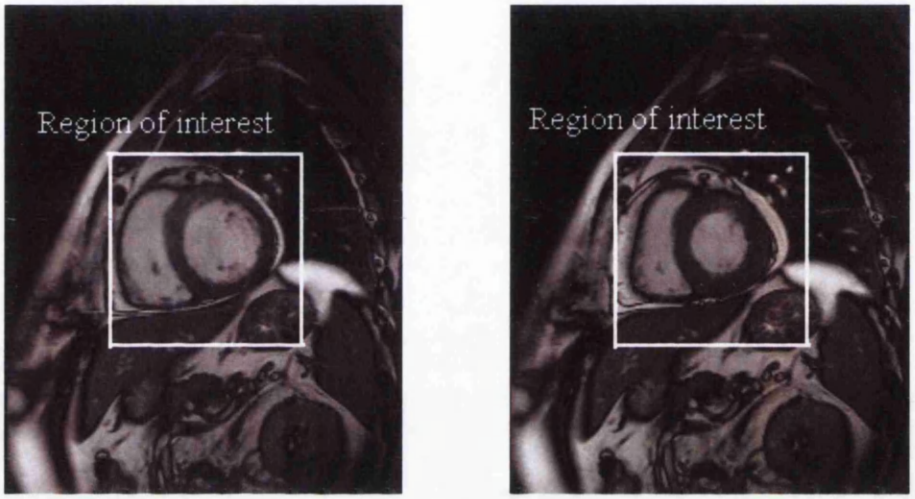

Figure 6.18 Most of tissues are relatively static compared to myocardium. To precisely evaluate the ability of the image registration algorithm using MSE and CC, a region of interest was defined manually. Only the pixels in the regions of interest were evaluated by MSE and CC.

	MSE (mean ± std[4])		CC (mean ± std)	
	Before MSSM	After MSSM	Before MSSM	After MSSM
Basal slice	30.65±6.25	14.61±4.37	0.70±0.03	0.93±0.09
Mid slice	28.74±5.56	11.18±3.60	0.71±0.10	0.95±0.03
Apical slice	28.55±8.33	10.99±2.72	0.66±0.16	0.95±0.02

Table 6.2 Cardiac cine MR images were acquired from 20 subjects. For each subject, three slices were chosen from the base, middle and the apex of myocardium. For each slice, the end diastolic image was warped to match the end systolic image. The warped images were compared with the end systolic images by MSE and CC.

[4] Std: standard deviation.

The overall results are shown in figure 6.19 and figure 6.20.

One result of MSSM and the corresponding difference image are shown in figure 6.21. Before MSSM, the difference image shows a substantial amount of motion artefacts (figure 6.21d). Figure 6.21c shows a post-MSSM image. The corresponding difference image (figure 6.21e) shows a significant reduction of motion artifacts.

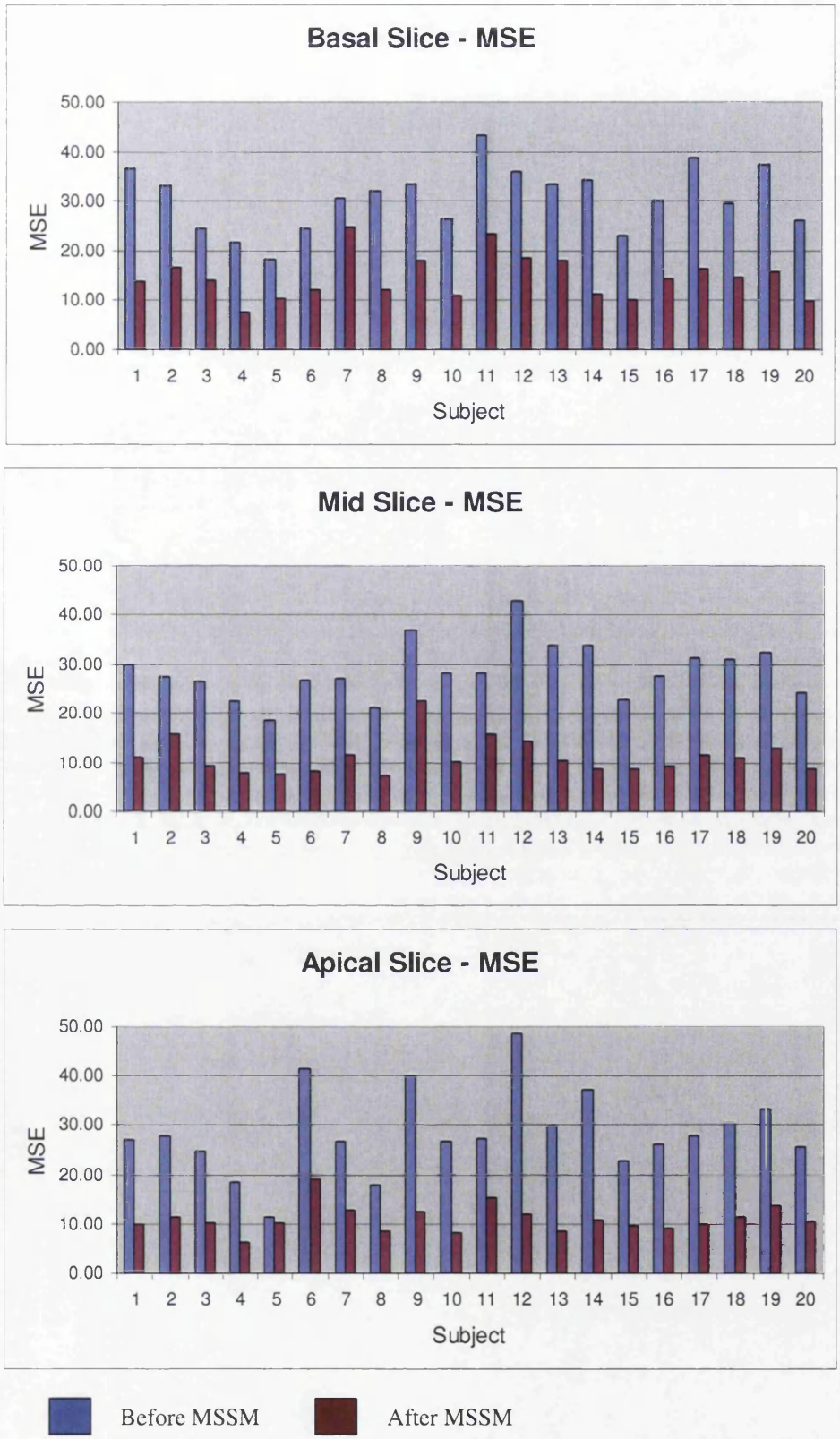

Figure 6.19 Overall comparison of the registration error in term of MSE before and after MSSM.

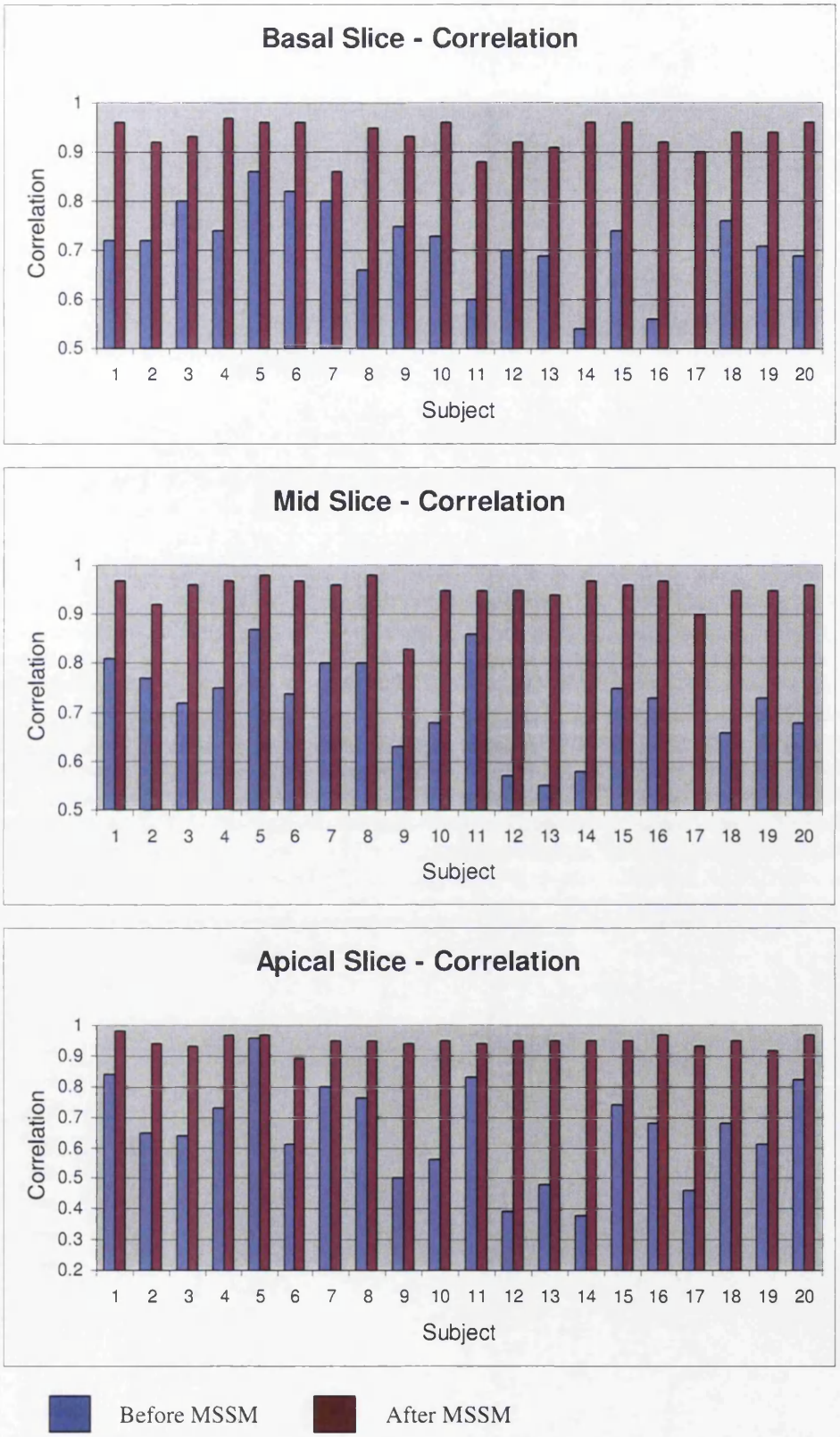

Figure 6.20 Overall comparison of the registration error in term of correlation coefficient before and after MSSM.

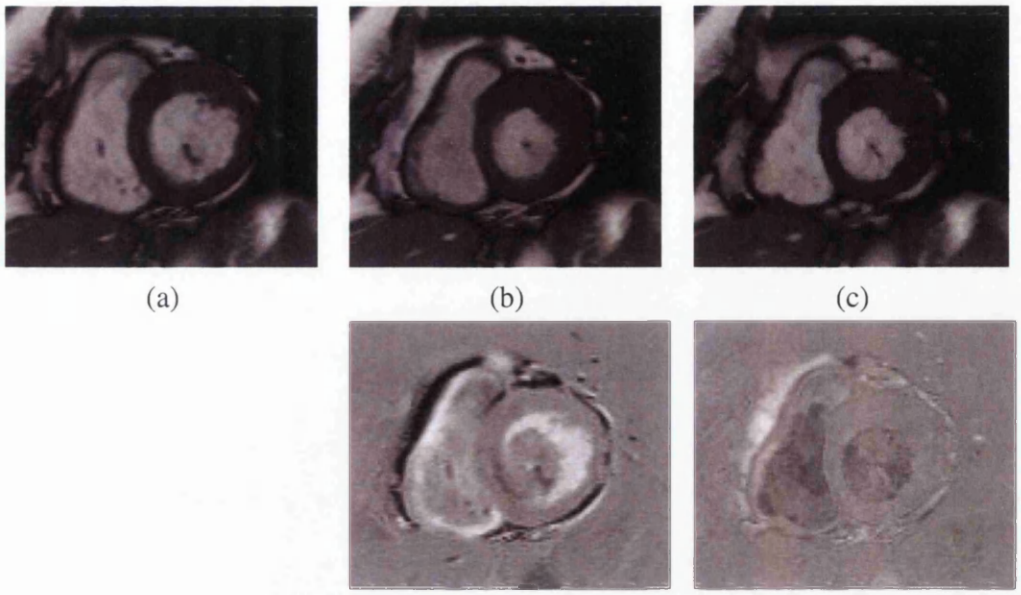

Figure 6.21 The end diastolic image (a) was matched with the end systolic image (b), producing a disparity map which can be used to warp the diastolic image to the systolic image, generating an artificial systolic image (c). The corresponding difference images are shown in (d) and (e). For image (a) and (b), the MSE is 34.12, the correlation coefficient is 0.76. After MSSM, for the image (b) and the generated image (c), the MSE is 36.92 and the correlation coefficient is 0.94.

Efficiency

MSSM is an efficient image registration algorithm. The pyramidal structure is built to reduce the computational complexity as well as increase the searching accuracy. The matching starts from the coarsest layers and moves successively toward the greater layers. The calculation of the cross-correlation is computationally complex. However, the computing time was minimised since only four neighbouring pixels are involved in the searching process for each pixel. Other time consuming parts involved in MSSM are:

1. The building of the differential pyramid which employs multiple convolution filters and interpolations.
2. The smoothing of the vector map. For each layer of the pyramid, the output vector map is smoothed by a Gaussian filter to avoid the discontinuous motion.
3. The refinement of the vector map. For each layer of the pyramid, the matching is repeated to achieve more accurate results.

In the implementation, the Intel image processing library (IPL)[5], which is optimised for the Intel MMX technology, was employed to increase the processing speed.

The efficiency of MSSM was evaluated by matching two images with the size of 512x512 and the depth of 8 bits per pixel. The matching was performed 10 times using a mainstream personal computer equipped with an Intel Pentium4 2.2 GHz processor and 512MB RAM memory. The elapsed time is listed in table 6.3.

[5] The IPL was later replaced by an open source project called OpenCV, which can be downloaded freely from http://sourceforge.net/projects/opencvlibrary

Number	Elapsed time (ms)
1	1.59
2	1.59
3	1.59
4	1.61
5	1.61
6	1.63
7	1.61
8	1.63
9	1.61
10	1.63
Mean (±SD)	1.61±0.015

Table 6.3 The efficiency of the MSSM

Robustness

The robustness tests the algorithm's resistance to the noise. Two types of artificial noise were added to the source images. The first type of noise is called "salt and pepper" (Morris, 2003). Salt and pepper noise is also called impulse error and spike error (Umbaugh, 2005) and is generally caused by errors in the data transmission. The corrupted pixels are set to either the maximum value or zero, giving the image a "salt and pepper" look. We implemented the noise generator using mathematical software Matlab (Mathwork). The density of the noise, d controls how noisy the image looks. It is calculated by dividing the number of corrupted pixels in the image by the total number of pixels:

$$d = \frac{numberOfCorruptedPixelsIn\,\mathrm{Im}age}{numberOfPixelsIn\,\mathrm{Im}age}$$

Figure 6.22 shows a set of cardiac images with different noise density.

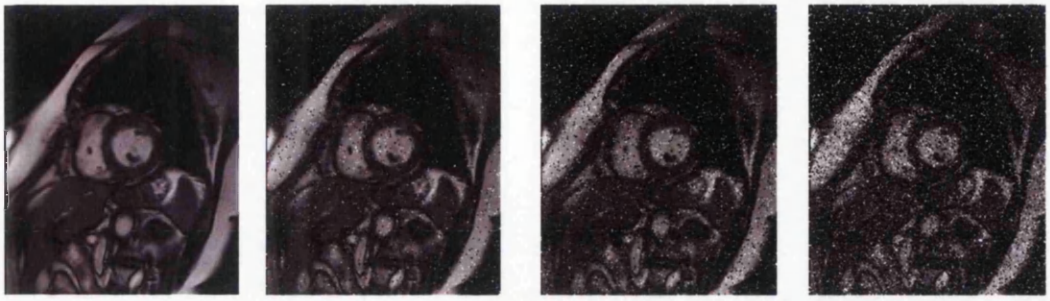

(a) (b) (c) (d)

Figure 6.22 "Salt and pepper" noise. a). the image without artificial noise; b). noise density d=0.05; c). d = 0.1; d). d = 0.2.

The second type of noise is called "speckle noise", which adds multiplicative noise using the equation:

$$I`(x, y) = I(x, y) + nI(x, y), n \in (0, v]$$

where I and $I`$ are the original and result images. v is the noise variance defined by the users, and n is a random number between 0 and the noise variance v. Figure 6.23 shows four images with different noise variance v.

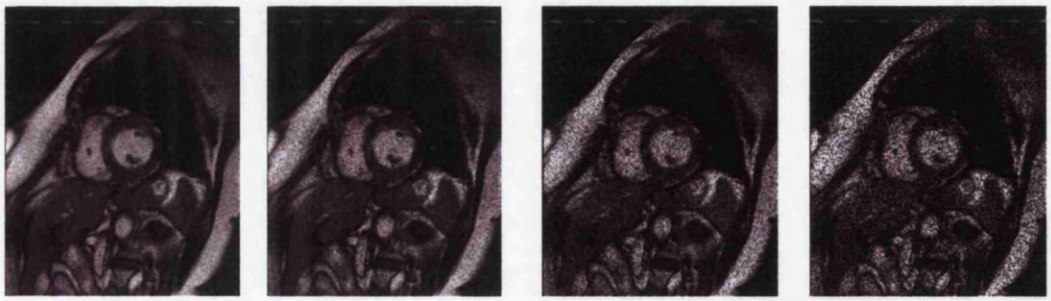

(a) (b) (c) (d)

Figure 6.23 "Speckle" noise. a). v=0.02; b).v=0.05; c). v = 0.1; d). v = 0.2.

An image sequence was randomly selected from the testing data. Four degrees of "salt and pepper" and "speckle" noise were added to the both the end diastolic and the end systolic images. Then, the diastolic image was matched with and warped to the systolic image. MSEs were calculated to assess the matching results.

Tables 6.4 and 6.5 summarized the matching results with the presence of "salt and pepper" noise and "speckle" nose in term of MSE.

Figure 6.24 shows the results of the noise resistance test.

"Salt and pepper" noise				
ID	Noise density (d)	MSE		
		Before	After	Improvement
1	No noise	35.42	39.01	3.59
2	0.02	33.61	37.99	4.38
3	0.05	32.43	35.32	2.89
4	0.1	31.09	35.40	4.31
5	0.2	29.73	33.34	3.61

Table 6.4 MSSM's resistance to the "salt and pepper" noise

"Speckle" noise				
ID	Noise variance (v)	MSE		
		Before	After	Improvement
1	No noise	35.42	39.01	3.59
2	0.02	34.85	38.14	3.29
3	0.05	34.26	38.14	3.88
4	0.1	33.56	38.14	4.48
5	0.2	32.51	34.51	2.00

Table 6.5 MSSM's resistance to the "speckle" noise.

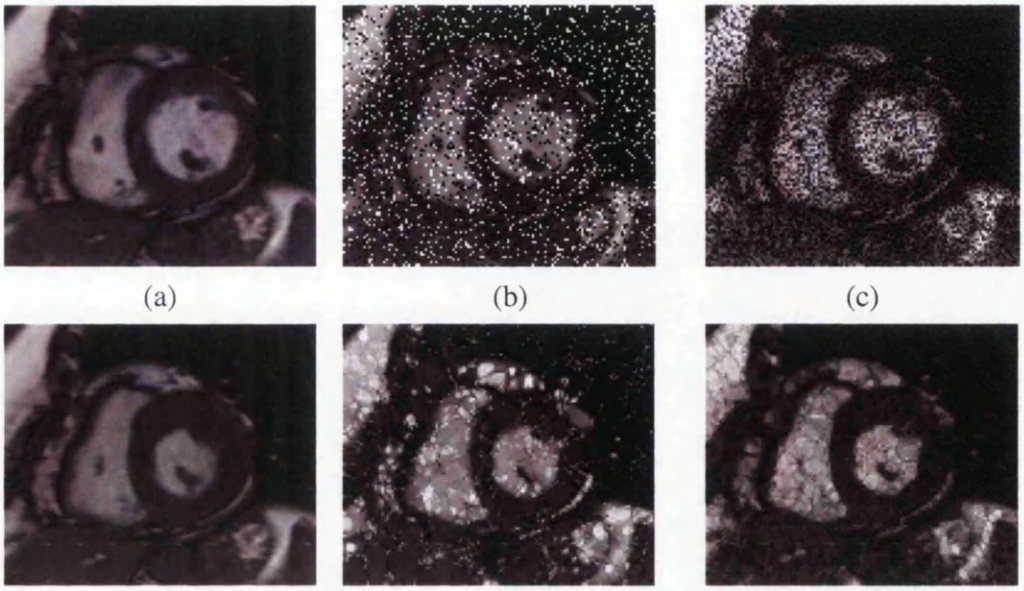

Figure 6.24. (a). the original diastolic image; (b). the diastolic image with "salt and pepper" noise (d = 0.2); (c). the diastolic image with "speckle noise" (v = 0.2); (d). the original systolic image; (e). the warped systolic image from the "salt and pepper" image compared to the original systolic image; (f). the warped systolic image from the "speckle" image.

6.7.3 Cine late contrast enhanced MRI

Twenty patients with chest pain who were both troponin I and late contrast enhancement positive were recruited. A reference image was selected manually from each of the short axis slices. The mis-registration between the reference image and its corresponding late contrast enhanced image was corrected using a mutual information based full search registration algorithm. MSSM were employed to extract the motion vector from each of the short axis slices following the "n to one" matching strategy (n = 3). The corrected contrast enhanced MR images were warped to build the cine

contrast enhanced sequence. The mean of the cardiac parameters, including the left ventricle end diastolic volume and left ventricle end systolic volume, were compared between the original cine sequence and the warped sequence. Student t-test value, *p*, was computed to reveal the statistically significant differences between the two data sets. The two data sets were deemed to have no significant differences if the t-test value was greater than 0.05 ($p > 0.05$).

Mean left ventricle diastolic volume in each of the slices was measured by planimetry (original / warped) = 206 / 215 ml. The t-test shows there is no significant difference between the left ventricle diastolic volume of the original image and the warped image ($p = 0.35 > 0.05$). Left ventricle systolic volume = 129 / 123 ml, $p = 0.33$. The overall data are presented in figure 6.25.

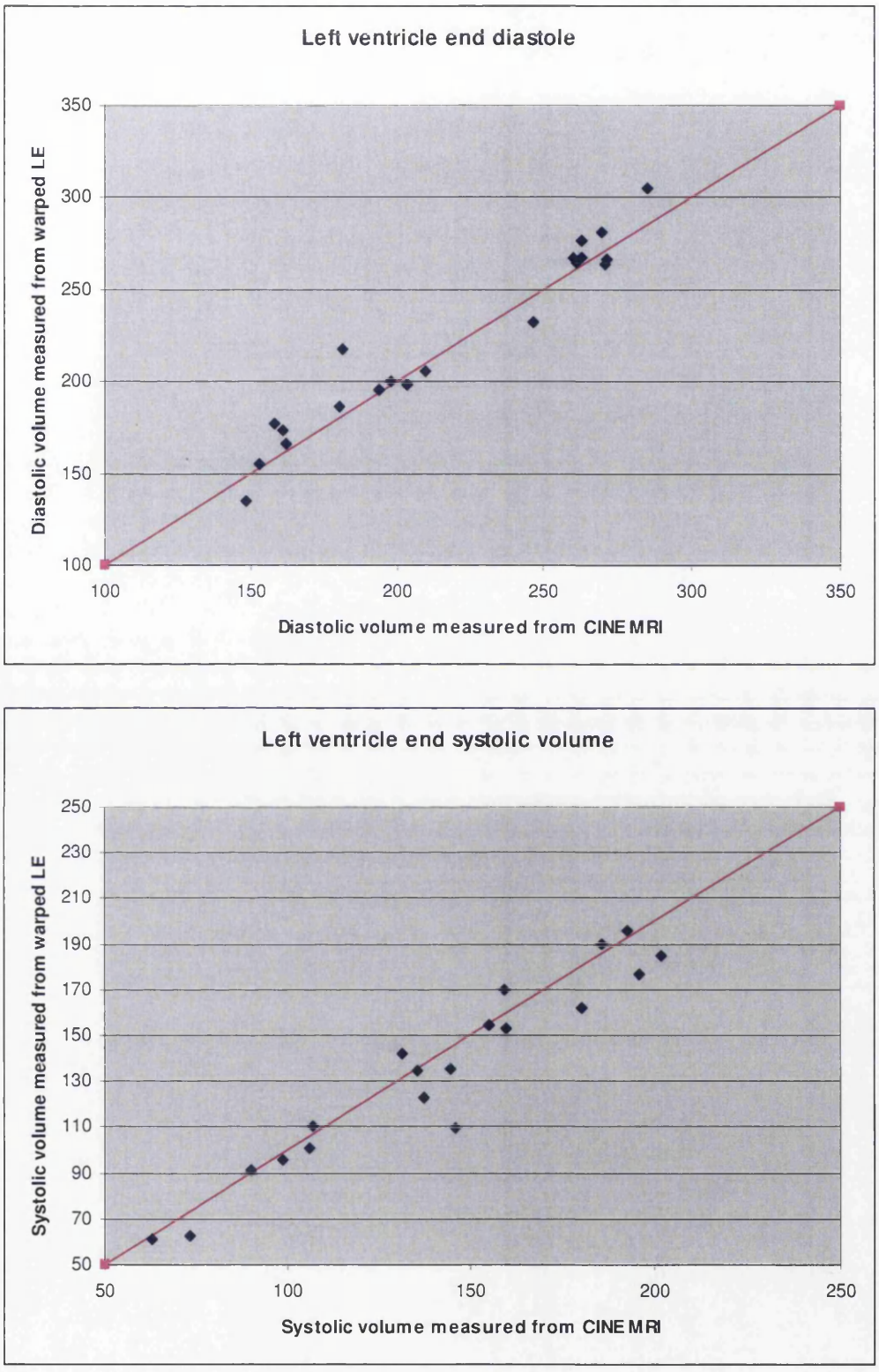

Figure 6.25 The comparison between the cine contrast enhanced MR images and the original cine MR images.

The error distributions are shown in figure 6.26.

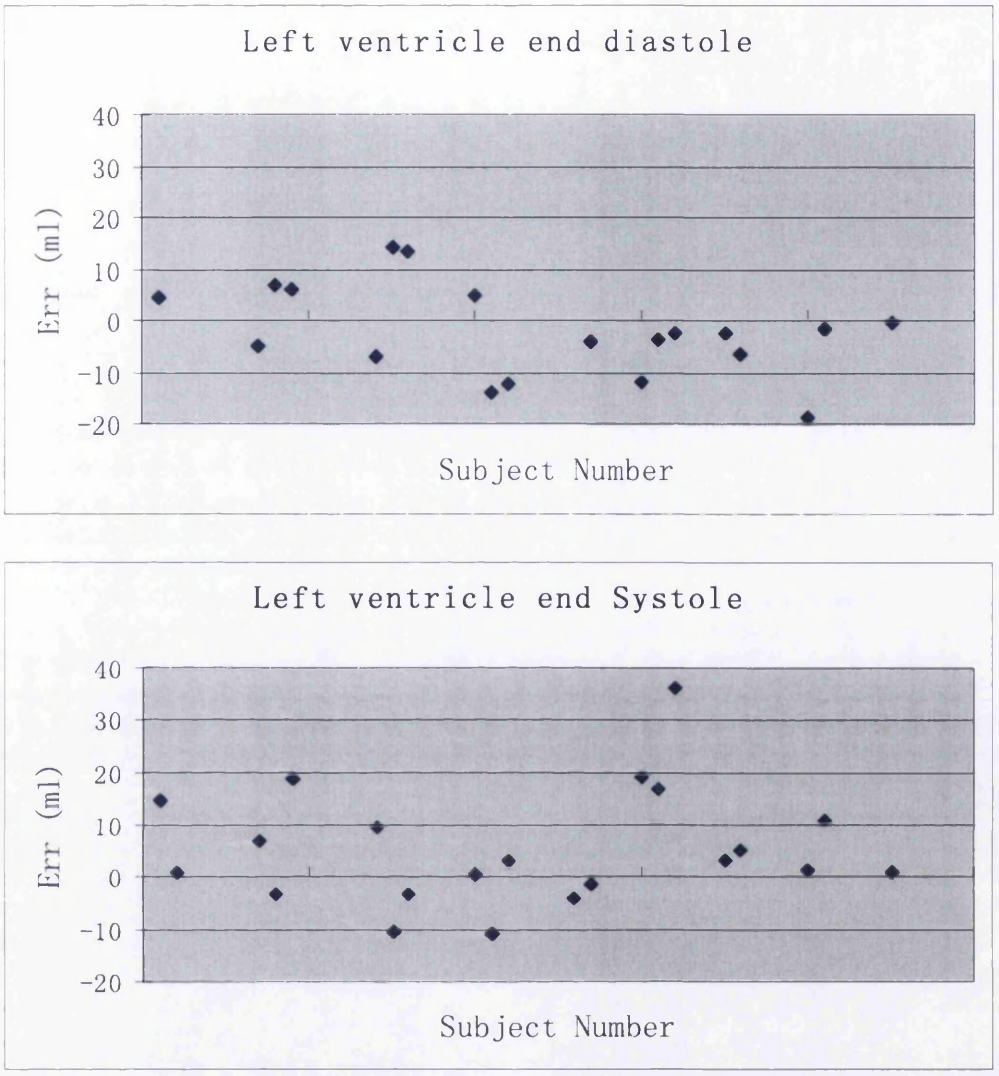

Figure 6.26 The errors between the cine contrast enhanced MR images and the original cine MR images.

An example of the cine contrast enhanced sequence is shown in figure 6.27.

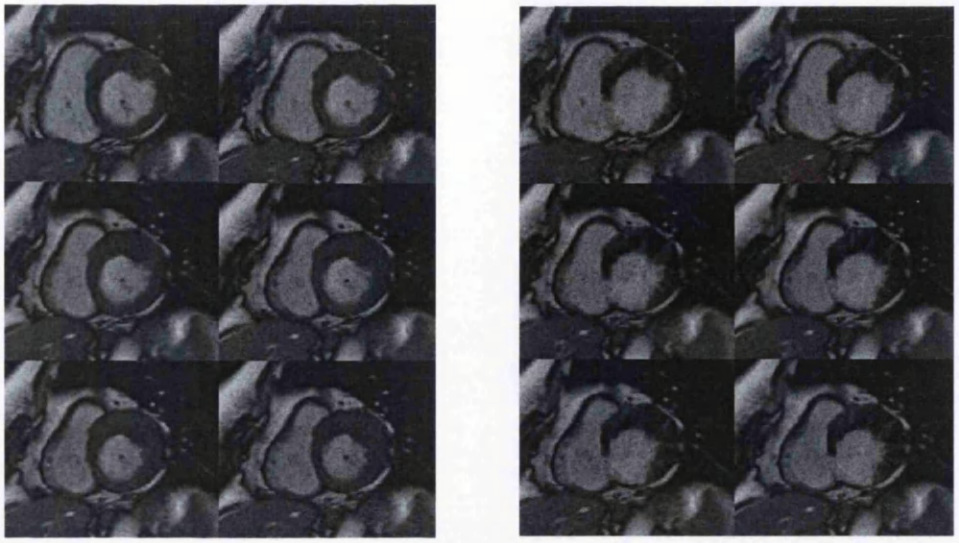

Figure 6.27 The cine MR images and the cine contrast enhanced MR images. The six images on left are cine images. Their corresponding warped contrast enhanced images are shown on the right.

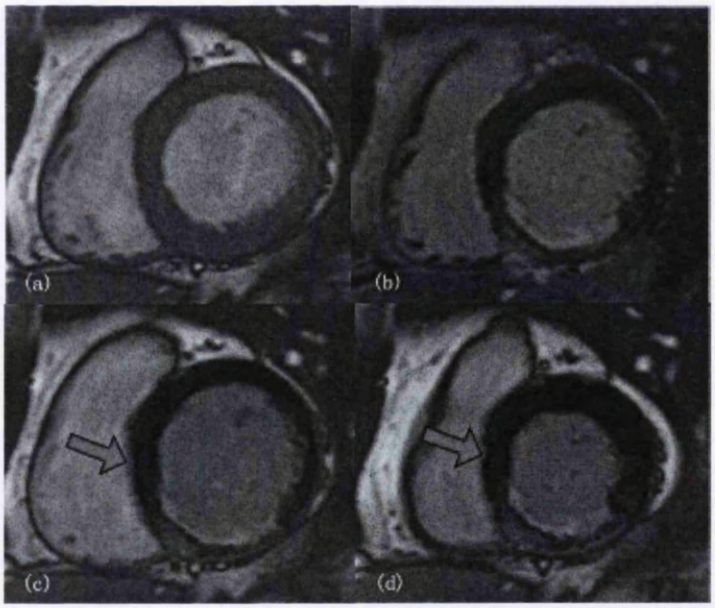

Figure 6.28 Location of the hibernation myocardium from the cine late contrast enhanced MR images. The end diastolic and the end systolic frames of a cine contrast enhanced sequence. The arrows suggested the potential hibernating myocardium.

The other example is shown in figure 6.28. The two images are the end diastolic and the end systolic frames from a cine contrast sequence. The arrows show the

myocardium without contrast enhancement, but on playback it moves abnormally. This is the suspicious hibernating myocardium.

6.8 Discussion and future work

6.8.1 Discussion

Late contrast enhanced MRI, in combination with cine MRI, has shown great potential for identifying reversible myocardial dysfunction. Simultaneous study of late contrast enhanced MRI and cine MRI in the form of an integrated late enhancement cine image brings three major benefits:

1. It enables fast location of a reversible myocardial infarct.
2. It improves the accuracy of diagnosis of reversible myocardial infarcts and reduces the observer dependence.
3. It enables the study of the muscle motion neighbouring the infarct during systole, in order to study the neighbourhood effect (Fieno et al., 1999).

Q. Chen and his colleagues proposed a method making contrast enhancement cine MRI images by exploiting the T1 / T2 difference after injecting Gd-DTPA. Chen's method is straightforward and easy to implement but cannot guarantee visible late enhancement which therefore limits its clinical application. In this study, we developed an alternative method. Compared to Chen's work, our method, a purely

software one is more flexible. Our method by the use of algorithms integrates information from cine MRI and late contrast enhanced MRI to produce a late enhanced cine sequence. As a result, the output shows the best features of cine MRI images, as well as the optimum contrast and therefore infarct depiction of late enhancement. The experimental results show no significant difference in left ventricle diastolic volume and left ventricle systolic volume. The results strongly suggest that our method would provide an improved viability assessment tool.

6.8.2 Future work

In many circumstances, errors could be produced. Firstly, the image registration can only find the statistically best estimation of cardiac motion while the realistic motion may be different. Secondly, the selected reference image cannot be identical to its corresponding late contrast enhanced MRI image. With the presence of late contrast enhancement, it is difficult to precisely register it with the reference image. The first error can be minimised by a robust image registration algorithm. The second potential error source can be well controlled by the ECG gated MRI scanner. The third situation which might produce errors is the through plane motion of myocardium. It is known that the cardiac motion is complex. It involves the through plane motion as well as the horizontal motion. The registration algorithm we used in this study is two dimensional. Therefore, the motion we extracted only includes the motion in the 2D plane. Although the effect of through motion, location and shape of the infarct remains unknown, it is possible that with the presence of the through plane motion, the healthy

myocardium might move down to "replace" the myocardial infarction in the 2D slice obtained during the cardiac cycle. In other words, in the cine contrast enhanced MRI images, the contrast enhancement may disappear gradually during the systolic phase. A 2D image registration algorithm cannot predict or cope with such a situation.

In practice, an MRI scanner acquires MR signals from a slice with a defined thickness instead of an infinitely thin plane. The slice thickness in our study was defined as 8mm plus a 2mm gap between slices. Normally, 6-12 slices are required to cover the entire myocardium depending on the size of the heart. The quantisation errors during any quantitative study of myocardium are inevitable. The hypothesis is that the quantisation errors may completely or partially dwarf the errors introduced by the through plane motion of the myocardium. However, it is difficult to prove the hypothesis practically. The ideal solution for the argument is to develop a 3D image registration algorithm which can extract cardiac motion in 3D space. In recent years, many 3D image registration techniques have been invented (Moshfeghi et al., 1994; Maes et al., 1997; Penney et al., 1998; Rohlfing et al., 2003; Rao et al., 2004). They have been applied in different MRI studies, including breast MRI (Rohlfing et al., 2003), functional MRI (Rao et al., 2004), cardiac tagged MRI (Rao et al., 2004), first-pass perfusion MRI (Slomka et al., 2004) and etc. However, no reports have been made about the study of cardiac cine MRI using 3D image registration. A full investigation in the future will be worthwhile.

6.9 Conclusion

In this chapter, a novel method for left ventricle viability assessment using combined cardiac cine and late contrast enhanced MRI images was introduced. We have shown that there are no significant differences in left ventricle diastolic volume (206 / 215 ml, $p = 0.35$) and left ventricle systolic volume (129 / 123 ml, $p = 0.33$).

In this chapter, we mentioned Chen's work which also produces cine late contrast enhanced MR images. His method adopts the existing MRI techniques, and is straightforward and easy to implement. However, Chen's method sacrifices the preparation pulse for shorter acquisition time which could significantly reduce the image contrast (figure 6.2 and figure 6.3), increasing the difficulty to depict myocardial infarction. Compared to their method, our method has two clear improvements:

1. Our method is flexible as a post-processing technique. Using our method, it is possible to produce cine late contrast enhanced MR images from previous scans.
2. Our method integrates information from cine MRI and late contrast enhanced MRI to produce a late enhanced cine sequence. As a result, the output shows the best features of cine MRI images, as well as the optimum contrast and therefore infarct depiction of late enhancement.

Our method therefore appears promising as an improved viability assessment tool.

Chapter 7
Extensive Studies

In the previous chapters, we introduced a cardiac function and viability assessment method using image registration and late contrast enhanced MRI. In this chapter we will further investigate the application of the image registration algorithm in cardiac MRI studies including non-linear cardiac ejection fraction, myocardial perfusion and the distensibility and pulse wave velocity of the aorta. These studies involve a common difficulty, that of contour definition. In this chapter we will describe how image registration could be a solution for contour definition.

7.1 The extensive studies

Late contrast enhanced MRI is one of the major tools for cardiac function and viability study in Glasgow Cardiac MR Unit (GCMRU, http://www.glasgowcmr.com). Cardiac cine MRI is performed on each patient or volunteer. Cardiac parameters such as left ventricle volume and ejection fraction are extracted from the cine MR images. Besides

In order to show up differences in myocardial perfusion, pharmacological stress is achieved using adenosine. This increases the blood supply to normal myocardium by 2-3 times by causing smooth muscle relaxation in the coronary arteries via the adenosine A2a receptors. This process is impaired in coronary artery disease with endothelial dysfunction as there is little or no increase in flow in these arteries, increasing the difference in perfusion between normal and ischaemic myocardium.

Ease of analysis of these images is vital for this technique to become an acceptable test of myocardial perfusion. At the present time the majority of the analysis of these images is performed qualitatively and semi-quantitatively. The qualitative assessment is an eye-ball assessment of the uptake of gadolinium on an MRI workstation. However, the mainstay of semi-quantitative analysis involves the creation of a signal intensity over time curve for selected regions of interest (ROI) in the myocardium and in the left ventricular cavity (also known as the arterial input function). Areas of reduced perfusion can be identified as the time to achieve peak signal intensity is prolonged and does not achieve as high a peak signal intensity as areas of normal myocardium. We can also measure from these curves the contrast enhancement ratio, the myocardial to left ventricle upslope index, the upslope integral ratio and the myocardial perfusion reserve index (MPRI).

In GCMRU, perfusion imaging is obtained in 3 slices of the myocardium per heart beat. Each of these slices is analysed every cardiac cycle for 50 cycles as we watch the perfusion of gadolinium into the LV myocardium. It is therefore imperative that there is no change in the position of the heart between cardiac cycles in order to ensure that we have an accurate signal intensity curve. Motion is minimised by triggering the images on each R wave of the electrocardiograph and by asking patients to hold their breath throughout the scan. Many of the patients are on rate limiting medications such as beta-blockers or calcium channel blockers and do not have much of a tachycardia despite adenosine stress. In such patients, 50 cardiac cycles may require a breath hold of almost a minute. They should then be adequately rate controlled with a resting pulse of between 50-60 beats per minute. For many of the patients who are elderly, this is therefore an impossible task and motion due to breathing is inevitable. A further problem necessitating motion correction is in patients with frequent ectopic beats leading to differences in myocardial thickening and therefore position. In order to create our signal intensity curves, we have to manually align each of the images (3 slices in total and 50 images per slice) at both stress and rest, which equates to a total of 300 images which is exceptionally time-consuming and makes the analysis cumbersome and impractical. This study aims to apply a semi-automatic solution to this problem of motion to ensure the analysis of perfusion MRI images.

Image registration has been widely involved in the automatic motion correction in cardiac perfusion study using MRI technology (Delzescaux et al., 2003; Dornier et al., 2003; Fenchel et al., 2004; Slomka et al., 2004). An image is selected from the first-pass perfusion sequence as the reference. The reference image should show clear anatomical structures of the myocardium. The reference image is then registered with other images in the sequence producing disparity maps or motion fields. These disparity maps or motion fields could be used to digitally warp the images in the perfusion sequence to match the reference image. Mutual information is often used as the similarity measurement of the image registration algorithm because of its immunity to the variety of the pixel intensity. If the image registration algorithm is robust and accurate, the warped images would be identical to the reference image in term of the shapes. The motion artifacts can therefore be compensated. The cardiac contours are defined on the reference image manually and then copied to the other images. Mean pixel intensities of regions are calculated to establish the perfusion curves over time.

This method establishes the perfusion curve using warped images. The warping algorithm may have changed the original pixel intensity as interpolation is often involved. The accuracy of the perfusion curve cannot be guaranteed. In this study, we attempt to keep the original image data by trying to track the cardiac contours instead of building a set of perfusion images with identical shapes. The method will be introduced in section 7.3.

7.1.2 Aortic Stiffness

There has been much interest recently in the relationship between arterial stiffness and cardiovascular disease, including hypertension and increased left ventricular mass (Blacher et al., 1999; London et al., 2001). Arterial stiffness may be measured using a variety of invasive and noninvasive methods. MRI has been used to demonstrate the inverse relationship between aortic distensibility and age, that aortic distensibility is reduced in hypertensive patients and that arterial compliance is reduced in patients with coronary artery disease but increased in athletes (Mackenzie et al., 2002). Using ultrafast MRI technology, aortic motion can be captured over time. Aortic contours are defined on each of the aortic images. The maximum and minimum aortic area can therefore be computed. The aortic distensibility is evaluated by:

$$distensibilty = Area_{\max} / Area_{\min}$$

In recent years, pulse wave velocity (PWV) is increasingly used to identify patients at increased cardiovascular risk (Mackenzie et al., 2002). According to the Moens-Korteweg equation (Nichols et al., 1998), the PWV, which is related to the square root of

the elasticity modulus, rises in stiffer arteries. The elastic properties of the aorta and central arteries are important determinants of cardiovascular coupling, and the PWV measured along the aortic pathway appears to be most clinically relevant. Arterial stiffening occurs normally with aging (Rogers et al., 2001) but also correlates with the prevalence of atherosclerosis.

PWV is the speed at which the forward pressure is transmitted from the aorta through the vascular tree. The more rigid the wall of the artery, the faster the wave moves. A commonly used method is to take two simultaneous Doppler flow tracings at the aortic arch and the femoral artery in the groin with a Doppler unit. The Doppler flow tracing identifies the arrival of the arterial pulse. The time blood flow travels from aortic arch and femoral artery can therefore be calculated by:

$$\Delta t = t_{aorticArch} - t_{femoralArtery}$$

where $t_{\text{aorticArch}}$ is the time when the arterial pulse reaches the aortic arch, $t_{\text{femoralArtery}}$ is the time when the arterial pulse reaches the femoral artery. The distance $\Delta dist$ travelled by the blood flow is measured over the body surface as the distance between the two recording sites. A simple equation is used to calculate PWV:

$$pwv = \Delta dist / \Delta t$$

MRI appears to be a robust tool for PWV measurement. The physical principle of PWV measurement using MRI has been discussed in chapter 3. MRI reveals the aorta from

both short axis and long axis views (figure 7.1a). The length of the aortic pathway can be measured either manually or automatically (Gao & Patrick et al., 2004). Cross-sectional phase contrast MRI (PCMRI), which was discussed in chapter 3, measures the velocity of blood flow (figure 7.1b) at specified regions based on accumulated phase shifts of the blood signal as it flows in the direction of a magnetic field gradient which is applied with opposite slopes, generating time-velocity curves. A progressive time-delay in arrival of the velocity wave results in a rightward shift of each curve.

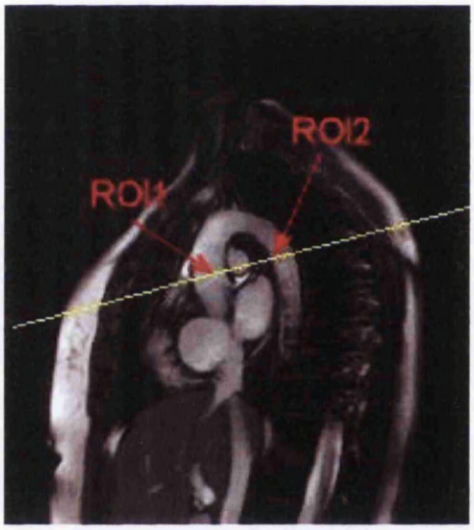

(a)

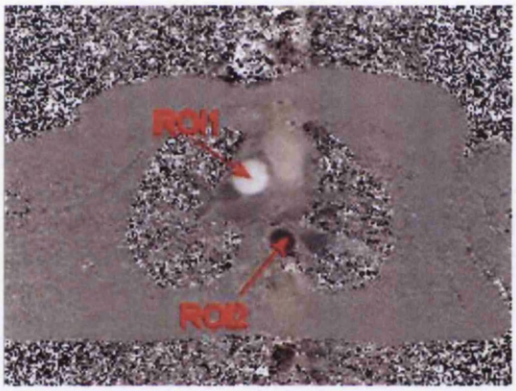

(b)

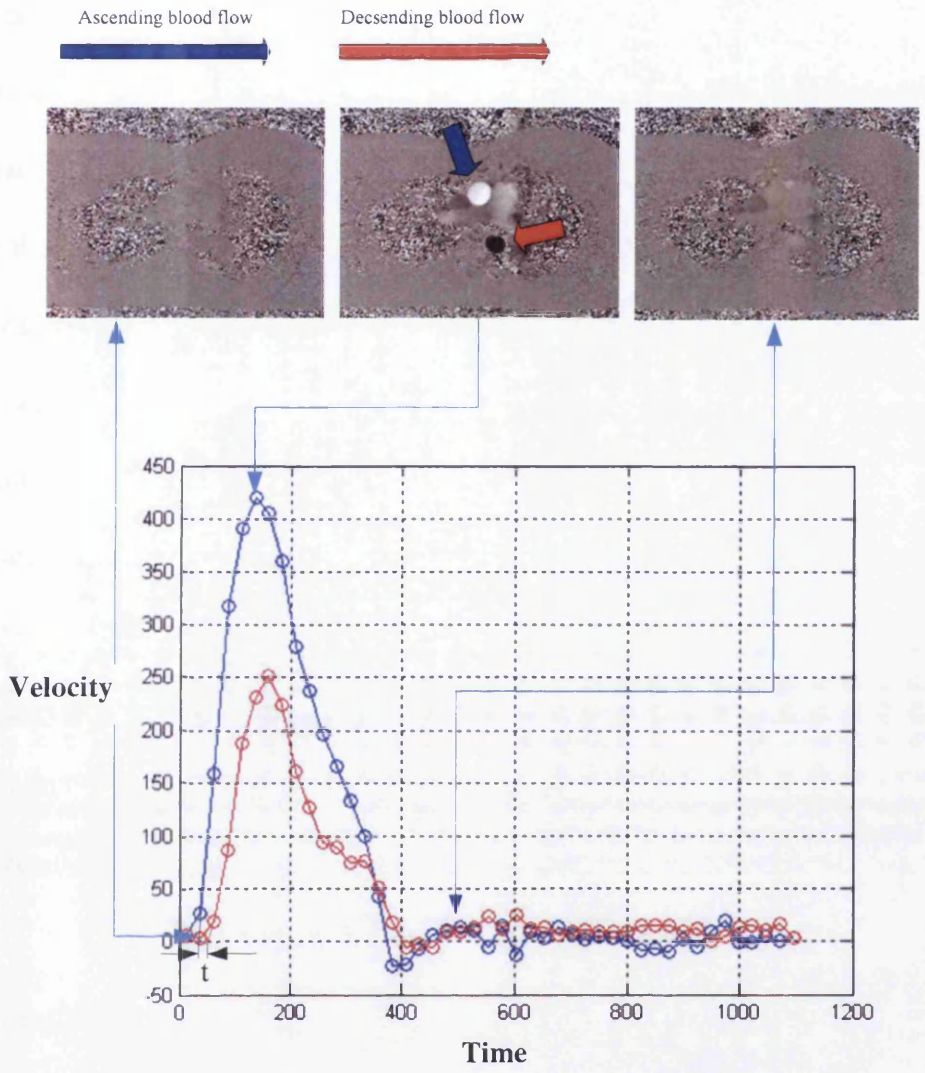

(c)

Figure 7.1 Image (a) reveals aorta from the long axis view. Flow image (b) is projected from the long axis aortic image, intersecting aorta at ROI1 and ROI2. The distance between ROI1 and ROI2 along aorta can be measured manually. Aorta contours were defined on the short axis aortic image and then projected to the flow images. Mean pixel intensities inside the aortic contours were calculated to form two flow curves (c). For each flow curve, the steepest section of the upstroke portion is extrapolated or interpolated to have an intersection point, t_i with the horizontal axis where flow = 0. The time delay between two flow curves is calculated by $t_2 - t_1$.

At present, there are two major methods to calculate the time delay using PCMRI. In the first method, the two velocity curves are normalised to have the same peak. Then the location of the best cross-correlation of two partial upstroke curves was used to estimate the time delay (Roger et al., 2001). Alternatively, the time delay can be calculated using a so called "foot to foot" method (Vulliemoz et al., 2002). For each flow curve, the steepest section of the upstroke portion is extrapolated or interpolated to have an intersection point, t_i with the horizontal axis where *flow velocity* = *0*. The time delay between two flow curves is calculated by:

$$\Delta t = t_{i+1} - t_i$$

In the Glasgow Cardiac MR Unit, we chose the foot to foot method as our pilot study showed that it produced more stable results compared to the first method described above, especially for the study on elderly subjects.

Normally the time delay t is from 20 to 40 milliseconds for a healthy volunteer and could be less than 10 milliseconds for a patient or elderly person with stiff aorta. Although our pilot study has showed that PWV measured using MRI has good correlation with aortic distensibility, we realise the measurement errors cannot be neglected as the time resolution is limited by the PCMRI capability at present. However, PWV measurement shows a new application of MRI technology. With future improvements in both hardware and software, and further clinical study, we believe the measure of PWV using MRI

could be a strong candidate for the status of "gold standard". In this study, we did not intend to improve the hardware capability of PCMRI.

In order to produce the velocity curves, aortic contours are defined on each image in the cross-section aortic cine sequences. The contours are then projected to the corresponding PCMRI sequence. Mean pixel intensities inside aortic contours are calculated to produce the flow curves over time. Normally, a PCMRI sequence contains more than 40 images. For each image, at least two contours (the ascending aorta and the descending aorta) are required to be defined in order to calculate the time delay. At present, manual contour definition is used in most of the studies. Undoubtedly, an automatic or semi-automatic contouring algorithm could significantly reduce the study time as well as the subjective errors.

7.2 Contours definition

Cardiac contours definition is involved in most cardiac MRI studies. In most of the clinical studies, cardiac contours are defined manually due to the lack of an efficient and reliable automatic contour definition algorithm. However, manual contour definition is tedious, time consuming and subjective. For many years, scientists and researchers have

been trying to invent an automatic method which could satisfy the clinical requirements. Many methods have been proposed in recent decades. Active contour models or "snakes" are amongst the most widely used algorithms (Rueckert et al., 1997). Generally, the "snakes" are computer generated curves that move within the images to find object boundaries. The "snakes" algorithm was proposed by Kass and his colleagues in 1988, and since then has been used in computer vision and image analysis to detect and locate objects, and to describe the shapes. In recent years, "snake" algorithms have been applied to the studies of medical images such as tumour detection and cardiac function analysis.

Mathematically, a "snake" is defined as an energy function E_{snake}. If the snake has the best fit with an object's contour, the energy function should return a minimum value. The function E_{snake} has two components, the internal spline energy caused by stretching and bending and the image energy. In some literature, the snake function has one more component, the constraint energy, which is imposed by the users to either achieve a more accurate result or reduce the computational complexity. The energy function of snake is defined as equation 7.1:

$$E_{snake} = \int_0^1 (E_{\text{int}ernal} V(s) + E_{image} V(s) + E_{constra\text{int}} V(s)) ds \qquad 7.1$$

The internal energy and the image energy are defined as equation 7.2 and 7.3.

$$E_{internal} = \alpha(s)\left|\frac{dv}{ds}\right|^2 + \beta(s)\left|\frac{dv}{ds}\right|^2 \qquad 7.2$$

$\alpha(s)$ and $\beta(s)$ are two parameters which control the shape of the curve. $\alpha(s)$ is the measure of elasticity while $\beta(s)$ controls the stiffness.

$$E_{image} = w_1 I(x, y) + w_2 \left|\nabla I(x, y)\right|^2 \qquad 7.3$$

where w is the weighted function. $\boldsymbol{I}$ is the pixel intensity of the input image.

The constraint energy is determined by external constraints. Normally, this energy is defined by users. It may come from higher knowledge about the images in question.

To search the contour in an image, the users mark several control points. The initial contour is interpolated from these points using a spline algorithm. An evolution of the curve is then carried out to adjust the curve toward the object boundary following the mathematical constraints as described in the equations 7.1 ~ 7.3.

The "snake" algorithm was plagued by two key problems since its invention in 1988. These problems are that snakes cannot move toward objects that are too far away and that snakes cannot move into boundary concavities or indentations. Although many solutions have been proposed, these problems are not completely solved.

Another popular automatic contouring algorithm is active shape model (Cootes et al., 1994). The active shape model represents a parametric deformable model where a statistical model of the global shape variation from a training set is built. This model, called the point distribution model (PDM), is then used to fit a model (or template) to unseen occurrences of the object earlier annotated in the training set. The PDM could be constructed using various algorithms such as principal component analysis. The active shape model and the "snake" algorithm can be used together to provide a better result. Similar to PDM, Kenji and his colleagues proposed a training-set based cardiac contour definition algorithm using a neural network (Suzuki et al., 2004). Their algorithm consisted of three steps: 1) detect "subjective edges" from the training set by use of neural network; 2) find the rough contour using a low-pass filter, for example, a Canny filter (Morris, 2003); 3) find the contour based on the "subjective edges" detected in the first step and the rough contours extracted from the second step.

Although many different methods and satisfactory results were reported in past years, the "gold standard" at present is still the most basic manual contour definition because:

1. The requirements are always high because the results must be clinically safe.
2. Unlike natural images, the quality medical image can be easily affected by a variety of reasons such as partial volume effects, weak contrast and unwanted patient motion.

3. An algorithm must be efficient to be practically useful however the accuracy must be maintained.

In Glasgow Cardiac MR Unit, we tested the original "snake" algorithm implemented in Intel's open computer vision library (OpenCV). A large degree of contour mis-definition was observed in almost every test sequence. The comparison will be discussed in the experimental results.

In such situations, the semi-automatic methods are of considerable benefit. We extended the work discussed in previous chapters, to a semi-automatic contour definition algorithm. The method was tested on images captured by three different MRI sequence types, including cardiac cine MRI, first-pass perfusion MRI and aortic cine MRI. Although our method is not fully automatic, the experiment showed our method significantly reduced the analysis time and the experimental results suggested the defined contours could be reliable and clinically useful.

7.3 Semi-automatic contour definition

The demand for an automatic contour definition algorithm is constantly increasing because contours are often required to be defined on multiple studies for an MRI study.

For example, in myocardial perfusion study, clinicians are generally required to define cardiac contours for more than 300 images. However, these images often display the same object from the same angle over time. There is a strong correlation between the images, which could be investigated for the contour definition.

Our method defines contours for time-series MRI images by exploiting correlations between the images. Similar to the "snake" algorithm, our method can also be explained as an energy function. The difference is that we used motion energy to replace the image energy in the "snakes" energy function.

In a reference image, several control points are defined manually along the object boundaries. The contours are initialised by cubic-interpolating these control points. We assume the initial contours can describe the object boundaries exactly.

For a cine sequence, a reference image is selected. The object contours are manually defined by a set of control points (figure 7.2). MSSM registers the reference image with other images within the same sequence, building a set of motion maps. The control points will find their new locations in the other cine images using the motion maps. New contours can therefore be built using a cubic spline interpolation.

In this study, we applied the algorithm to cardiac cine images primarily. With cardiac contours defined in each image in the cine MR sequence, we can extend the study into new areas such as non-linear ejection fraction, cardiac filling rate. In addition, we will make preliminary tests of the algorithm on the aortic cine images and the first-pass perfusion images for forthcoming projects.

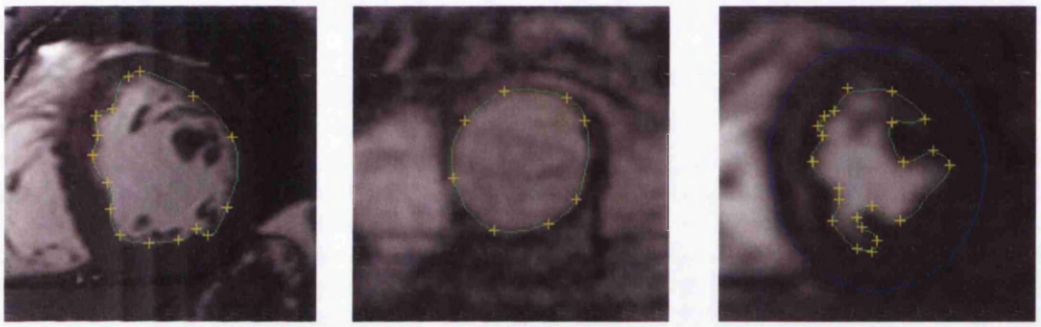

(a) (b) (c)

Figure 7.2 Given a set of control points, smooth curves can be built by cubic interpolation of the control points. The cross marks show the control points. (a). Cardiac CINE image; (b). Aortic CINE image; (c). First-pass perfusion image.

7.4 Experimental results

7.4.1 Data acquisition

The image sequences for testing were selected from the database of GCMRU, which contains more than 2000 MRI studies. All the MRI studies were performed on a Siemens Sonata 1.5 Tesla MRI system. Cardiac cine sequences were acquired using ultrafast pulse sequence TrueFISP, 8mm slice thickness with 2mm gap, TR/TE = 3.2/1.6 ms, with a matrix size of 208 x 256. Breath-hold is required during data acquisition. For the study of pulse wave velocity, the PCMRI uses a velocity sensitivity of ±150cm/s, slice thickness of 6mm, TR/TE of 16 / 3.1 ms and a flip angle of 15 degrees. At least one angle transverse image sequence for each study is acquired to reveal both ascending and descending aorta. For the study of first-pass perfusion MRI, images were acquired from 3 slices with a slice thickness of 10mm using an ECG gated turboFLASH sequence. The three slices were acquired from the base, middle and the apex of the heart. The matrix size is 78x128, FOV = 400mm.

7.4.2 Cardiac cine MRI images

Thirty-four cardiac cine MRI scans were selected from the database of GCMRU. The subjects included 20 normal volunteers and 14 heart failure patients. For each short axis stack, we defined a reference image. In the reference image, the cardiac contours were defined manually as the initial contours. Papillary muscles were not covered by the

contours. The MSSM algorithm exploits the correlation between the reference image and the other images, producing vector maps estimating the motion of each pixel on the reference image. Therefore, the control points are propagated from the reference image to the other images using the vector maps.

For each slice, the end diastolic image and the end systolic image were decided manually. The reference images were chosen between the end diastolic image and the end systolic image. Mean left ventricular end diastolic volume in each of the scans was measured by planimetry (manual/proposed)=177.31/176.55ml, p=0.48. The left ventricular end systolic volume (manual/proposed) =82.10/84.32ml, p=0.33. The basal slice, mid-slice and apical slice of a random example are shown in figure 7.3. Figure 7.4 shows the endocardial volume change in a cardiac cycle of the example shown in figure 7.3. Figure 7.5 shows a solution to calculate the non-linear ejection fraction. Overall data from the healthy volunteers and patients are shown in figure 7.6 and 7.8. Figure 7.7 and 7.9 presented the error distribution.

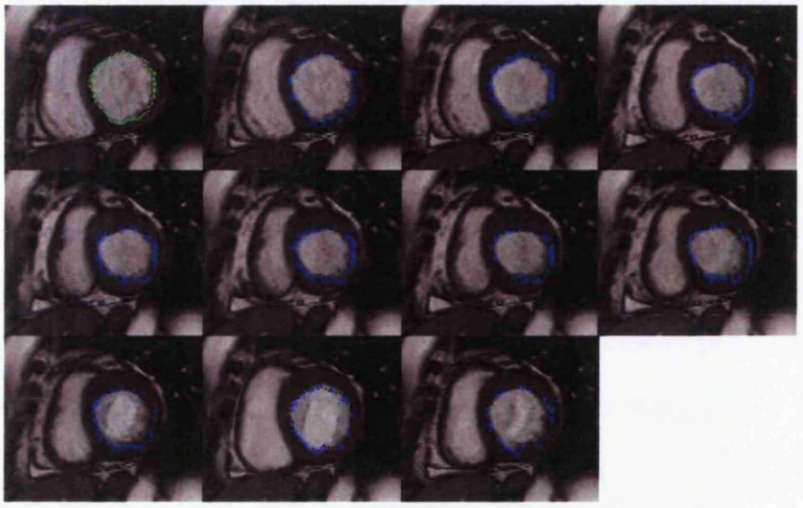

(a)

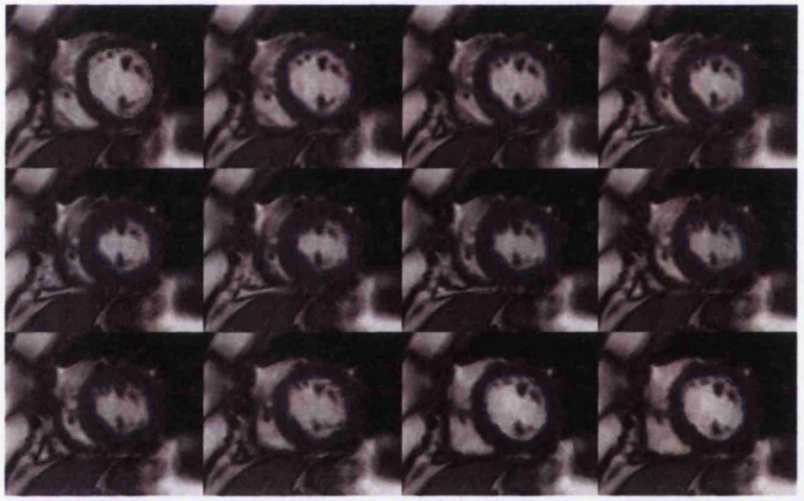

(b)

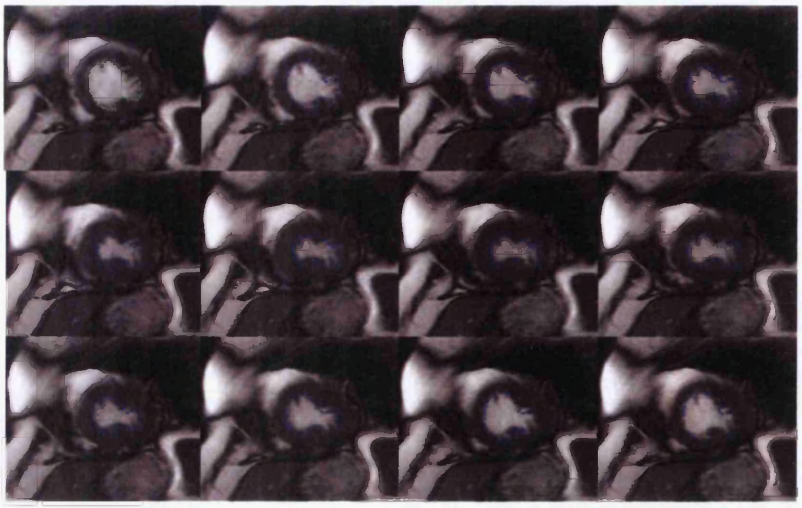

(c)

Figure 7.3 Cardiac contours were defined semi-automatically. In the first image, the contour was defined manually. Then the contour was propagated to the other images. (a). a basal slice; (b). a mid-slice; (c) an apical slice.

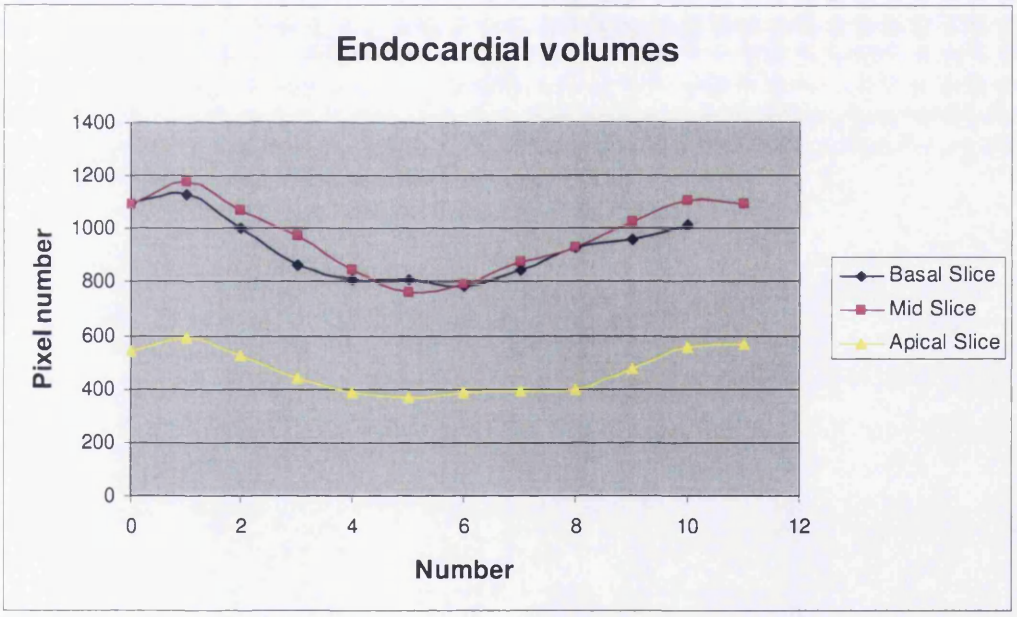

Figure 7.4 The volume change of the left ventricle endocardium in a cardiac cycle. Cardiac contours were defined on each cine MR image semi-automatically.

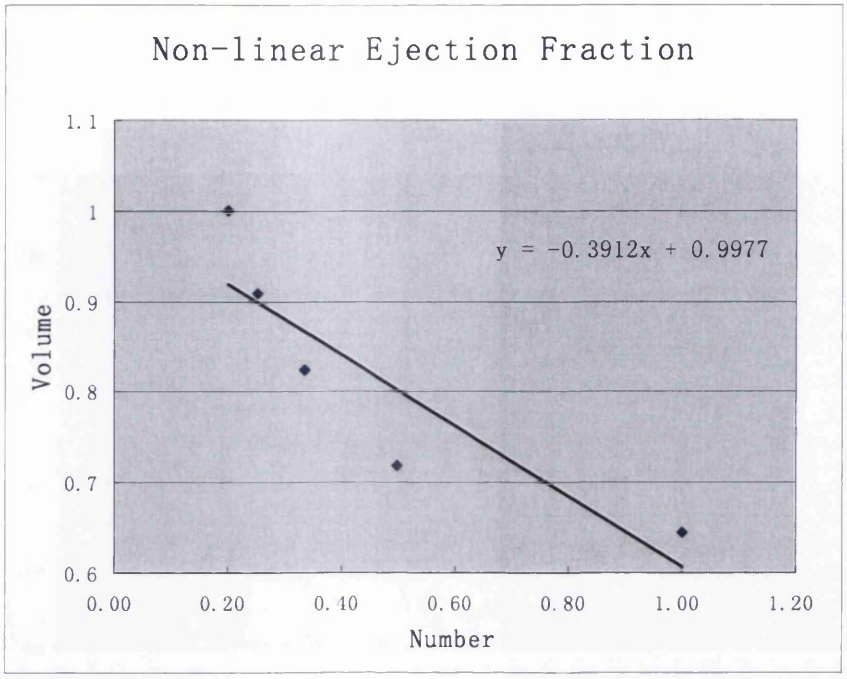

Figure 7.5 Non-linear calculation[1] of the ejection fraction. Cardiac contours were defined in each image in a cine MR sequence. The end-diastole and the end systole were located based on the endocardial volume. The data were re-sampled to have N points. In this example, N = 5. Both the volume (y axis) and the image number (x axis) were stretched to have the maxima of 1. A straight line is calculated to best fit the data and the slope can therefore be considered as the ejection fraction. The same method can also be applied to non-linear filling rate study.

[1] **Non-linear ejection fraction is also referred to as ejection rate.**

20 Healthy volunteers

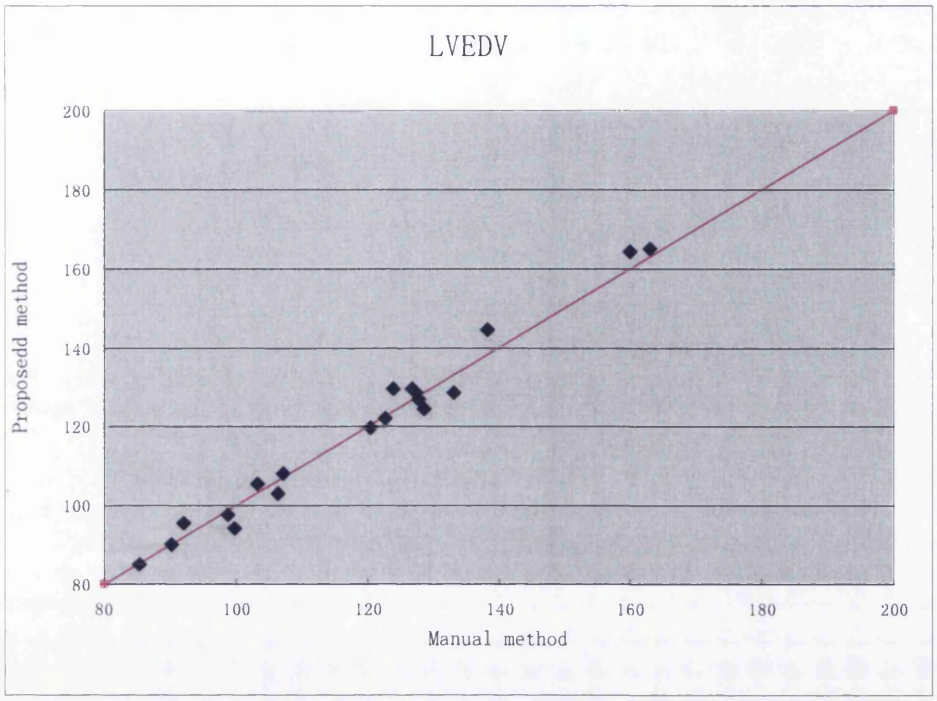

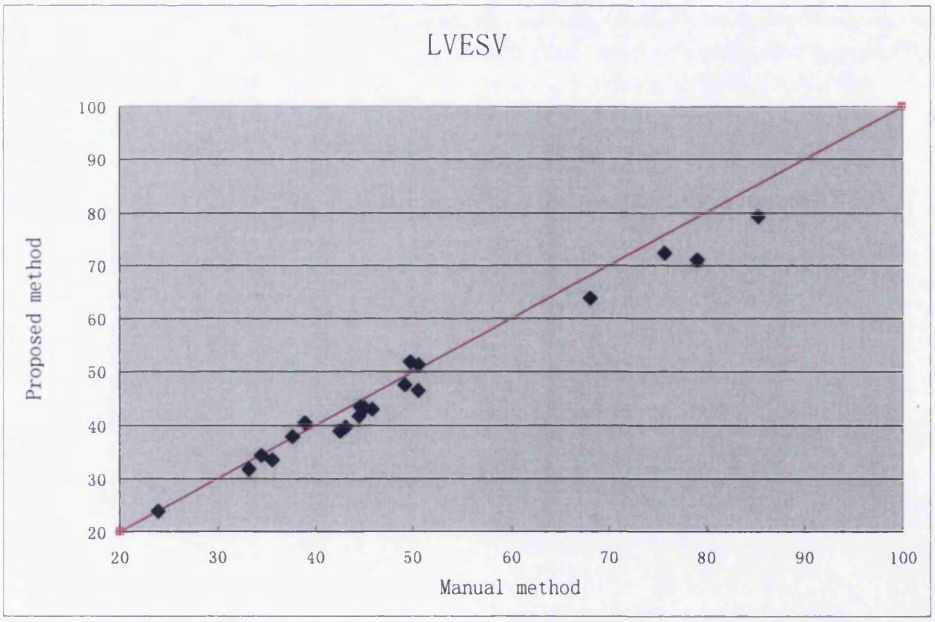

Figure 7.6 Comparison between the proposed contour definition method and the manual contour definition method. The initial contour was defined manually on the image between the diastolic and systolic image.

20 Healthy volunteers

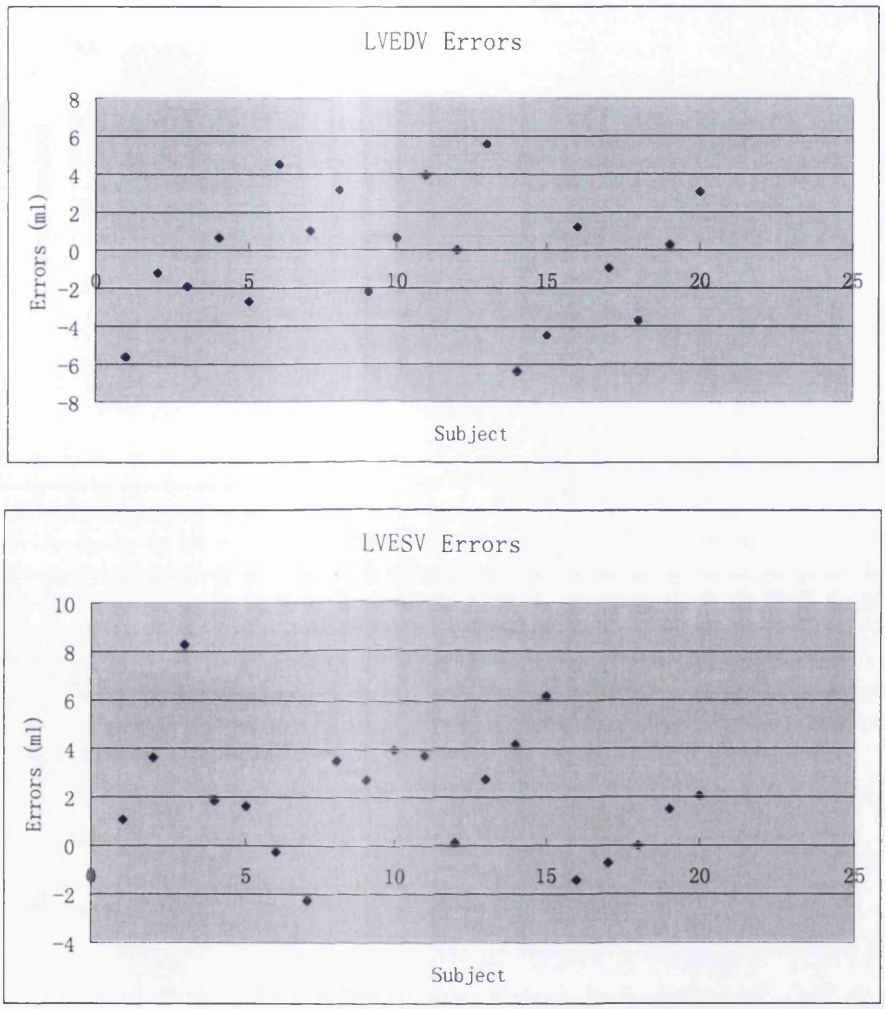

Figure 7.7 Comparison between the proposed contour definition method and the manual contour definition method. The figure presents the data of 20 healthy volunteers

14 patients

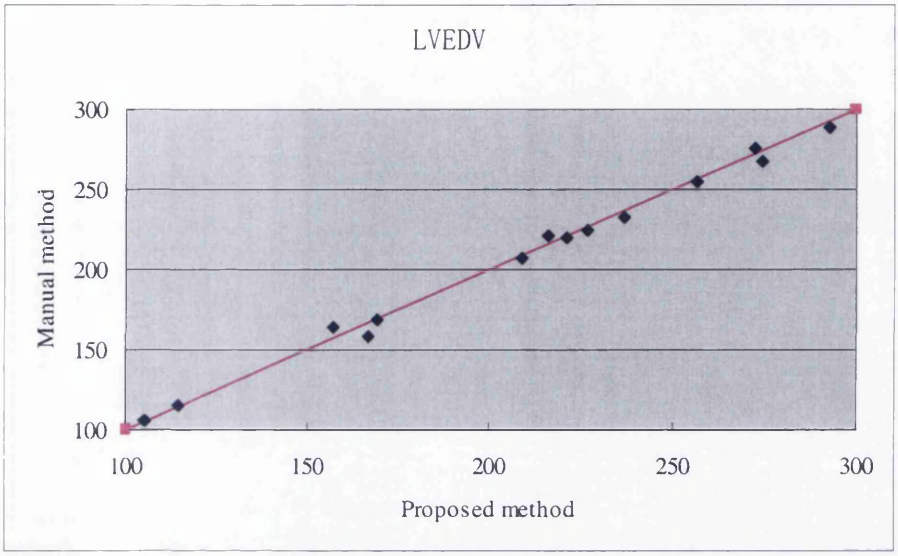

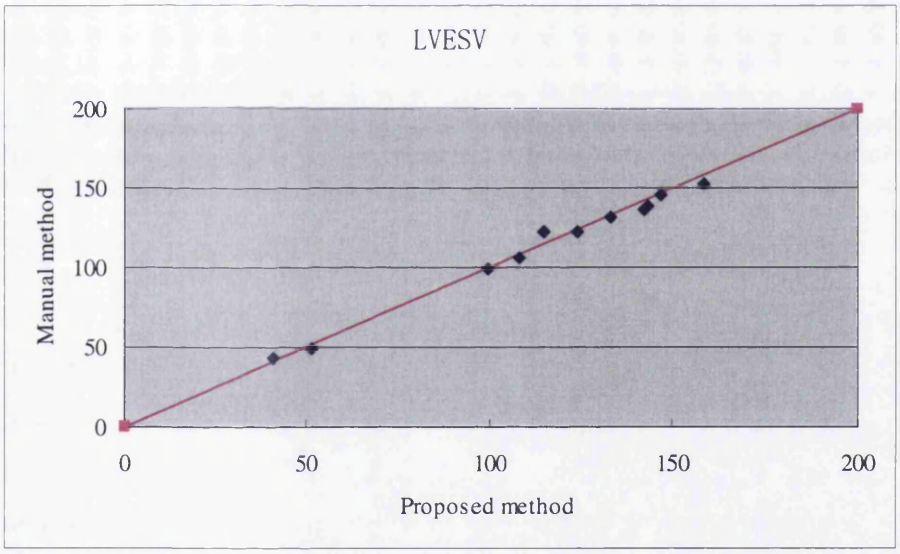

Figure 7.8 Comparison between the proposed contour definition method and the manual contour definition method. The initial contour was defined manually on the image between the diastolic and systolic image.

14 patients

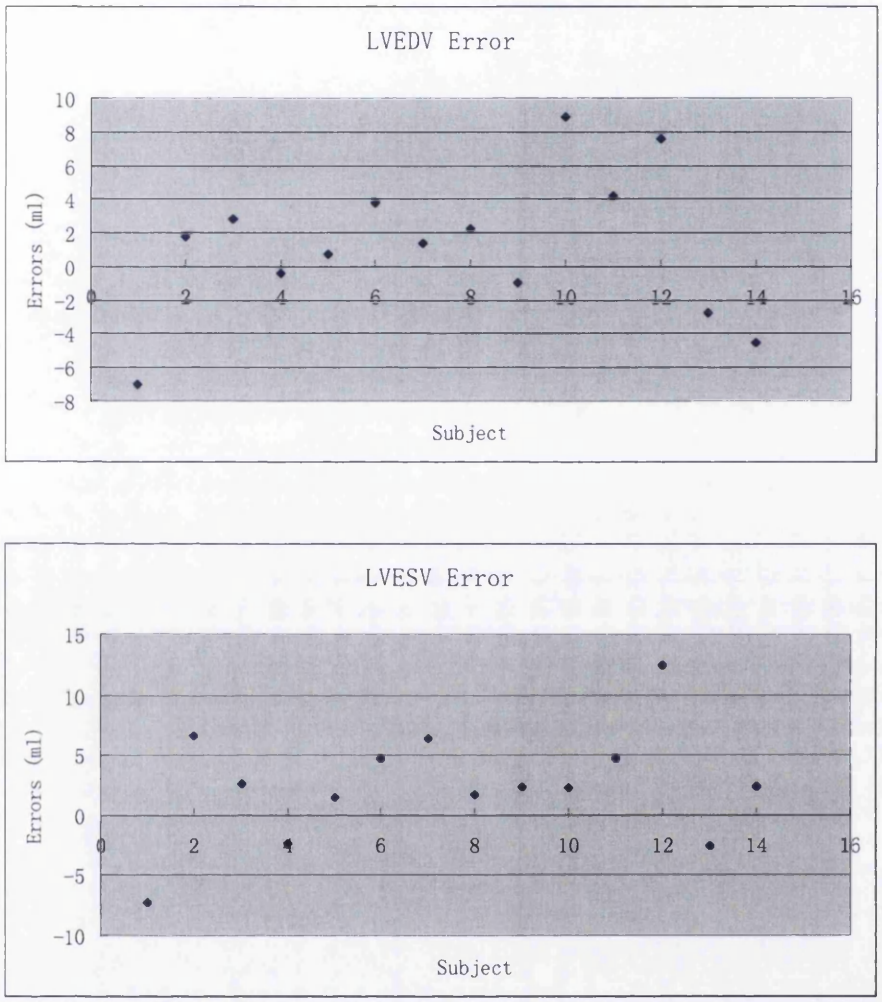

Figure 7.9 Comparison between the proposed contour definition method and the manual contour definition method. The figure presents the data of 20 healthy volunteers

In addition, we compare results produced from our algorithm with the results produced from the 'snake' algorithm. Five cardiac cine MR scans were selected from the database of GCMRU. All five scans were acquired from healthy volunteers. For each cine MRI scan, a reference image was selected between the end diastole and the end systole. Cardiac contours were defined manually on the reference image. The snake algorithm was used to find the contours on both the diastolic image and the systolic image. Table 7.1 and table 7.2 summarised the comparison results.

Subjects	Manual definition (ml)	Snake (ml)	The proposed algorithm (ml)
1	160.31	132.90	165.21
2	136.24	122.66	142.54
3	130.73	139.57	128.77
4	169.81	147.33	166.63
5	124.11	108.02	120.05

Table 7.1 Comparison of LVEDV between the proposed algorithm and the snake algorithm

Subjects	Manual definition (ml)	Snake (ml)	The proposed algorithm (ml)
1	50.10	78.05	52.03
2	68.25	82.31	62.12
3	76.86	84.57	71.43
4	46.39	57.55	42.61
5	38.88	63.24	40.29

Table 7.1 Comparison of LVESV between the proposed algorithm and the snake algorithm

From the comparison, our proposed algorithm is clearly superior to the snake algorithm.

7.4.3 First-pass perfusion MR images

Before the MRI contrast agent Gd-DTPA reaches the heart, no MRI signals are acquired. Pixel intensities in the areas of myocardium and the blood pool are relatively close, which make it very difficult to define the contours of myocardium. The Gd-DTPA reaches the right ventricle as the blood flow returns to the left ventricle from the right atria. Following the blood flow, the Gd-DTPA is pumped to the lung for oxygenation and then goes back to the left ventricle from the left atria. In a first-pass perfusion sequence, the right ventricle becomes visible in the first instance and then the left ventricle. In our experiment, the reference image was selected to be the first image in which the left ventricle boundary can be clearly observed. The left ventricular contours including the endocardium and the epicardium were defined manually.

A characteristic of the first-pass perfusion MR image is the constant change of the pixel intensity. As discussed in chapter 6, the MSSM algorithm matches the images in spatial frequency space, where the focus is on the shape. The variation of the pixel intensity cannot significantly affect the registration results. However, the cardiac boundary could be blurred in the first-pass perfusion image as the pixel intensity becomes too high. The blurring of the cardiac contours increases the difficulty of the registration. In addition, the low resolution of the first-pass perfusion imaging may cause extra difficulty for the

matching. From the pilot study discussed in chapter 6, we concluded that the "n to one" matching strategy has the best overall performance. In this study, we registered perfusion MR images with the selected reference image using the "n to one" matching strategy. The reference image was selected to be the middle image in the sequence where clear left ventricle structure could be observed. Initially, the n was set to 5. However, it could be manually adjusted to achieve a better result if the output is unsatisfactory.

To test our method, 10 first-pass perfusion MRI scans were selected from the database of GCMRU. Figures 7.10 and 7.11 show partial results from a randomly selected test, suggesting our algorithm can significantly reduce the motion artifacts in the first-pass perfusion study.

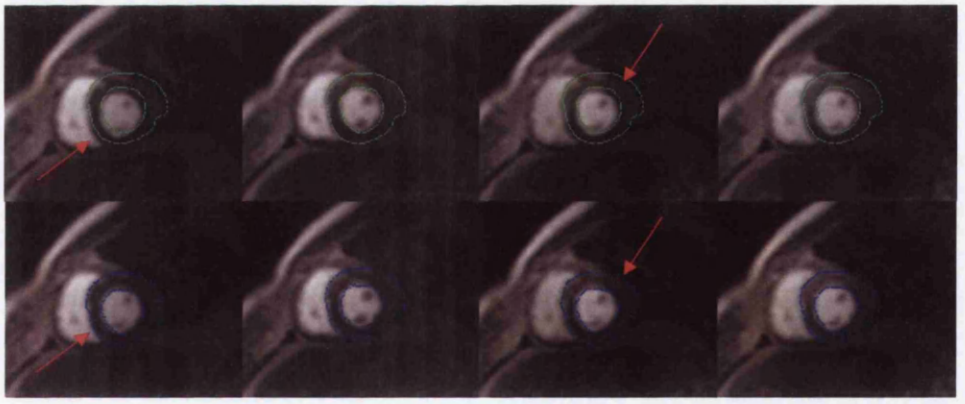

Figure 7.10 The 16^{th}, 17^{th}, 18^{th} and 19^{th} image of a base slice first pass perfusion sequence. In the upper row, cardiac contours were copied from those defined on the reference image (the 20^{th}). The 16^{th} and 18^{th} suffers serious motion artefacts. In the lower row, the contours were defined using our algorithm. The arrows point to the areas where significant motion artefacts were corrected.

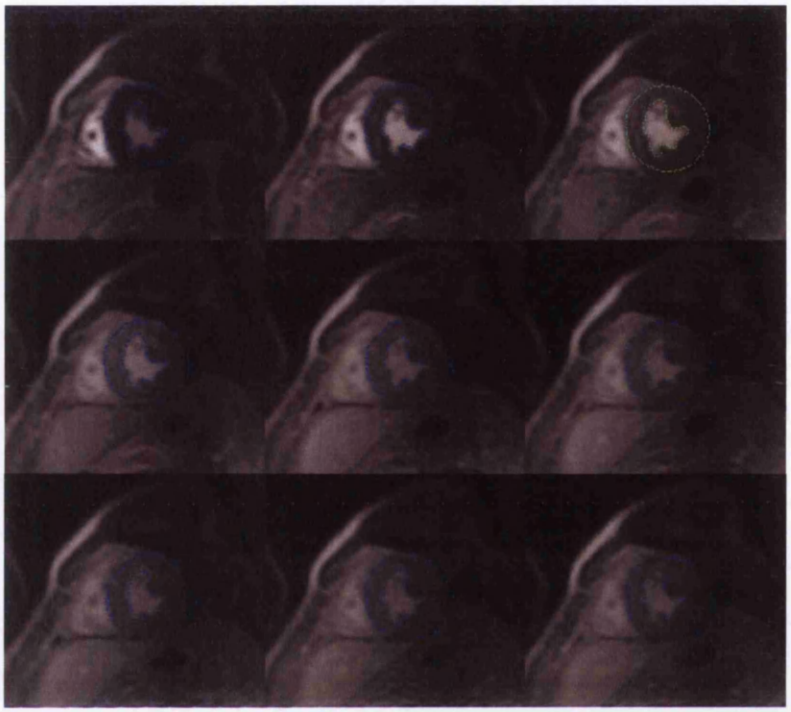

Figure 7.11 A middle slice of first-pass perfusion MR images. The images are the 10^{th}, 15^{th}, 20^{th}, 25^{th}, 30^{th}, 35^{th}, 40^{th}, 45^{th} and 49^{th} image in the sequence. The 20^{th} image was selected as the reference image. Left ventricle contours were defined on the reference image and propagated to the rest of the sequence. No manual corrections were involved in the test.

The experimental results from the initial test on 10 first-pass perfusion sequences were visually assessed. The result of the definition for endocardium is satisfied even for those images where the endocardium is obscured by the blood pool. The contour definition for the epicardium is always challenging especially for the period when the contrast agent is passing through the heart. Mis-definition for the epicardium occurs in 17 images out of

the 500 images we tested (1 ~ 3 images for each first-pass perfusion sequence). Manual correction is required to correct the mis-registration.

7.4.4 Aortic cine MRI images

Two types of aortic MR images were involved in our study. The first type is the aortic cine MR image, which is generated using ultrafast MRI techniques such as Siemens TrueFISP and TurboFLASH. Ideally, aortic contours will be defined in each image in the sequence for the distensibility study. The second type of aortic MR image is the phase contrast MRI (PCMRI, see chapter 3). The PCMRI as a single pulse sequence produces two types of image simultaneously. One image sequence shows the encoded velocity maps over time. The other image sequence shows the anatomic details. Aortic contours are defined in each image of the anatomic sequence and then projected to the velocity maps. The average pixel intensity within the contours is calculated to build the pixel intensity curves. For both the distensiblity study and PWV study, the reference image is selected to be the image between diastole and systole. Aortic contours were defined manually on the reference image and the contours in other images can therefore be automatically produced. Generally, aortic motion is not as significant as cardiac wall

motion, and even the "all to one" matching strategy can produce satisfactory results (figures 7.11 and 7.12).

Initial experiment tested our algorithm on 10 studies selected from the database of GCMRU.

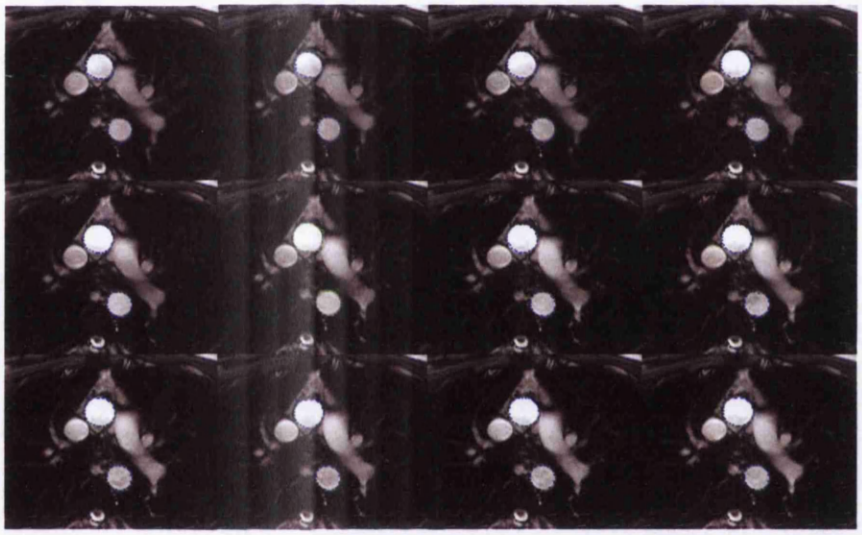

Figure 7.11 Aortic contours were defined in each frame of the aortic cine MRI sequence to study the aortic distensibility. The contours in the reference image (the 6^{th} image) were defined manually while others were defined automatically.

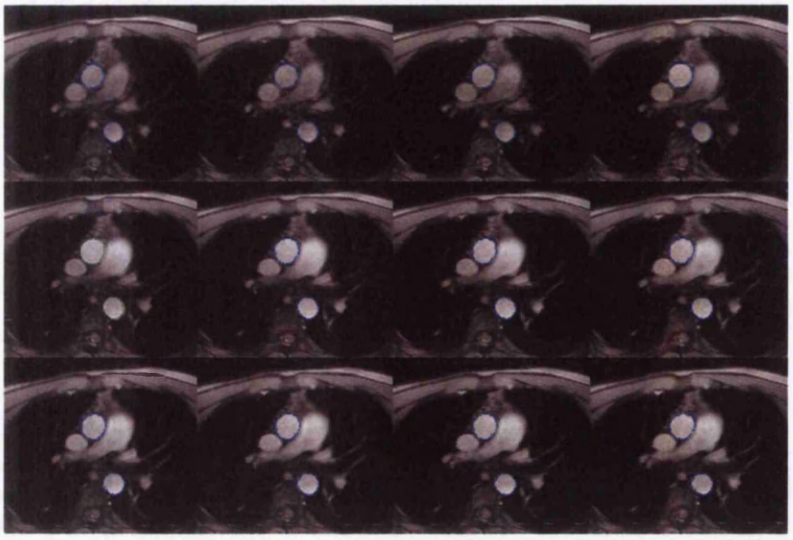

Figure 7.12 The reduced image quality PCMRI did not affect the performance of the semi-automatic contour definition algorithm.

Figures 7.11 and 7.12 show the contour definition result using our algorithm for an aortic cine sequence and a PCMRI sequence. For all 10 experiments, the quality of the contour definition is excellent. Although the image quality of the PCMRI images is not as high as the aortic cine images, the performance of our algorithm is equally satisfying. Potentially, our algorithm could improve the aortic study using MRI significantly.

7.5 Discussion

The automatic contour definition for cardiac MR images is difficult for many reasons, including the low image quality and the partial volume effect. Although many efforts

have been made in recent decades, no algorithm is used practically at present because of their unreliability. The method we discussed in this chapter appears to be a trade-off as a semi-automatic contour definition algorithm. The method was extended from a robust and efficient image registration algorithm and has been tested on cardiac cine MR images, first-pass perfusion MR images and two types of aortic MR images. For cine MR images, the experimental results shows no difference between the manual method and our method for the testing on 34 subjects. The experimental results for the first-pass perfusion MRI studies appear less promising than the cardiac cine MRI study because of the low image quality and resolution.

In the first-pass perfusion MRI study, MR contrast quickly disappears as Gd-DPTA passes the myocardium, which could severely affect the registration results. For this reason, the selection of the reference image is rather important. In this study, the reference image is chosen manually to ensure both left ventricle endocardium and myocardium can be clearly observed. The definition of endocardium is easier than the definition of epicardium because this outer boundary often hides in the background as the contrast fades away. On some occasions manual intervention is required to correct the mis-definition as the error which could be propagated to the definition in the next image.

The initial experiment suggests our algorithm could achieve the best results for aortic contour definition. Dilation and translation are equally significant during aortic systole. Our free-form sub-pixel level image registration algorithm appears to be a robust and efficient tool to detect those types of motion. No mis-definition was observed in the test on all the 10 subjects. Although the image quality of PCMRI is not as promising as aortic cine MRI, the contour definition for PCMRI is equally satisfied.

7.6 Conclusion

For the quantitative assessment of cardiac MR images, cardiac contours are often to be defined in multiple images. The demand for an automatic contour definition algorithm is constantly increasing. However, the design of a completely automatic contour definition algorithm is extraordinarily difficult due to the variation of the image quality and the strict requirements of the medical image assessment to be fit for their clinical purpose. We were attempting to find a compromise solution by introducing a semi-automatic contour definition algorithm. Our algorithm is specifically designed to define the contour for time-series MR images. An initial contour is required to be defined on a selected reference image. Our algorithm will exploit the correlation between images and deform the initial contour to find the target in the other images.

The algorithm was tested on cardiac cine MR images from 34 subjects including 20 healthy volunteers and 14 patients with heart failure. The experimental results show no difference between our method and the manual method, which is the "gold standard" at present. Five subjects were selected randomly from the 20 healthy volunteers. The "snake" algorithm was used to definite the cardiac contours for their cine MRI scans. Under the same conditions (same reference image, same initial contours), our algorithm shows better results in all five scans. We did not have the chance to compare our algorithm with other existing automatic contour definition algorithms such as the active shape model due to lack of implementation. The data we got so far suggest our algorithm could be a strong competitor to any existing algorithms.

The satisfactory performance suggests our algorithm could be used in more challenging areas such as the study of myocardial perfusion and aortic stiffness. We tested our algorithm on the first-pass perfusion MRI, aortic cine MRI and PCMRI preliminarily. The results for both aortic cine MRI and PCMRI are satisfactory. The contour definition for the first-pass perfusion MRI is slightly less promising. Visible errors occur occasionally in the definition of epicardium as the MR signals from myocardium are dwarfed in the background in some cases. Manual assistance is required to correct the mis-definition. Besides the occasional errors, our algorithm has shown great potential to

be an improved assessment tool for cardiac MR studies. With further investigation and evaluation, we believe our algorithm could be a competitive candidate for future clinical studies.

Chapter 8
Conclusion

MRI is a noninvasive imaging technique used primarily in medical settings to produce high quality images of the inside of the human body. As a young but quickly growing technology, MRI has attracted massive research on both hardware and software. At present, with carefully designed pulse sequences such as TrueFisp and TurboFlash MRI is able to produce high quality images within seconds. The fast MRI acquisition techniques are widely used in cardiovascular studies. During a cardiac cycle, cardiac cine images are acquired to reveal cardiac motion. Reduced cardiac motion indicates the existence of myocardial diseases such as myocardial infarction and hibernating myocardium. Recent studies suggest that 10 minutes after the injection of an MRI contrast agent such as Gd-DPTA, myocardial infarction can be observed in T1 weighted MR images as a contrast difference. Although the areas of contrast enhancement are not necessarily identical to areas of previous myocardial infarction, contrast enhanced MRI is playing an important role in the quantitative or semi-quantitative studies of myocardial infarction. At present, contrast enhanced images are studied in combination of its corresponding cine MR images to derive a cardiac viability score. The intention is to locate reversible hibernating myocardium using such a scoring system. However, the contrast enhanced image and cine images are not registered because of patient motion in the intervening

period. The resulting misregistration could introduce diagnostic errors. The objective of this work is to overcome such difficulties and produce an efficient and accurate software package for cardiac viability analysis. In this work, we developed an algorithmic method which produces what we called late enhanced cine images. The output of our method shows the best features of cine MR images along with the improved contrast of late enhancement.

The key of this method is an accurate, robust and efficient image registration algorithm, MSSM. MSSM extracts motion data from the cine MRI sequence. The motion data are used to digitally warp the static late contrast enhanced MR image. They can also be analysed regionally to locate myocardium with reduced wall motion. The cardiac viability score is produced by visual evaluation of wall motion abnormalities in combination with presence or absence of late enhancement. The experimental results show MSSM is an accurate, robust and efficient cardiac registration algorithm. There is no significant difference in left ventricle end diastolic volume and left ventricle end systolic volume between the original cine and late contrast enhanced images and the motion late enhanced images. The results strongly suggest that our method would be a reliable cardiac viability assessment tool.

Our method is not the only method currently existing which produces cine late contrast enhanced MR images. Chen and his colleagues proposed an alternative method in 2003.

Using their method, cine late contrast enhanced images can be generated directly from an MRI scanner. However, Chen's method sacrifices the preparation pulse for the short acquisition time. This significantly reduces the image contrast, thereby affecting its ability to depict myocardial infarction (figures 6.2 and 6.3). Compared to Chen's method, our method is more flexible. As a post image processing technique, we can even generate cine late contrast enhanced images from archives of previous scans. Most importantly, our method provides a better infarct visualization when compared to Chen's method. Technically, our method integrates information from cine MRI and late contrast enhanced MRI to produce a late enhanced cine sequence. As a result, the output shows the best features of cine MR images, as well as the optimum contrast and therefore infarct depiction of late enhancement. Results from Chen's method and our method were examined by the cardiologists in GCMRU. They concluded that our method could be an improved viability assessment tool.

Cardiac contour definition is one of the most frequency used method in cardiac MRI studies. In many of the studies, the contours need to be defined in the entire image sequence which is time consuming. In this study, we extended our work to a semi-automatic contour definition algorithm which is specifically designed for sequential contour definition. Similar to the well-known "snake" algorithm, in our method, initial cardiac contours are required to be defined on a selected reference image. The image registration algorithm will find the cardiac motion by matching the reference image with

the other images in the cardiac cine MRI sequence. The predefined cardiac contours could therefore be "stretched" to match the cardiac boundaries in other images.

This algorithm was tested on cardiac cine MR images from 34 subjects, including 20 healthy volunteers and 14 patients with myocardial infarction. The experimental results appear promising as no significant difference between our method and the manual contour definition was shown.

The "snake" algorithm is a widely recognised automatic contour definition method. To further evaluate the performance of our algorithm, we compared the performance of our technique with the "snake" algorithm. The "snake" algorithm we used is implemented in an Intel open source project, OpenCV (http://sourceforge.net/projects/opencvlibrary/). The initial contours, including endocardium and epicardium were defined manually on a reference image. Then the initial contours were deformed to the cardiac boundary of every image in the image sequence using our algorithm and the "snake" algorithm. Under the same condition (same reference image, same initial contour, without manual correction), our technique shows better results compared to the "snake" algorithm. The experimental data show heavy manual correction is needed for the use of the "snake" algorithm in practice while only small or no human intervention is required for the use of our algorithm. Therefore we can conclude that our method is better than the "snake" algorithm in the application of cardiac contour definition using MRI.

Besides the "snake" algorithm, several other automatic contour definition algorithms were proposed in recent years, including the active shape model and point distribution model. Due to a lack of implementation, we are not able to compare the performance of our algorithm with theirs. Based on the data we have so far, our algorithm could be a strong competitor for any existing algorithms. Evaluation of our technique will continue in future research.

Our algorithm was preliminarily tested on different MRI modalities, including the first-pass perfusion MRI and phase contrast MRI, both of which have played important roles in cardiac viability study. The successful application of the first-pass perfusion MRI reveals the ischaemic myocardium. The phase contrast MRI suggests the velocity of blood flow, indexing the aortic stiffness. Both the study of the first-pass perfusion MRI and phase contrast MRI require contour definition for the entire sequence.

The contour definition for the first-pass perfusion MRI and the phase contrast MRI is more challenging than for the cardiac cine MRI because of low image resolution and quality. Preliminary experiments indicate our method could produce reliable and clinically useful result with minor manual correction. Although it is a semi-automatic algorithm, the labour intensity and analysis time could still be significantly reduced. With further investigation and validation, we believe this could be an improved software

solution for cardiac MRI study.

It was reported that in 2003 there were approximately 10,000 MRI units worldwide, and approximately 75 million MRI scans performed per year. MRI technology is one of the hottest research topics at present. It is not to be doubted that MRI technology will remain a hot research topic in the future. MRI technology produces high quality images. The extraction of clinically useful data relies on successful application of computer aided methods, manipulated either manually or automatically.

In the past decade, research on automatic medical image analysis has attracted more and more attention, because of its clear advantages, including subjectivity and efficiency. In this work, modest achievements have been made and difficulties have been well recognised. Some problems are still remained unsolved. The research will continue.

Reference

Ablitt et al., 2004	Nicholas, A. Ablitt, Jianxin Gao, Jennifer Keegan, et al., "Predictive Cardiac Motion Modeling and Correction with Partial Least Squares Regression", IEEE Transactions on Medical Imaging, Vol. 23, No. 10, October 2004
Adelson et al., 1984	E. H. Adelson, C. H. Anderson, J. R. Bergen, P. J. Burt, J. M. Ogden, "Pyramid methods in image processing", RCA Engineer, 29-6, Nov/Dec 1984
Agostino et al., 2003	E. D.Agostino, J. Modersitzki, F. Maes, D. Vandermeulen, B. Fischer and P. Suetens, "Free-Form Registration Using Mutual Information and Curvature Regularization", Biomedical Image Registration, Springer-Verlag Heidelberg, June 2003, pp11-20
Aamer & Masataka, 2002	Aamer Aziz and Masataka Uetani, "Introduction to MRI - History", 2002
Anderson & Becker, 1980	Robert H. Anderson and Anton E. Becker, "Cardiac Anatomy: An intergrated text and colour atlas", Gower Medical Publishing ltd., 1980
Ardeshir, 1986	Ardeshir Goshtasby, Piecewise linear mapping functions for image registration, Pattern Recognition, Vol 19, pp. 459-466, 1986.
Ardeshir, 1988	Ardeshir Goshtasby, Image registration by local approximation methods, Image and Vision Computing, Vol 6, p. 255-261, 1988.
Atkinson et al., 1990	D. J. Atkinson, D. Burstein, R. R. Edelman, et al., "First-pass cardiac perfusion: evaluation with ultrafast MR Imaging", Radiology, Vol. 174, pp. 757 – 762, 1990
Axel & Dougherty, 1989	L. Axel and L Dougherty, "MR Imaging of Motion with Spatial Modulation of Magnetization", Radiology, Vol. 171, pp. 841-845, 1989
Ball, 1995	Stephen G. Ball, "Myocardial Infarction: From trials to practice", Wrightson Biomedical Publishing Ltd, 1995

Bernstein et al., 2004	Matt A. Bernstern, Kevin F. King and Xiaohong Joe Zhou, "Handbook of MRI pulse sequences", Elsevier Academic Press, 2004
Bezdek et al., 1993	J. C. Bezdek, L. O. Hall, and L. P. Clarke, "Review of MR image segmentation techniques using pattern recognition," *Medical Physics*, vol. 20, no. 4, p. 1033-1048, 1993.
Blacher et al., 1999	Jacques Blacher, Alain P. Guerin, Bruno Pannier, "Impact of Aortic Stiffness on Survival in End-Stage Renal Disease", Circulation, 99:2434-2439, 1999
Bloch et al., 1946	Bloch F. Hansen et al., "Nuclear Induction", Physical Review, 69:127, 1946
Braunwald & Rutherford, 1986	Braunwald E, Rutherford JD, "Reversible ischemic left ventricular dysfunction: evidence for the "hibernating myocardium", J Am Coll Cardiol, 8: 1467-70, 1986
Brown, 1992	Lisa G. Brown, "A surrey of image registration techniques", ACM Computing Surveys, Vol. 24, Issue 4, pp. 325 – 376, December 1992
Cerqueria et al., 2002	Manuel D. Cerqueria, Neil J. Weissman, Vasken Dilsizian, et al., "Standardized Myocardial Segmentation and Nomenclature for Tomographic Imaging of the Heart: A Statement for Healthcare Professionals From Cardiac Imaging Committee of the Council on Clinical Cardiology of the American Heart Association", Circulation, Vol. 105, pp. 539-542, 2002
Chandrashekara et al, 2002	R Chandrashekara, RH Mohiaddin, D Rueckert, "Analysis of myocardial motion in tagged MR images using nonrigid image registration", Proceedings of Medical Image understanding and analysis (MIUA), Portsmouth, pp. 1 – 4, 2002
Chen et al., 2003	Q. Chen, P. Storey, P. V. Prasad, "Simultaneous Assessment of Myocardial Function and Viability", Proceeding of International Society of Magnetic Resonance in Medicine, pp. 1610, 2003
Cho et al., 1993	Zang-Hee Cho, Joie P. Jones and Manbir Sinch, "Foundations of Medical Imaging", John Wiley & Sons, 1993
Cideciyan et al., 1992	A. V. Cideciyan, S. G. Jocobson, C. M. Kemp, et al., "Registration of high resolution image of the retina", Proceeding of SPIE: Medical Imaging VI: Image Processing, Vol. 1622, pp. 310 – 322, 1992

Clarke et al, 1995	L. P. Clarke, R. P. Velthuizen, M. A. Camacho, J. J. Heine, M. Vaidyanathan, L. O. Hall, R. W. Thatcher, and M. L. Silbiger, "MRI segmentation: Methods and applications," *Magnetic Resonance Imaging*, vol. 13, no. 3, p. 343-368, 1995.
Cockshott et al., 2003	W. P. Cockshott, Y. Tao, G. Gao, et. al., "Confocal Microscopic Image Sequence Compression Using Vector Quantization and 3D Pyramids" SCANNING -The Journal of Scanning Microscopies, Vol. 25 (5), pp. 247-256, Sept. 2003
Cockshott & Tao, 2003	W. P. Cockshott, Y. Tao, G. Gao, C. Daly, "Microscopic Volumetric Image Data Compression Using Vector Quantization and 3D Pyramid" Picture Coding Symposium 2003 (PCS'03), pp. 119-124, Saint-Malo, France, April 2003
Cohen & Weisskoff, 1991	Cohen MS and Weisskoff RM, "Ultra-fast imaging", Magnetic Resonance Imaging, 9(1):1-37, 1991
Collignon et al., 1995	A. Collignon, F. Maes, D. Delaere, et al., "Automatic multi-modality image registration based on information theory", Information processing in medical imaging, Y. Bizais et al. Eds. Amsterdam, the Netherland: Kluwer, pp. 263 – 274, 1995
Coversano et al., 1996	Conversano A, Walsh JF, Geltman EM, Perez JE, Bergmann SR, Gropler RJ, "Delineation of myocardial stunning and hibernating myocardium by PET in advanced coronary artery disease", American Heart Journal, 131: 440-50, 1996
Cootes et al., 1994	T. F. Cootes, A. Hill, C. J. Taylor, et al., "The Use of Active Shape Models for Locating Structures in Medical Imaging", Image and Vision Computing, Vol. 12, No. 6, pp355 – 366, July 1994
Cullen et al., 1999	J. H. S. Cullen, M. A. Horsfield, C. R. Reek, et al., "A Myocardial Perfusion Reserve Index in Humans Using First-pass Contrast-Enhanced Magnetic Resonance Imaging", Journal of American College of Cardiology, Vol. 33, No. 5, 1999
Damadian, 1971	Damadian RV, "Tumor detection by nuclear magnetic resonance", Science, 171: 1151-1153, 1971

Delzescaux et al., 2003	Thierry Delzescaux, Frederique Frouin, Alain De Cesare, "Using an Adaptive Semiautomatic Self-Evaluated Registration Technique to Analyze MRI Data for Myocardial Perfusion Assessment", Journal of Magnetic Resonance Imaging, Vol. 18, pp. 681 – 690, 2003
Dhawan, 2003	Atam P. Dhawan, "Medical Image Analysis", IEEE press series in Biomedical Engineering, 2003
Dornier et al., 2003	C. Dornier, M. K. Ivancevic, P. Thevenaz, "Accurate MR cardiac perfusion analysis by using a multiresolution B-splines registration algorithm", Proceeding of International Society of Magnetic Resonance in Medicine, pp700, 2003
Dougherty et al., 1999	Lawrence Dougherty, Jane C. Asmuth, Aaron S. Blom, et al., "Validation of an Optical Flow Method for Tag Displacement Estimation", IEEE Transaction on Medical Imaging, Vol. 18, No. 4, April 1999
Elsen et al., 1993	Petra A. van den Elsen, Evert-Jan D. Pol and Max A. Viergever, "Medical Imaging Matching: A Review with Classification", IEEE Engineering in Medicine and Biology, pp. 26 – 39, March 1993
Epstein et al., 2002	Frederick H. Epstein, James F. London, Dana C. Peters, et al., "Multislice First-Pass Perfusion MRI: Validation in a Model of Myocardial Infarction", Magnetic Resonance in Medicine, 47: 4820491, 2002
Eusemann et al., 2001	Christian D. Eusemann, Stefan Mohlenkamp, Erik L. Ritman, et.al., "3D Quantitative Visualization of Altered LV Wall Thickening Dynamics Caused by Coronary Microembolization", Proceeding of SPIE – Medical Imaging, pp. 100 – 107, 2001
Fenchel et al., 04	Michael Fenchel, Ulrich Kramer, Uwe Helber, et. al, "Semiquantitative Assessment of Myocardial Perfusion Using Magnetic Resonance Imaging: Evaluation of Appropriate Thresholds and Segmentation Models", Investigative Radiology, Vol. 39, No. 9, 2004
Frahm et al., 1986	Frahm J., Haase A. and Matthaei D., "Rapid NMR imaging of dynamic processes using the FLASH technique", Journal of Magnetic Resonance, 3:321-327, 1986
Freire et al., 2002	Freire, L.; Roche, A.; Mangin, J.-F, "What is the best similarity measure for motion correction in fMRI time series?", IEEE transaction on medical imaging, vol21, issue 5, May 2002

Fieno et al., 1999	Kim RJ, Fieno DS, Parrish TB, et al, "Relationship of MRI delayed contrast enhancement to irreversible injury, infarct age, and contractile function", Circulation, Vol 100, pp1992 – 2002, 1999
Hornak, 2002	Joseph P. Hornak, "The basics of MRI", http://www.cis.rit.edu/htbooks/mri/, April, 2002
Gao et al., 2004	Gang Gao, Paul Cockshott, Bjoern Groenning, Thomas Martin, "Cardiac Imaging", International Patent Application, PCT/GB03/004831, Department of Computing Science, Glasgow University
Gao & Patrick et al., 2004	Gang Gao, Patrick Mark, Paul Cockshott, et. al., "Measurement of pulse wave velocity using MRI", IEEE EMBC, San Francisco, 2004
Gao & Cockshott et al., 2004	Gang Gao, Paul Cockshott, Thomas Martin, et. al., "A novel method for viability assessment by cinematographic and late contrast enhanced MRI images", ISMRM'04 Kyoto, Japan, May 2004
Gao & Martin et al., 2004	Gang Gao, Paul Cockshott, Thomas Martin, et. al., "A novel method for viability assessment by cinematographic and late contrast enhanced MRI images", Journal of Cardiac Magnetic Resonance, Feb. 2004
Garot, 2004	Jerome Garot, "The study of diastole by tagged MRI: Are we nearly there yet?", European heart journal, Vol. 25, No. 16, August, 2004
Gatehouse et al., 2004	Peter Gatehouse, Andrew Elkington, Nicholas Ablitt, et al., "Accurate Assessment of the Arterial Input Function during High-dose Myocardial Perfusion Cardiovascular Magnetic Resoance", Journal of Magnetic Resonance Imaging, 20:39-45, 2004
Glockner et al., 2003	J. F. Glockner, D. W. Stanley, A. B. Robbins, et al., "Real Time Myocardial Delayed Enhancement: Initial Clinical Evalution", Proceeding of International Society of Magnetic Resonance in Medicine, pp. 1608, 2003
Gomes et al., 1999	Jonas Gomes, "Warping and morphing of graphical objects", Morgan Kaufmann Publishers, 1999
Gyngell, 1988	Gyngell M. L., "The application of steady state free precession imaging in rapid 2D FT NMR imaging: FAST and CE-FAST pulse sequence", Magnetic Resonance in Medicine, 6:415-419, 1988

Higgins et al., 2002	Charles B. Higgins, Albert De Roos, "Cardiovascular MRI and MRA", Lippincott Williams & WilKins, pp. 51 – 69, 2002
Ibrahim et al., 2003	T. Ibrahim, S. G. Nekolla, M. Hornke, et al., "Quantification of Infarct-size using Contrast Enhanced Magnetic Resonance Imaging in Acute Myocardial Infarction", Proceeding of International Society of Magnetic Resonance in Medicine, pp. 1607, 2003
Itskovich et al., 2001	Vitalli V. Itskovich, Kenneth A. Kraft, Ding-Yu Fei, "Rapid Aortic Wave Velocity Measurement with MR Imaging", Radiology, Vol. 219, pp. 551 – 557, 2001
Jezzard et al., 2001	Peter Jezzard, Paul M. Matthews, Stephen M. Smith, "Functional MRI: an introduction to methods", Oxford university press, 2001
Jin et al., 2000	Joseph Zhengping Jin, Bryan Niblett, Colin Urquhart, "Improved method and apparatus for 3D imaging", International Patent Application, PCT/GB99/03584, Department of Computing Science, Glasgow University
Julian, 1988	Desmond G. Julian, "Cardiology 5th Ed.", Bailliere Tindall, 1988
Klein et al., 2002	Christoph Klein, Stephan G. Nekolla, Frank M. Bengel, et al., "Assessment of Myocardial Viability with Contrast-Enhanced Magnetic Resonance Imaging: Comparison with Positron Emisson Tomography", Circulation, Vol. 105, pp. 162 – 167, 2002
Kolipaka et al., 2003	A. Kolipaka, G. P. Chatzimavroudis, R. D. White, et al., "Automatic Quantification of Non-Viable Myocardium in Delayed Enhancement Magnetic Resonance Images", Proceeding of International Society of Magnetic Resonance in Medicine, pp. 1603, 2003
Kraitchman et al., 1995	Dara L. Kraitchman, Alistair A. Young, Cheng-Ning Chang, et al., "Semi-Automatic Tracking of Mycoardial Motion in MR Tagged Images", IEEE Transactions on Medical Imaging, Vol. 14, No. 3, September 1995
Kvitting et al., 2004	John-Peder Escobar Kvitting, Tino Ebbers, Jan Engvall, et al., "Three Directional Myocardial Motion Assess Using 3D Phase Contrast MRI", Journal of Cardiovascular Magnetic Resonance, Vol. 6, No. 3, pp. 627 – 636, 2004

Laddis et al., 2001	Laddis T., Manning W. J., Danias P. G., "Cardiac MRI for assessment of myocardial perfusion: Current status and future perspectives", Journal of Nuclear Cardiology, Vol 8(2), pp207-214, 2001
Lauerma et al., 1997	K. Lauerma, K. S. Virtanen, L.M. Sipila, et al., "Multislice MRI in Assessment of myocardial perfusion in patients with single-vessel proximal left anterior descending coronary artery disease before and after revascularization", Cirrulation, Vol. 96, pp. 2859 – 2867, 1997
Lauterbur, 1973	Lauterbur PC, "Image formation by induced local interaction: examples of employing nuclear resonance", Nature, 242: 190-191, 1973
London et al., 2001	Gerard M. London, Jacques Blacher, Bruno Pannier, et al., "Arterial Wave Reflections and Survival in End-Stage Renal Failure", Hypertension, 38:434-438, 2001
London et al., 1996	G. M. London, A.P. Guerin, S.J. Marchais, et al, "Cardiac and Arterial Interaction in end-stage renal disease", Kidney Int. 50:600-608, 1996
Mackenzie et al., 2002	I.S. Mackenzie, I.B. Wilkinson and J.P. Cockcroft, "Assessment of Arterial Stiffness in Clinical Practice", Q J Med, 95:67-74 2002
Maes et al., 1997	Frederik Maes, Andre Collignon, Dirk Vandermeulen, et al, "Multimodality Image registration by Maximization of Mutual Information", IEEE Transactions on Medical Imaging, Vol.16, No. 2, April 1997
Mahrholdt et al., 2003	Heiko Mahrholdt, Anja Wagner, Michele Parker, Matthias Regenfus, David S. Fieno, Robert O. Bonow, Raymond J. Kim and Robert M. Judd, "Relationship of contractile function to transmural extend of infarction in patients with chronic coronary artery disease", Journal of America College Cardiology, 42(3), pp. 505 – 512, August, 2003
Makela et al., 2002	Timo Makela, Patrick Clarysse, Outi Sipila, et al, "A Review of Cardiac Image Registration Methods", IEEE Transactions on Medical Imaging, Vol. 21, No. 9, September, 2002
Manning et al., 2002	Warren J. Manning and Dudley J. Pennel, "Cardiovascular Magnetic Resonance", Churchill Livingstone, pp. 53 – 62, 2002.

Mansfield et al., 1973	Mansfield P, Grannell PK, Garroway AN, Stalker DC., "Multi-pulse line narrowing experiments: NMR "diffraction" in solids?" Proceedings. First Specialized Colloque Ampère. Cracow, Poland. 1973. 16-27.
Marshall et al., 2000	Marshall,S.J. Siebert,J.P., "Human Body 3D imaging by speckle texture projection photogrammetry", Sensor Review. Volume 20, No 3, pp.218-226, 2000
Morris, 2003	Tim Morris, "Computer vision and image processing", Basingstoke : Palgrave Macmillan, 2004
Moshfeghi et al., 1994	Mehran Moshfeghi, Surendra Ranganath, and Ken Nawyn, "Three-dimensional Elastic Matching of Volumes", IEEE transactions on image processing, Vol 3, No. 2, March 1994
Meyer et al., 1996	Francois G. Meyer, R. Todd Constable, Albert J. Sinusas, "Tracking Myocardial Deformation Using Phase Contrast MR Velocity Fields: A Stochastic Approch", IEEE Transactions on Medical Imaging, Vol. 15, No. 4, August 1996
McLeish et al., 2002	Kate McLeish, Derek L. G. Hill, David Atkinson, Jane M. Blackall, and Reza Razavi, "A Study of the Motion and Deformation of the Heart Due to Respiration", IEEE transaction on medical imaging, vol21, No. 09, September 2002
Mitchell, 1999	Donald G. Mitchell, "MRI principles", W.B. Saunders Company, 1999
Nagel et al., 2003	E. Nagel, C. Klein, I. Paetsch, et al., "Magnetic Resonance perfusion measurement for the noninvasive detection of coronary artery disease", Circulation, Vol. 108, pp. 432 – 437, 2003
Nichols et al., 1998	Nichols WW, O'Rourke MF, "McDonald's Blood Flow in Arteries: Theoretical, Experimental and Clinical Principles (4th edition)", London, UK, Edward Arnold, pp243–283 and 347–395, 1998
Nielsen et al., 2004	Gitte Nielsen, Thomas Fritz-Hansen, Christina G. Dirks, et al., "Evaluation of Heart Perfusion in Patients with Acute Myocardial Infarction Using Dynamic Contrast-Enhanced Magnetic Resonance Imaging", Journal of Magnetic Resonance Imaging, 20:403-410, 2004
Park et al., 1996	Jinah Park, Dimitri Metaxas and Leon Axel, "Analysis of Left Ventricle Wall Motion Based on Volumetric Deformable models and MRI-SPAMM", Medical Imaging Analysis, Vol. 1, No. 1, pp. 53 – 71, 1996

Pelc et al, 1991	Pelc N. J., Herfkens R. J., Shimakawa A., et al., "Phase contrast CINE magnetic resonance imaging ", Magnetic Resonance Quarterly 4, 229-254, 1991
Pelizzari et al., 1989	C. A. Pelizzari, G. T. Y. Chen, D. R. Spelbring, et al., "Accurate three-dimensional registration of CT, PET and/or MR images of the brain", Journal of Computer Assisted Tomography, Vol. 13, No. 1, pp. 20 – 26, 1989
Penney et al., 1998	Graeme P. Penney, Jurgen Weese, John A. Little, Paul Desmedt, Derek L. G. Hill and David J. Hawkes, "A comparison of Similarity Measures for Use in 2D-3D Medical Image Registration", IEEE transaction of medical imaging, vol 17, No. 4, August, 1998
Penzkofer et al., 1999	H. Penzkofer, B. J. Wintersperger, A. Knez, et al., "Assessment of myocardial perfusion using multisection first-pass MRI and color-coded parameter map: a comparison to 99mTc Sesta MIBI SPECT and systolic myocardial wall thickening analysis", Magnetic Resonance Imaging, Vol. 17(2), pp. 161 – 170, February 1999
Periaswamy et al., 2003	Senthil Periaswamy and Hanny Farid, "Elastic Registration in the Presence of Intensity Variations", IEEE Transaction on Medical Imaging, Vol. 22, No. 7, July 2003
Pluim et al., 2003	Josien P. W. Pluim, J. Michael Fitzpatrick, "Image Registration", IEEE Transactions on Medical Imaging, Vol. 22, No. 11, November 2003
Purcell et al., 1946	Purcell EM, Torrey HC et al., "Resonance Absorption by Nuclear Magnetic Moments in a Solid", Physical Review 69:37, 1946
Raghavendra, et al., 2004	Raghavendra Chandrashekara, Raad H. Mohiaddin, and Daniel Rueckert, "Analysis of 3-D Myocardial Motion in Tagged MR Images Using Nonrigid Image Registration", IEEE transaction on medical imaging, vol23, issue 10, October 2004
Rao et al., 2004	A. Rao, R. Chandrashekara, G. I. Sanchez-Ortiz, R. Mohiaddin, et al, "Spatial transformation of motion and deformation fields using nonrigid registration", IEEE transaction on medical imaging, vol24, No.9, September 2004
Ritter et al., 1999	Nicola Ritter, Robyn Owens, James Cooper, et al., "Registration of Stereo and Temporal Images of the Retina", IEEE Transactions of Medical Imaging, Vol. 18, No. 5, May 1999

Rogers et al., 2001	Walter J. Rogers, Yong-Lin Hu, Douglas Coast, et al., "Age-Associated Changes in Regional Aortic Pulse Wave Velocity", Journal of American College of Cardiology, Vol 38 No. 4, 2001
Rohlfing et al., 2003	Rohlfing, T.; Maurer, C.R., Jr.; Bluemke, D.A.; Jacobs, M.A., "Volume preserving non-rigid registration of MR breast imaging using free-form deformation with incompressibility constrain", IEEE transaction on medical imaging, vol22, issue 6, June 2003
Rueckert, et al., 1997	D. Rueckert, P. Burger, S. M. Forbat, et al., "Automatic Tracking of the Aorta in Cardiovascular MR Images Using Deformable Models", IEEE Transactions on Medical Imaging, Vol. 16, No. 5, October 1997
Rueckert et al., 1999	D. Rueckert, L. I. Sonoda, C. Hayes, D. L. G. Hill, M. O. Leach, and D. J. Hawkes, Nonrigid Registration Using Free-Form Deformations: Application to Breast MR Images", IEEE transaction on medical imaging, vol18, issue 8, August 1999
Saadi et al., 2000	Al Saadi N., Nagel E., Gross M., et al., "Noninvasive detection of myocardial ischaemia from perfusion reserve based on cardiovascular magnetic resonance", Circulation, Vol.101(12), pp1379-1383, 28 March 2000
Schnabel et al., 2003	Julia A. Schnabel, Christine Tanner, Andy D. Castellano-Smith, et al., "Validation of Nonrigid Image Registratioin Using Finite-Element methods: Application to Breast MR Images", IEEE Transaction on Medical Imaging, Vol. 22, No. 2, February 2003
Shannon, 1948	C. E. Shannon, "A mathematical theory of communication", Bell System Technical Journal, Vol. 27, pp. 379-423, July, 1948
SimplyPhysics, 2002	Simply Physics, "Basic Nuclear Magnetic Resonance", http://www.simplyphysics.com/page2_1.html, April, 2002
Slomka et al., 2004	Piotr J. Slomka, Hidetaka Nishina, Daniel S. Berman, et al., "Motion-Frozen" Display and Quantification of Myocardial Perfusion", The Journal of Nuclear Medicine, Vol. 45, No. 7, July 2004

Siebert et al., 1994	Siebert, J. P. and Urquhart, C. W., "C3D: a Novel Vision-Based 3-D Data Acquisition System", Proc. Mona Lisa European Workshop, Combined Real and Synthetic Image Processing for Broadcast and Video Production, Hamburg, Germany, 1994
Simonetti et al., 2001	Orlando P. Simonetti, Raymond J. Kim, David S. Fieno, et al., "An improved MR imaging technique for the visualization of myocardial infarction", Radiology, 218: 215-223, 2001
Solomon et al., 1990	Eldra Pearl Solomon, Richard R. Schmidt, Peter James Adragna, "Human anatomy and physiology (2nd Edition)", Saunders College Publishing, 1990
Studholme et al., 1995	C. Studholme, D. L. G. Hill and D. J. Hawkes, "Multiresolution voxel similarity measures for MR-PET registration", Information Processing in Medical Imaging, Y. Bizais et al., Eds. Amsterdam, the Netherland: Kluwer, pp. 287 – 298, 1995
Suinesiaputra et al., 2003	A. Suinesiaputra, Luc Florack, J. J. M. Westenberg, et al., "Optic Flow Computation from Cardiac MR Tagging Using a Multiscale Differential Method: A Comparative Study with Velocity-Encoded MRI", pp. 483 – 490, Proceeding of MICCAI, Montreal, Canada, 2003
Suzuki et al., 2004	Kenji Suzuki, Isao Horiba, Noboru Sugie, et al., "Extraction of Left Ventricular Contours From Left Ventriculograms by Means of a Neural Edge Detector", IEEE Transactions on Medical Imaging, Vol. 23, No. 3, March 2004
Thevenaz et al., 1998	P. Thevenaz, U. E. Ruttimann, and M. Unser, "A pyramid approach to subpixel registration based on intensity", IEEE Transactions on Image Processing, vol.7, pp. 27-41, 1998
Timmis et al., 1997	Adam D. Timmis, Anthony W. Nathan and Ian D. Sullivan, "Cardiology 3rd Ed.", Blackwell Science Ltd., 1997
Umbaugh, 2005	Umbaugh Scott, "Computer Imaging: Digital Image Analysis and Processing", CRC Press, 2005
Valk, 1987	J. Valk, "MRI of the brain, head, neck and spline", Nijhoff, 1987
Vulliemoz et al., 2002	Serge Vulliemoz, Nikos Stergiopulos and Reto Meuli, "Estimation of Local Aortic Elastic Properties with MRI", Magnetic Resonance in Medicine, Vol. 47, pp.649-654, 2002

Yezzi et al., 1997	Anthony Yezzi, Arun Kumar, Peter Olver and Allen Tannenbaum, "A Geometric Snake Model for Segmentation of Medical Imagery", IEEE transactions of medical imaging, VOL. 16, No. 2, April 1997
Wendland et al., 1999	Wendland MF, Saeed M, Lund G, Higgins CB, "Contrast-MRI for Quantification of Myocardial Viability"", JMRI, 10:694-70, 1999
Wilke et al., 1994	N. Wilke, M. Jerosch-Herold, A. E. Stillman, et al., "Concepts of myocardial perfusion in magnetic resonance imaging", Magnetic Resonance Quantisation, Vol. 10, pp. 249 – 286, 1994
Wolff et al., 2004	Wolff SD, Schwitter J, Coulden R et al., "Myocardial first-pass perfusion magnetic resonance imaging: a multicenter dose-ranging study", Circulation, 110(6):732-737, August, 2004